1-3-2022

Centrifugal assembly of bijel ropes via helical microfluidics

Shankar P. Kharal
Rowan University

CENTRIFUGAL ASSEMBLY OF BIJEL ROPES VIA HELICAL MICROFLUIDICS

by

Shankar P. Kharal

A Dissertation

Submitted to the
Department of Chemical Engineering
College of Engineering
In partial fulfillment of the requirement
For the degree of
Doctor of Philosophy
at
Rowan University
December 8, 2021

Dissertation Chair: Martin F. Haase, Ph.D.

Committee Members:
Gary Thompson, Ph.D.
Joseph Stanzione, Ph.D.
Robert P. Hesketh, Ph.D.
Vince Beachley, Ph.D.

Dedication

To Nature.

Acknowledgment

Foremost, I would like to express my sincere gratitude to my advisor Dr. Martin F. Haase for the continuous support of my PhD study and research, for his patience, motivation, enthusiasm, and immense knowledge. I could not have imagined having a better advisor and mentor of my PhD study.

Besides my advisor, I would like to thank the rest of my thesis committee: Dr. Robert P. Hesketh, Dr. Joseph Stanzione, Dr. Gary Thompson, and Dr. Vince Beachley, for their encouragement, insightful comments, and motivations.

I thank my fellow labmates in Rowan University and Utrecht University, for the stimulating discussions, and all the fun we have had in the last three years. Special thanks to Lab technician Mr. Rob McClernan.

I would like to thank my parents, Mr. Dinanath Kharal and Jhabikala Kharal, for their unwavering support throughout my life. I would like to thank all of my siblings for their encouragement and support in achieving my goal.

During my PhD study, the charming and beautiful couple Dr. Kul Kapri and Dr. Sangeeta Pudasaini-Kapri gave us with a warm, welcoming and homey environment that I will remember for the rest of my life, thank you.

Finally, and most importantly, huge thank you to my beautiful and lovely wife Anjana for her full-supports, caring, and love.

Abstract

Shankar P. Kharal
CENTRIFUGAL ASSEMBLY OF BIJEL ROPES VIA HELICAL MICROFLUIDICS
2020-2021
Martin F. Haase, PhD
Doctor of Philosophy in Chemical Engineering

Bicontinuous interfacially jammed emulsion gels (bijels) are soft materials that retain a liquid bicontinuous network stabilized by an interfacially jammed layer of nanoparticles. In this thesis, we investigated a microfluidic twisting method to fabricate micro-ropes of nano-structured bijel fibers. This method shows how weak microfibers with tensile strengths of a few kPa can be reinforced by 4 orders of magnitude by means of microfluidic twisting. Microfluidic twisting allows to produce continuous bijel fiber ropes of controllable architecture. Modelling the fluid flow field reveals the rope geometry dependence on a subtle force balance composed of rotational and translational shear stresses. However, the direction of the centrifugal force determines whether microropes undergo undulation during microfluidic twisting. The undulation of ropes can be avoided by decreasing the density of the fiber casting mixture, or upon increasing the density of the co-flowing liquid, enabling a controlled and continuous collection of uniform microropes. We envision microfluidic twisting to enable the fabrication of new composite materials with applications in flexible electronics, micro robotics, actuators, and tissue engineering. Furthermore, the knowledge gained from this thesis will facilitate future studies of microfiber twisting, as well as the assembly of particles, emulsion droplets or biological cells via microfluidic twisting.

Table of Contents

Table of Contents (Continued)

Table of Contents (Continued)

List of Figures

List of Figures (Continued)

List of Figures (Continued)

Chapter 1

Introduction

1.1 Research Motivation

The rapid growth of the world's population results in a significant increase in energy demand. Fossil fuels, the classical source of energy, are widely being used and they are major source to release large amount of harmful gases as their end-product. It is impossible to avoid this unwanted gaseous product but perpetuate release of these gases on the Earth's atmosphere leads to long term effects.[1][2] The finite resources in non-refillable nature and ecological deterioration prompted by processing these fuels urged to search new source of sustainable energy and materials. Energy efficient materials and technology both are urgently needed to optimize the use of limited natural resources in the Earth.[3][4]

Environmentally friendly industrial processes are being explored to meet the current demands. The understanding behind the transition from batch to continuous manufacturing is a critical step toward achieving a safer, greener, and more cost-effective industrial production. The major task to be addressed soon is to discover highly efficient continuous approach to produce value added materials to cut down production costs, reduce waste generation, avoid environmental contamination, and ultimately save natural resources for next generation.[5][6]

1.2 Relation of the Dissertation With Current State of Knowledge

Bicontinuous interfacially jammed emulsion gels (bijels) are soft materials.[7] The material preserves bicontinuous architecture of two immiscible fluids partitioned by a layer

of nanoparticles.[8] Bijels have a number of structural properties such as uniform, asymmetric, hierarchical and interconnected pore geometry, a tunable interfacial area, and the ability to introduce catalytically active materials with a specific thickness at the interface.[7][8][9] This property makes bijels a potential candidate for tissue engineering,[10] sensors,[11] catalysis,[12][13][14] electrochemical devices,[15][16] filtration membranes,[17] and food products.[18] Several fabrication schemes, computer simulation, and applications of bijels have already been investigated (Chapter 2).

Figure 1

Bijels
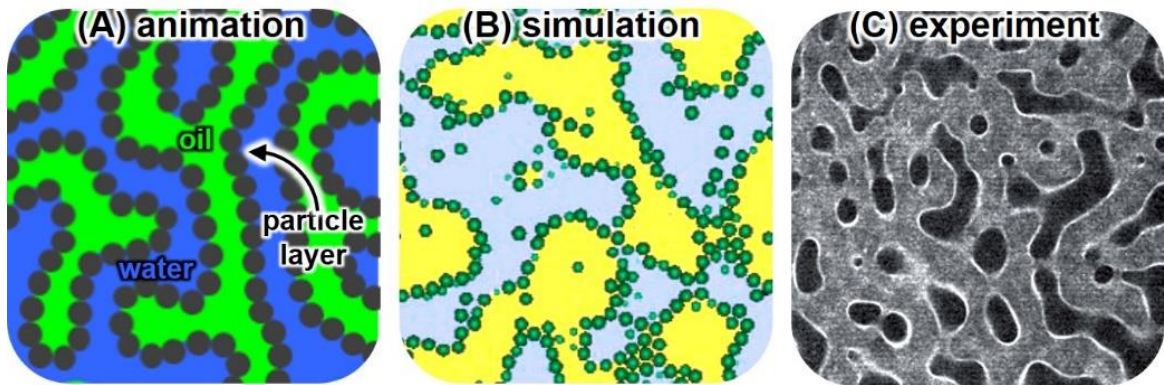
Note. (A) Animation depicting inherent features of bijels. (B) Micrograph of bijels obtained from computer simulation in the year 2005 (adapted from reference [7]). (C) Micrograph of bijels observed via experiments in the year 2007 (adapted from reference [8]).[7]

Bijels with a hierarchical internal architecture were discovered in 2015 by using a new microfluidic method called STrIPS (**S**olvent **Tr**ansfer **I**nduced **P**hase **S**eparation).[9] In this method, a bijel fiber is fabricated by injecting a homogeneous ternary liquid mixture of oil, water, and a suitable solvent into a continuous stream of water. When the ternary mixture is introduced into the stream of water, solvent diffuses establishing interpenetrating channels between the two other phases of water and oil. Concomitantly, surface-active nanoparticles dispersed in the ternary mixture bind to the liquid interfaces, stabilizing the bijel via interfacial jamming.

STrIPS enables the bijels in various shapes such as particles, fibers and membranes in a continuous fashion. However, the science governing the formation of bijels via STrIPS is yet not fully understood, necessitating more investigation. Current researches on STrIPS bijels are primarily focused in three directions: (i) determine the governing principle for colloidal stability in ternary mixtures, (ii) comprehend the underlying processes that occur during STrIPS, and (iii) tailor and measure mechanical properties, as well as investigate applications.[19] It is important to note that microfluidics is the technique used to process and manipulate STrIPS bijels in all mentioned research directions. Therefore, understanding the science behind microfluidics of STrIPS bijel is essential in order to process and manipulate bijels in the search for answers to numerous unexplained questions and application potentials.

1.3 Thesis Objectives

Microfluidics has been used to study the behavior of fluids and complex mixtures for several decades. Microfluidics is a discipline that examines the behavior of fluids in micro-channels, as well as a technology for making microminiaturized devices with

chambers and tunnels through which fluids can be confined.[20] Microfluidic devices have a high surface area to volume ratio, which leads to unique phenomena not seen at the macroscale.

The mechanics of geometrically constrained complex fluids in microchannel open up possibilities for fabricating high-value materials. The mechanics of coaxial flow in a microfluidic array of capillaries have been widely studied.[21][22][23] By combining the geometry of the device and the properties of the fluids, concurrent flow has been used to manipulate and control fluids.[24][25] Microcapillary devices have become a standard tool in many physical and biological sciences. Controlling fundamental forces in fluids with rotating micro-channels, on the other hand, has not been thoroughly researched.

Actively rotating the microfluidic channel opens up new possibilities for microfluidic twisting, helical assembly, and particle mixing or separation. The major purpose of this thesis is to present new microfluidic methods that allows fluids to flow continuously in a helical path. The rotational flow generated by actively rotating micro capillary channels is employed to examine microfluidic twisting and helical assembly of bijel fibers. Furthermore, helical flow field is utilized to build robust composite bijels and stimuli-responsive hydrogel ropes. The following are details of the many accomplishments in this research work:

1.3.1. Microfluidic Twisting Production of Bijel Fibers (Chapter 3)

The structural stability of bijels is because of the interfacially jammed nanoparticle scaffold, which forms the framework of the 3D bicontinuous architecture. The process of structure stabilization begins through fluid phase, transits viscoelastic stage, and finally

4

gets maturity becoming solid. The main goal of this chapter is to introduce continuous extrusion of bijel fibers in a helical fluid flow field.

The following four questions are the main focus of this chapter: (a) "How are multiple bijel fibers twisted to form a rope?" (b) "What are the governing physics that transform multiple parallel fibers into a rope?" (c) "How does geometrical features of the rope, such as helix angle, pitch length and diameter, be controlled?" (d) "How can the geometrical properties of ropes containing an arbitrary number of fiber strands change?"

Figure 2

Microfluidic Twisting
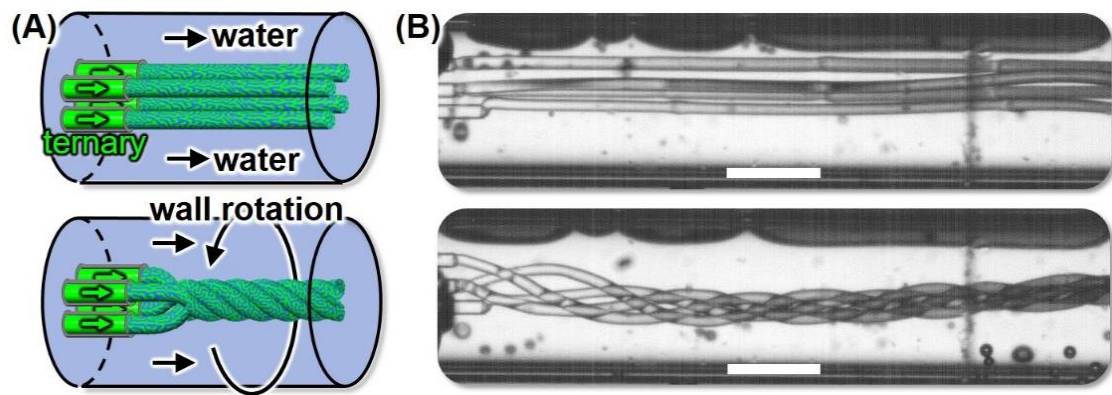
Note. (A) Schematics of four bijel fibers (top) and helix formation as channel wall rotation is activated (bottom). (B) Micrographs showing the formation of four bijel fibers (top) and a helix when the channel wall rotation is activated (bottom). Scale bar 0.5 mm.

1.3.2. Microfluidic Assembly of Helical Bijel Fibers via Centrifugal Forces (Chapter 4)

Centrifugal buoyancy force is crucial in manipulating and transporting fluids in a rotational microfluidic system. For example, centrifuge instruments are a well-known system that uses centrifugal force as its operating principle. The centrifugal force created due to the rotors in a centrifuge induces a hydrostatic pressure gradient in the tubes directed perpendicular to the axis of rotation. This results in larger buoyant forces that push the less dense particles inwards while the denser particles are moved outwards.[26] This enables component fluids to be separated based on their densities.

During microfluidic twisting of bijel fibers, the similar centrifugal effect appears. The control of centrifugal force effect during bijel rope extrusion is the main topic of this chapter. The following four questions will be addressed in this chapter: (a) "How does the bijel fiber density change during STrIPS over time?" (b) "During microfluidic twisting, how does the direction of centrifugal force changes with density evolution?" (c) "What effect does altering nanoparticle concentration in the fiber casting mixture have on the centrifugal force on the microropes?" (d) How does changing the density of the surrounding media around the microropes during extrusion control the centrifugal force effect?"

Figure 3

Microfluidic Assembly
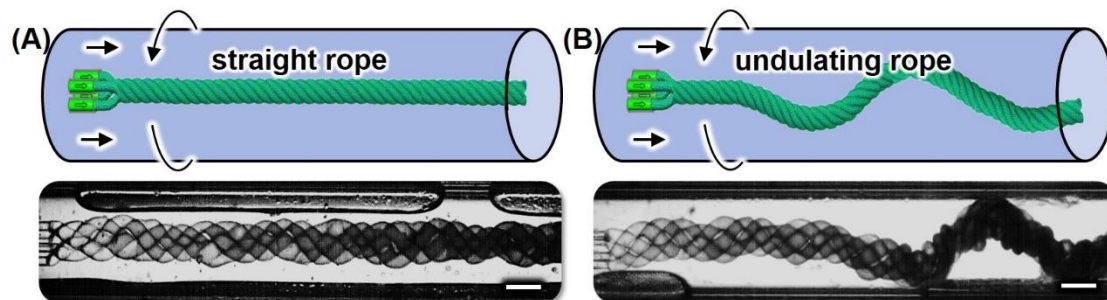
Note. Schematics and micrographs depicting a straight microrope in (A) and an undulating microrope in (B).

1.3.3. High-Tensile Strength, Composite Bijels and Derived Materials (Chapter 5)

Twisting multiple fibers into higher order helices or ropes combines the qualities of the individual fibers, resulting in a diverse reinforcement technique with numerous application possibilities. The mechanical strength of bijel ropes and the bijel derived hydrogel ropes are the major focus of this chapter.

In this chapter, we primarily address the following four questions: (a) "How do we transfer the bijel ropes from rotating to non-rotating environment during collection?" (b) What modifications do we need to make to the microfluidic system in order to extrude composite bijel ropes?" (c) "How does selective polymerization during microfluidic twisting contribute in tensile strength enhancement?" (d) What are the properties of composite hydrogels generated from the bijel route in different pH environments?"

Figure 4

Composite Bijels

(A) composite bijels | **(B) bijel-derived stimuli responsive hydrogels**
pH 4 | pH 10
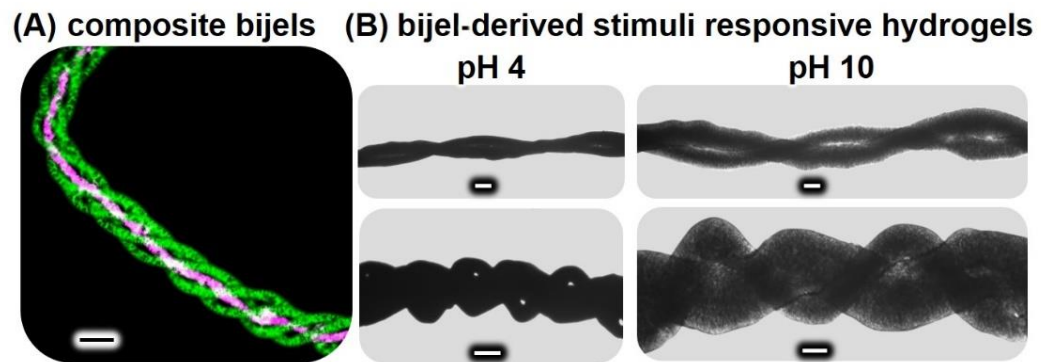
Note. (A) Micrograph representing composite bijel rope made of 5-fiber strand. (B) Micrographs representing hydrogel ropes at different pH of the surrounding fluid.

Chapter 2

Literature Overview

2.1 Bijels

The basic mechanism of bijel stabilization is the reduction of the interfacial free energy by the interfacial self-assembly of colloids. The attachment energy of a spherical particle on the interface of two immiscible fluids (oil-water) is $\Delta G = -\pi\gamma_{ow}a^2(1 \pm cos\theta)^2$ with a the particle radius, γ_{ow} the oil/water interfacial tension and θ the contact angle measured through either of the phase.[27] For given immiscible media and particles the attachment energy is controlled by tuning wettability (angle of contact). The attachment energy reaches maximum, $\Delta G = -\pi\gamma_{ow}a^2$ at $\theta = 90^o$, which equals the reduction of the oil-water surface energy by the removal of the surface occupied by the particle. The attachment energy can reach several thousands of K_BT, where K_B is the Boltzmann's constant and T is the absolute temperature, rendering the attachment virtually irreversible.

The particle packing constraints at the interfacial curvature influences the architecture of the oil/water scaffold. Particles with $\theta < 90^o$ curve the oil-water interface towards the oil to form oil-in-water droplets, while particles with $\theta > 90^o$ curve the interface towards the water to form water-in-oil droplets. In the case of bicontinuous stabilization, both positive and negative Gaussian curvatures are present, and this requires particles with $\theta \approx 90^o$. [28][29] Excellent emulsion stability results when particles form a densely packed, interfacial monolayer, sterically hindering droplets from coalescence or bicontinuous emulsions from further coarsening.

Figure 5

Bijel Formation Principle
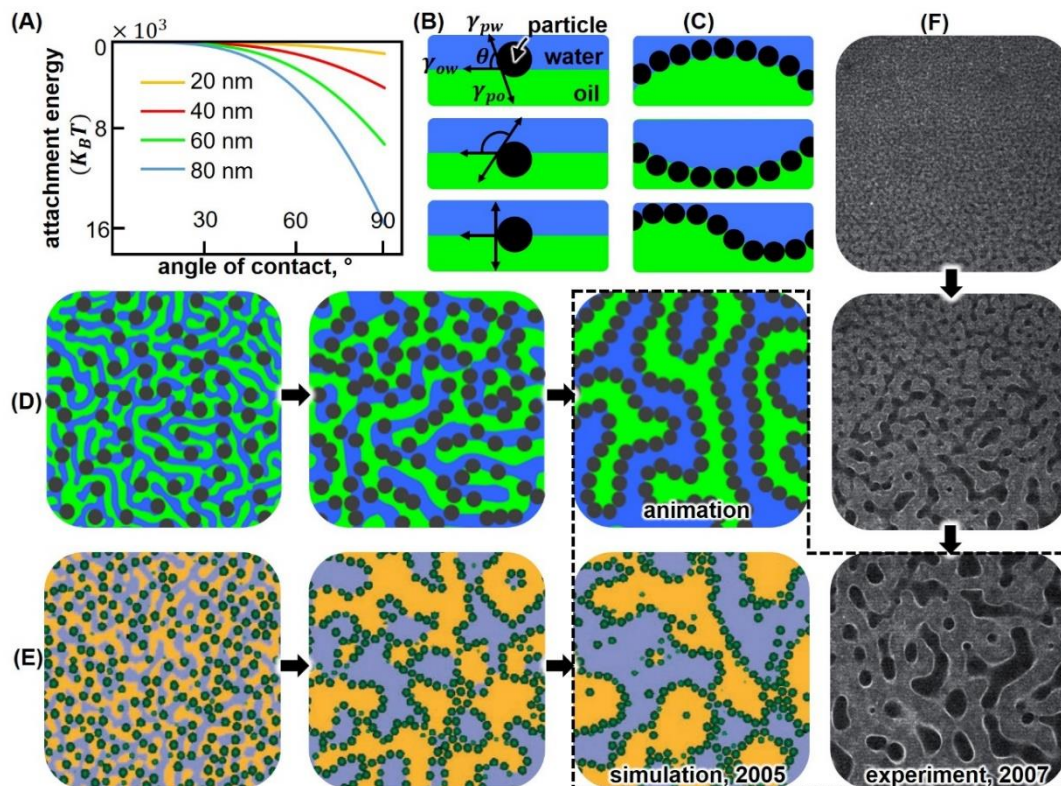
Note. (A) A graph depicting attachment energy as a function of contact angle at the oil-water interface for nanoparticles ranging in size from 20 nm to 80 nm. (B) At the oil-water interface, particles of varied wettability and the related interfacial curvatures are illustrated in (C). (D) An animation depicting spinodally decomposed oil (green) and water (blue) phases with dispersed colloidal particles, as well as the creation of bicontinuous surfaces over time. (E) Bijel evolution predicted through computer simulation in 2005 (adapted from reference [7]). (F) Bijel evolution over time observed experimentally in 2007 (adapted from reference [8].

2.2. Bijels: Fabrication to Application

The origins of bijels can be traced back to simulations conducted at the University of Edinburgh in the year of 2005 to see if colloidal particles might be utilized to stabilize a liquid interface of two immiscible fluids.[7] Following the use of computer simulations to predict bijel stability in 2005, laboratory investigations were conducted in 2007 to confirm bijels by experiment.[8] Since the experimental realization of bijels in 2007, numerous researchers have been working to improve the fabrication procedures.[8][30][31][9][32][33] Following that, we will review over the bijel fabrication methods in the next.

2.2.1 Bijels by Thermal Quenching Method

Bijel was initially demonstrated experimentally by dispersing colloidal particles in a binary water-lutidine mixture and afterwards thermally quenching the mixture. The particles were selected in such a way that they preferentially partition to the liquid-liquid interface ($\theta \approx 90^0$), where they jam and prevent the phase separation process. The liquids were miscible above the upper critical solution temperature (UCST) in the binary liquid composition. It was necessary to quench the system deeply and quickly in order for spinodal decomposition to occur. The fluids must go through spinodal phase separation to achieve bijel morphology; otherwise, nucleated structures will develop instead of bicontinuous structures. Most bijel fabrication protocols follow this basic path, with the only difference being whether selected binary mixtures are heated to a lower critical solution temperature (LCST)[8][30] or cooled to an upper critical solution temperature (UCST)[34][35] to generate bicontinuous structured materials, as shown in Figure 6.

11

The same research group who invented bijels first time was successful in synthesizing three-dimensional bijel material later that year. This was accomplished by using a single layer of colloidal particles to stabilize bicontinuous surfaces. [8] It was also critical to maintain particle wettability in order to stabilize the bicontinuous interface. The particles must be wetted neutrally, with a contact angle of 90 degrees. Otherwise, depending on their wettability, the particles partitioned into one of two liquid phases. Hydrophilic particles with a contact angle of less than 90 degrees go into the water phase, while hydrophobic particles with a contact angle of more than 90 degrees move into the oil phase. Furthermore, following a fast-thermal quench from room temperature to 40 degrees Celsius, the critical composition of lutidine (0.644 mole fraction, Lutidine) plays an important role in bypassing the nucleation areas. The liquid components containing a lower critical solution temperature (LCST) phase separated, and the particles collected at the fluid interface, jamming the phase separation process. As a result, maintaining a stable bijel material necessitates a high temperature condition as well as careful tuning of particle wettability to fit various liquid-liquid compositions.

Bijel capsules, an alternative to numerous emulsions, were developed in 2011 within a Pickering drop.[36] The binary mixture of nitromethane and ethanediol was cooled to room temperature to promote spinodal decomposition in the drops, which was arrested by the silanized silica. For the first time, bijel with domain sizes less than ten micrometers was fabricated using a higher concentration of 100 nm silica particles. As a result, produced capsules are stimuli responsive, indicating that they could be used in controlled release applications such as triggering flavor blending in various food formulations.[36]

Figure 6

Thermal Quenching Method
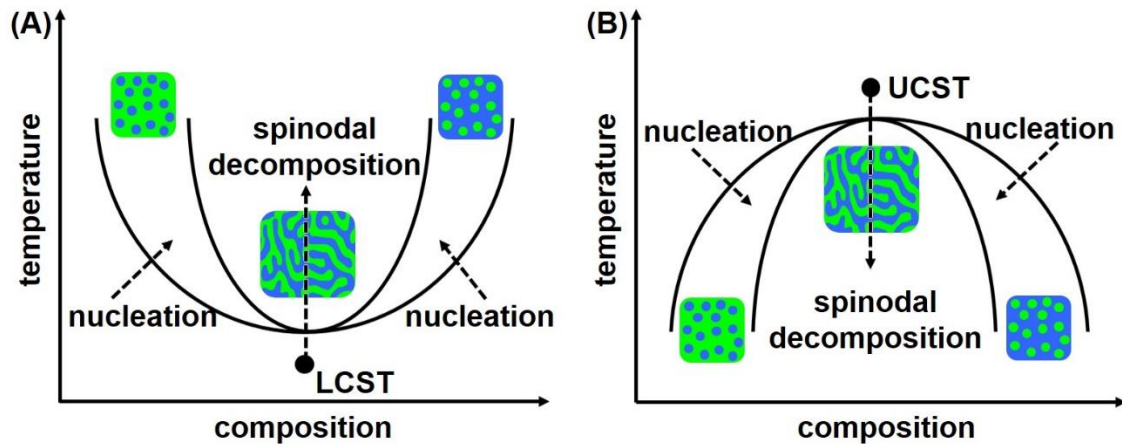
Note. (A) When binary mixtures are heated through a lower critical temperature (LCST). (B) When binary mixtures are cooled into an upper critical solution temperature (UCST).

Porous materials with changeable morphology and chemistry have a wide range of uses in energy and healthcare. Inspired by the many possibilities given by bijels for generating bicontinuous porous scaffolds, Lee et al. build macro porous bijel materials.[30] Their goal was to use the bijel scaffold in tissue engineering, catalysis, sensors, and fuel cells in their research. Microporous ceramic monolith with solid/pore morphology, metal coated microporous polymer scaffold, hierarchical porous and bicontinuous metal monoliths, and composite hydrogels for biomedical implants are some of the composite materials they have developed.[31][37][10]

13

The material features of these co-continuous and fully interpenetrating bicontinuous pathways were greatly improved, including effective electrochemical transport in porous electrode materials [15] and a scaffold for cell development.[10] This group's work includes turning a liquid bijel domain into a polymer bijel scaffold by including a photo initiator into a cross-linkable monomer. The resulting polymer bijel scaffold is then utilized to make hierarchical porous gold [38] and silver monoliths [31] for applications in catalysis, tissue engineering, sensing, and energy.

Figure 7

Polymerized Bijels
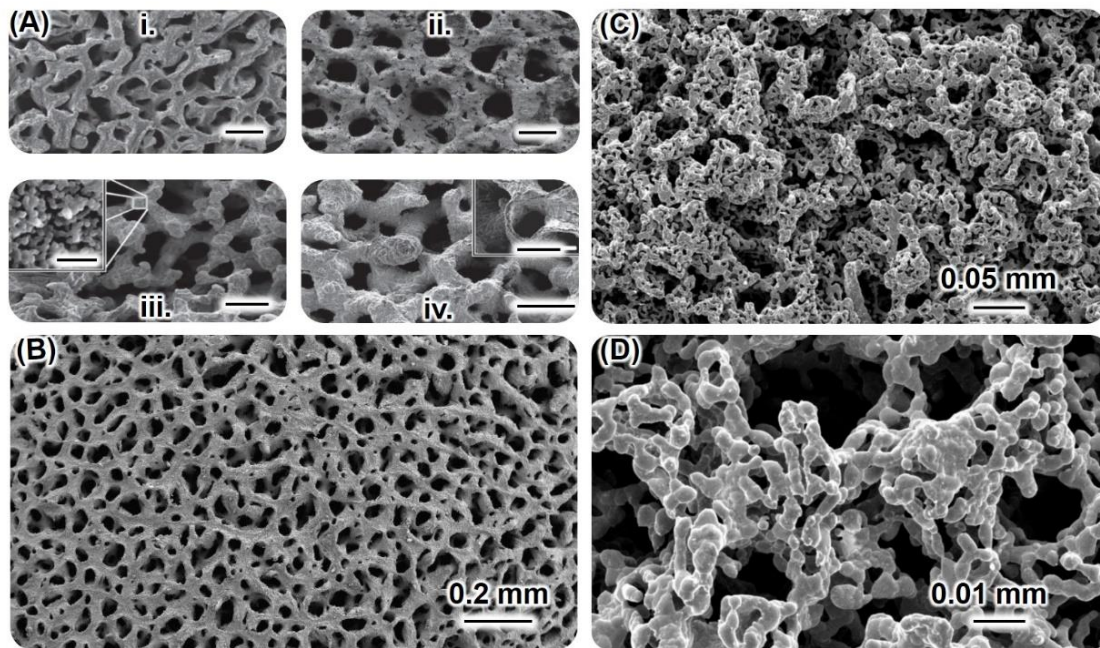
Note. (A) Polymerized bijel template (adapted from [30]) (i) Microporous ceramic (ii) Copper coated microporous polymer (iii) Hierarchical pore network (iv) Spinodal nickel

shell. Scale bar 50 µm. Inset scale bars correspond to 500 nm (iii) and 20 µm (iv). (B)

SEM image of selectively polymerized PEGDA bijel. SEM images of silver monoliths

are shown in the Figure (C) and (D) (adapted from [31])

In recent years, bijel research has expanded in a variety of ways. One such example

is edible bijel, which is a food product created within a bijel architecture. It was the first

time in 2014 that a bicontinuous architecture was used to demonstrate the potential to

stabilize particular food components. Inactivated singled-cell microorganisms were added

to gelatin-maltodextrin gels undergoing spinodal phase separation to achieve this.[18]

Other food-based systems incorporating emulsification for diverse flavors, texture, and

calorie reduction employing a wide range of food-based particles are presently being

researched in this field.

Figure 8

Bijel Applications
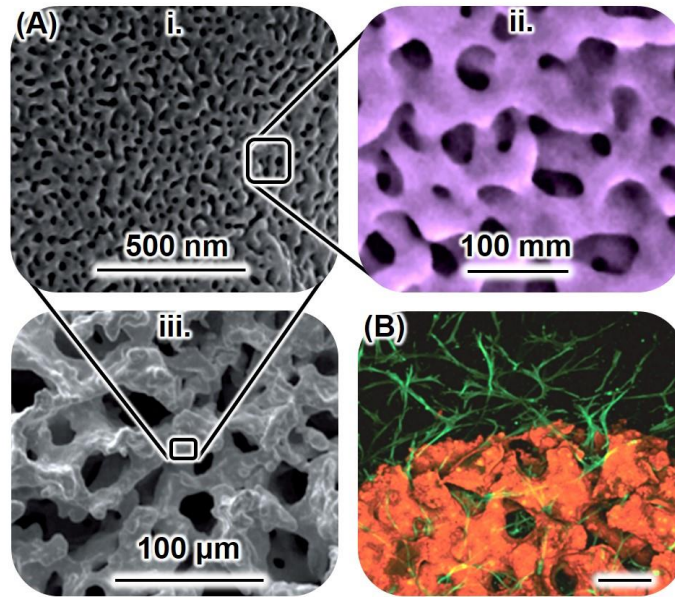
Note. (A) SEM images of monolithic porous gold with hierarchical porous bijels (adapted from [38]). (B) Confocal image representing cell delivery by using bijel template scaffold, scale bar 200 µm (adapted from [10])

The thermal quenching process, however, is time-consuming due to the requirement for fine-tuning particle wettability to fit various liquid-liquid mixtures, as well as high heat conditions to keep the bijel material stable. Additionally, this process uses batch protocol to create bijels, which is an important step yet to be realized for mass production. Furthermore, bijels of various geometrical shapes such as fibers, membranes, ropes, and other similar geometrical shapes cannot be generated.

16

2.2.2 Bijels by Solvent Transfer Induced Phase Separation (STrIPS) Method

In 2015, Haase et al. discovered STrIPS (Solvent Transfer Induced Phase Separation) as a novel method for making bijels.[9] This method, in particular, addresses the major issue with the thermal quenching method that are connected to continuous production of bijels.

Instead of the binary mixture solution used in the thermal quenching approach, STrIPS uses a ternary mixture of two immiscible fluids plus a suitable solvent to achieve spinodal decomposition of the fluids. Here, spinodal decomposition is achieved by employing microfluidic diffusion method.

For a bijel fabrication by STrIPS, a ternary solution of oil (for example Diethyl phthalate (DEP)), water and alcohol (ethanol) is prepared by choosing the critical composition as shown in the Figure 9A. The ternary solution also contains silica nanoparticles and suitable surfactant ($C_{16}TAB$). When the ternary mixture is injected into the stream of water, it phase separates because of the solvent diffusion. There can be two types of phase separations: (i) If the ternary composition is far away from the critical composition it results either W/O emulsion, or O/W emulsion. (ii) If the ternary composition is near the critical composition it results with spinodal decomposition during diffusion (Figure 9B). When the interfaces of two immiscible fluids appear during spinodal decomposition, the surface-active nanoparticles (Figure 9D) attach at the interfaces stabilizing the structures. The attachment improves with the jamming of nanoparticles in the course of time and eventually becomes bicontinuous interfacially jammed emulsion gels (Figure 9E).

Figure 9

STrIPS
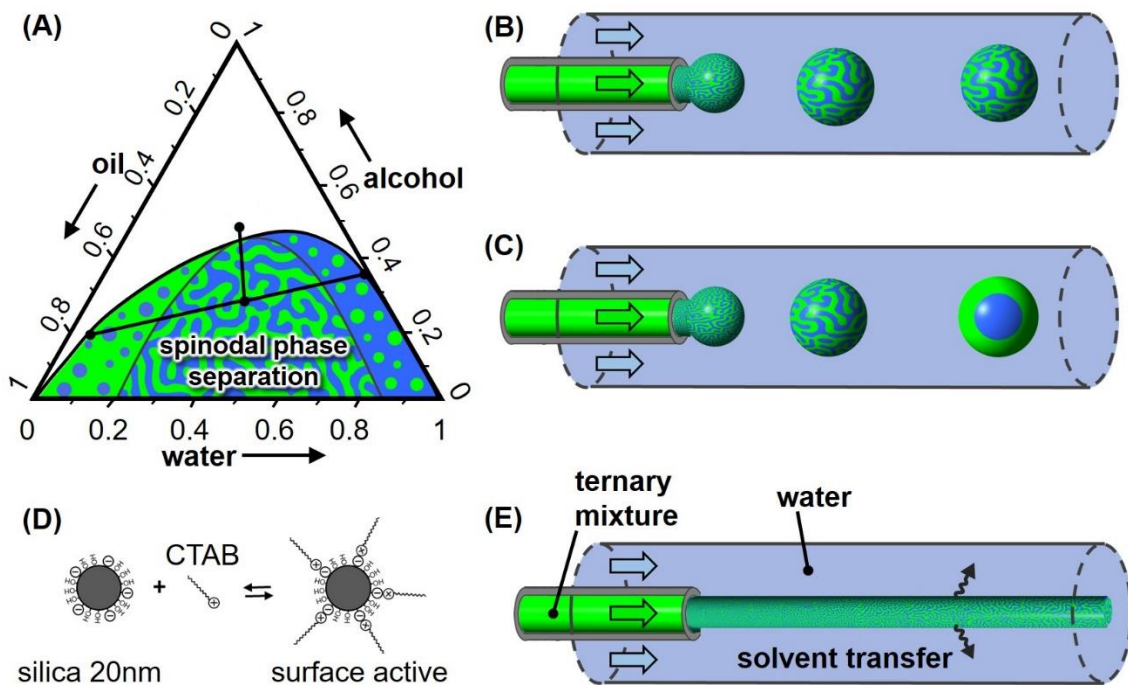
Note. (A) Ternary phase diagram representing binodal line, critical point, and spinodal phase separation region. (B-C) Schematics depicting droplets with spinodal phase separation and nucleation. (D) Surface modification chemistry of silica nanoparticles in the presence of surfactant ($C_{16}TAB$) (E) Bijel fiber generation due to the attachment of nanoparticles at the interfaces of two immiscible fluids during spinodal decomposition.

The advantage of employing STrIPS to make bijels is that it is a continuous and scalable process that allows for large-scale production. In addition, STrIPS bijels can be made with a number of liquid combinations to derive beneficial uses. STrIPS has been

utilized to manufacture a wide range of materials, including microparticles (Figure 10A (left)),[9] fibers (Figure 10A (right)),[39] planer membranes (Figure 10B (left)),[9] hollow fiber membranes (Figure 10B right),[17] resulting in novel applications in ultrafiltration and biphasic catalysis. The underlying mechanism that occurs during the STrIPS process and the controlling principle of colloidal stability in ternary mixture solutions are two major areas that need to be further investigated.

Bijels generated by thermal quenching or STrIPS, on the other hand, are both fragile in their inherent state. Bijels, regardless of their creation method, are prone to losing their structure and usefulness when subjected to external stressors. Mechanical agitation can very easily alter the macro- and micro-structure of bijels. The chemical and mechanical fragility of bijels makes them unsuitable for potential applications. In order for their prospective uses to be realized, their strengths must be improved.

In 2018, Giuseppe et al. discovered a method for tailoring the stability of STrIPS bijels. In his approach, tetraethyl orthosilicate (TEOS) is added to a ternary mixture, which undergoes hydrolysis and condensation reactions to bind the nanoparticles together, establishing a nanoparticle scaffold throughout the bijels.[13] Later, they used TEOS treated bijels for reactive separations. In 2019, Ansah et. al used functional particles to stabilize STrIPS bijels, and then demonstrated the use of partially functionalized particles and controlled surfactant adsorption to make STrIPS bijels using highly charged particles.[40][41]

Figure 10

Various Geometrical Shapes of Bijels
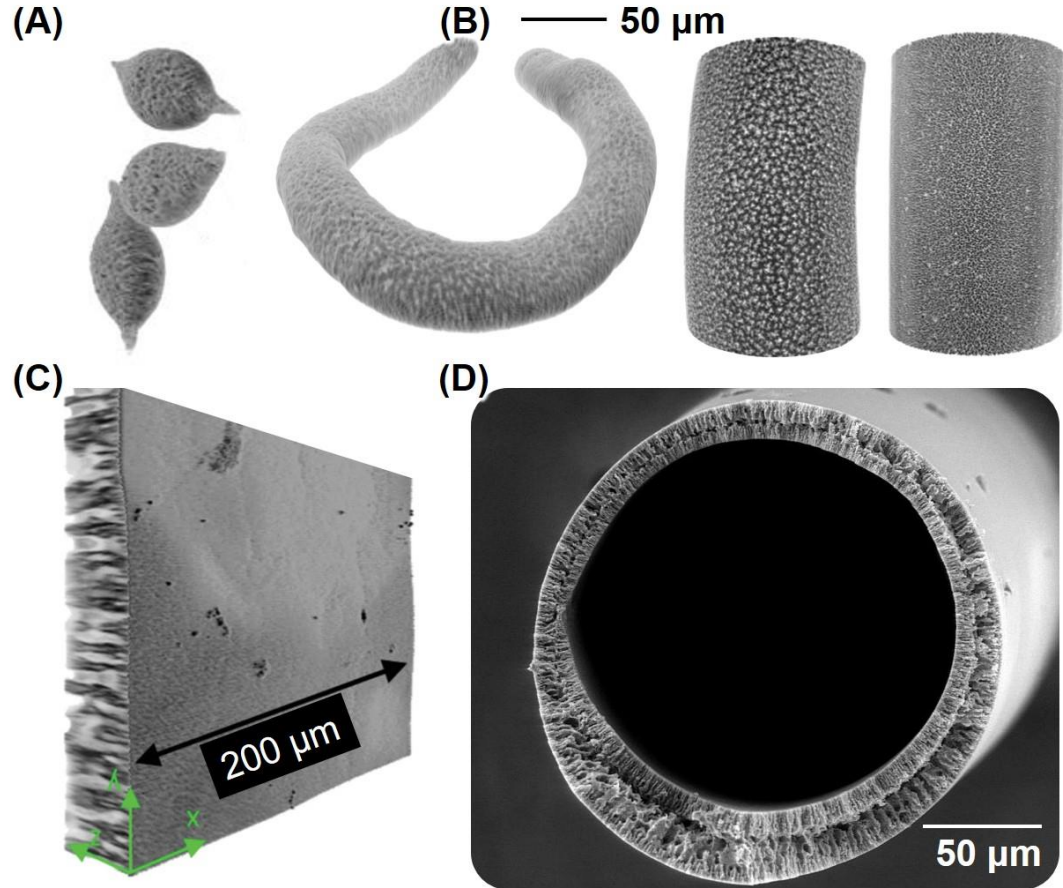
Note. (A) Particles (blobs) (adapted from [9]) (B) Fibers in different size (adapted from [39]) (C) Planer membranes (adapted from [9]) (D) Hollow fiber membranes (adapted from [17]).

2.3. STrIPS Bijels and Microfluidics

The backbone for processing and manipulating STrIPS bijels is microfluidics. Bijels in various geometrical shapes such as fibers and hollow fiber membranes are

typically made by incorporating the fluid properties and the microfluidic device geometry. The fundamental science behind multiphase flow of immiscible fluids is reviewed next, followed by a discussion of how we integrate the fluid properties with the microfluidic techniques to generate bijels of various shapes.

2.3.1 Concurrent Flow of Immiscible Fluids

Complex flow behaviour can be generated by the simultaneous flow of distinct fluids such as immiscible fluids, Newtonian and non-Newtonian fluids, and Newtonian fluids with substantial viscosity differences. When a Newtonian fluid is forced to flow through a capillary channel while another Newtonian but immiscible fluid is continuously flowing through it, it will eventually break down into drops near the orifice or distant from the orifice, resulting in dripping and jetting. Many factors influence the dripping or jetting mechanism, including fluid average velocities, viscosity, density, interfacial tension, surface chemistry, and device shape. The behaviour of fluids is controlled by the dominance of either shear force or inertial force, as specified by the equations below.[23]

$$C_a = \text{Shear force / surface tension force} = \frac{\mu u}{\gamma} \qquad \qquad \textit{Equation 1}$$

Where μ represents viscosity of fluids, u is the fluid velocity and γ denotes the surface tension.

When $C_a > 1$, shear force deforms droplet away from sphere.

The weber number (W_e) is also a dimensionless number which is defined as the ratio of inertial force and surface tension.

(W_e) = inertial force of outer fluid / surface tension force = $\dfrac{\rho u^2 d}{\gamma}$ *Equation 2*

Where ρ denotes density, u represents the average velocity, d is the droplet diameter and γ denotes the surface tension. Inertial forces are the force due to the momentum of the fluid. The denser a fluid is, and the higher its velocity, the more inertia it has. Viscous forces are the frictional shear forces due to the relative motion of the different layers in a flowing fluid. The ratio between the inertial forces and the viscous forces is defined by another dimensionless number called Reynolds number (*Re*):

Re = Inertial force / viscous force = $\dfrac{\rho u L}{\mu}$ *Equation 3*

Where ρ stands for the density of the fluid, u signifies the fluid velocity, L represents a characteristic linear dimension, and μ refers to the fluid viscosity. The Reynold number define the flow regime of the fluid. At low Reynold number values, the viscous forces are greater than the inertial forces and the flow regime within the capillary is laminar. When the viscous forces are dominated by the inertial forces, the turbulent flow occurs. The flow of fluid within our designed microfluidic capillary channel is the laminar flow. The condition for the jetting is the high flow rate of outer and the middle fluid. When $C_a > 1$ and $W_e > 1$ the jetting phenomenon occurs, which is illustrated in the Figure 8B. The condition for the dripping phenomena is the low flow rate of outer and the inner fluid. In this case when $C_a < 1$ and $W_e < 1$ the dripping phenomenon occurs.

Figure 11

Dripping and Jetting Phenomena
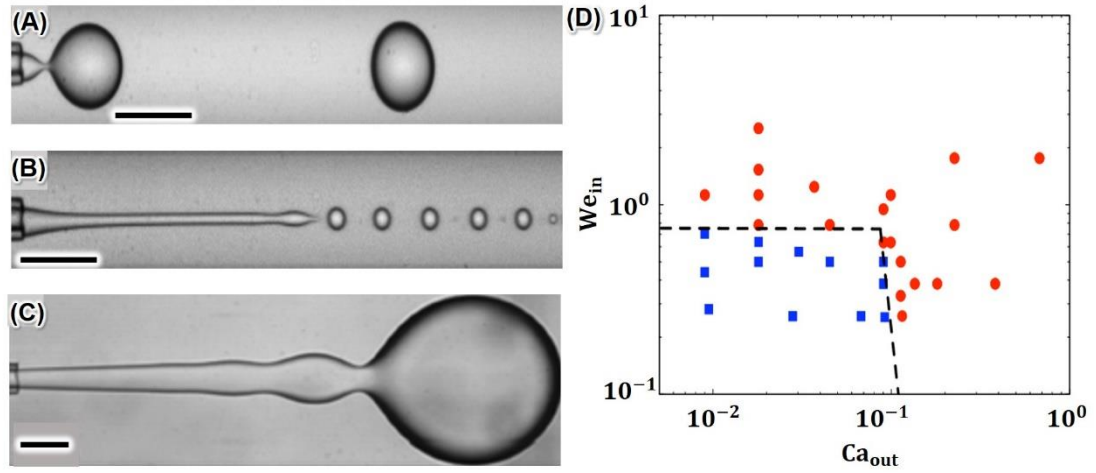
Note. (A) Dripping (B) Narrowing jetting (C) Widening jetting (D) State diagram representing dripping and jetting region. Squares represent dripping while circles represent jetting.(adapted from [23]) Scale bars are 50 µm.

2.3.2 Single Bijel Fiber Extrusion

In a microchannel environment, the laminar flow required for fluid control is easily obtained. By maintaining laminar flow and precisely controlling fluidic inertia, surface tension and viscosity fibers with various cross-section and structures can be generated. Furthermore, proper solidification processes play a key role in fiber production and structural variety. Photo polymerization, chemical cross-linking, ionic cross-linking, solvent exchange, non-solvent driven phase separation, and solvent evaporation are some

of the most often employed methods of solidifications. Furthermore, fiber materials can be

modified for particular application by encapsulating functional materials.

Figure 12

Generation of Controlled Fibers
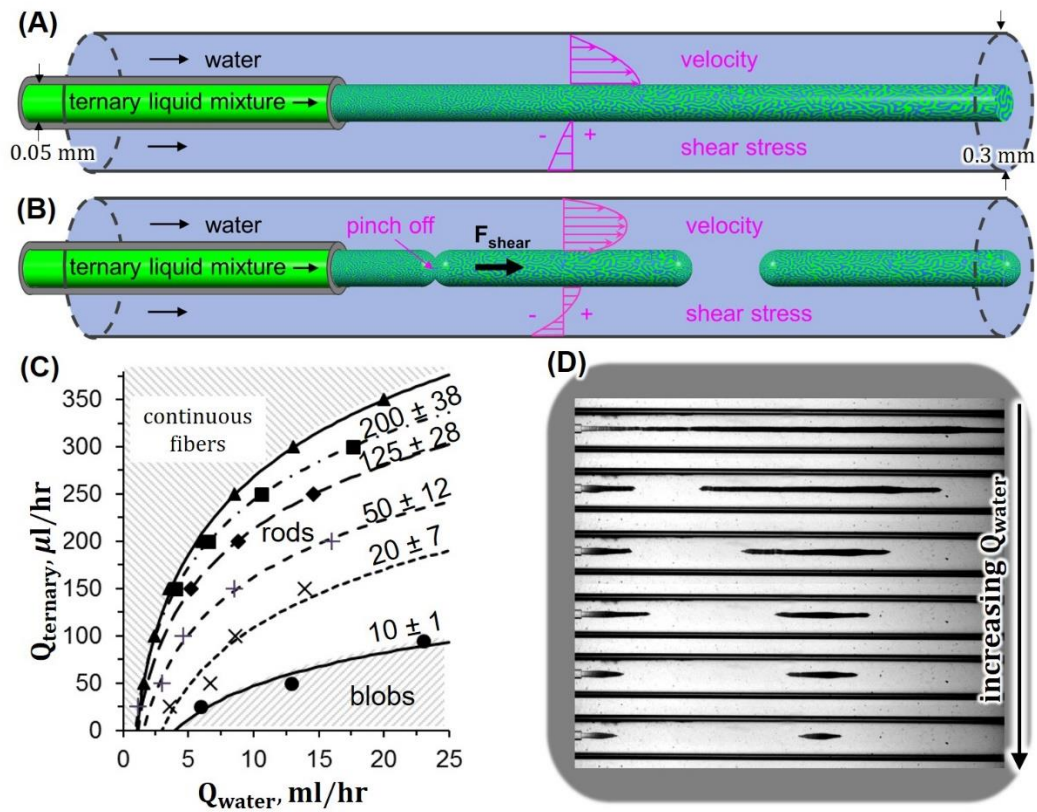
Note. (A) Continuous fiber generation (B) Segmented fiber generation (C) Graphical

representation to distinguish the blobs, rods, and fiber generation region for given device

and ternary mixture. (D) Micrograph representing different dimension of bijel rods at

different flow rate of the water phase. (adapted from [39])

The precise control of fiber structure is the most significant advantage of microfluidics over other approaches. Utilizing the simplest single channel or two phase coaxial microfluidic channels, microfibers with a cylindrical shape are most easily manufactured using microfluidics. The precise controllability of fiber dimensions is a crucial issue, which is influenced by channel dimensions, flow rates, and the method of solidification.

STrIPS bijels in terms of particles, rods and fibers is generated by employing a simple microfluidic device by assembling coaxially aligned glass capillary (Figure 12A-B). For given geometry of the device and ternary mixture solution, bijel particles (blobs), bijel rods, and bijel fibers are fabricated by tuning suitable flow rates of the ternary mixture and the water phase (Figure 12C). With the variation of the water, flow rates at constant ternary mixture flow rate, the velocity of the fiber changes and experiences dissimilar shear stresses to get definite shape during extrusion (Figure 12D).

2.3.3 Fluid Flow Around the Fiber Surface

In general, Navier-Stokes-Equations (NSE) are used to study and analyze the flow profile of fluids. NSE for a fluid of density ρ moving with velocity V in a non-rotating frame of reference can be written as:

$\nabla . V = 0$ (continuity equation),   *Equation 4*

$\rho \left(\frac{DV}{Dt} \right) = -\nabla P + \rho g + \mu \nabla^2 V$ (Momentum Equations).   *Equation 5*

In the momentum equation, $\rho \left(\frac{DV}{Dt} \right) = \rho \left[\left(\frac{\partial V}{\partial t} \right) + (V.\nabla)V \right]$ represents the total derivative $\left(\left(\frac{\partial V}{\partial t} \right) \right.$ denotes the change in velocity over time and $(V.\nabla)V$ refers to the

convective effect). Similarly, ∇P refers to the pressure gradient because fluids flow in the direction of reducing pressure, ρg represents the body forces that act on the fluid such as gravitational force or electromagnetic force. The term $\mu \nabla^2 V$ describes the diffusion during the flow, for example, viscosity (μ) operates as a diffusion of momentum in a Newtonian fluid flow.

Figure 13

Velocity and Shear Stress Profiles Around a Bijel Fiber
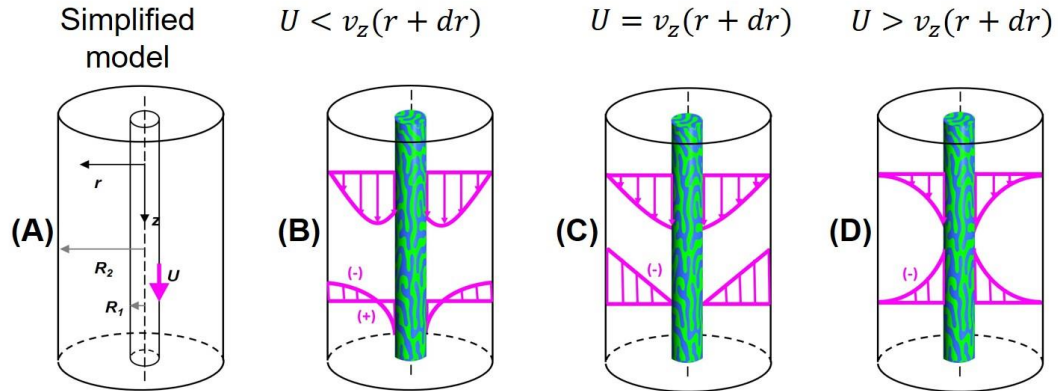
Boundary conditions: $(i)\ r = R_1 \quad v_z = U \qquad (ii)\ r = R_2 \quad v_z = 0$

Axial velocity: $v_z(r) = -\dfrac{dp}{dz}\dfrac{(R_2^2 - r^2)}{4\mu} + \left\{ U + \dfrac{\frac{dp}{dz}(R_2^2 - R_1^2)}{4\mu} \right\} \ln\left(\dfrac{R_2}{r}\right) / \ln\left(\dfrac{R_2}{R_1}\right)$

Shear stress: $\tau_{rz}(r) = \mu \dfrac{\partial v_z}{\partial r}$; Force: $F_z(r) = \tau_{rz}(r). 2\pi r. L_s$

Note. (A) Model development (B) Fiber moving slower than the water phase (C) Fiber moving with the same speed as water. (D) Fiber moving faster than water.

NSE can be used to determine the flow profile around the bijel fiber surface. For example, a cylindrical fiber of radius R_1 moving at a fixed velocity U can be compared to a cylindrical annulus with an inner cylinder (fiber) flowing at velocity U in a bigger channel of radius (R_2) without slipping and a static outer wall moving at zero velocity. Various characteristic parameters such as fiber length(L), fiber radius(R_1), fiber velocity(U), and pressure drop along the flow direction dp/dz must be quantified in order to simulate the flow field by determining shear stress profiles around the fiber surface. The velocity of the fiber can be evaluated using high-speed imaging; however, other required characteristic parameters can be approximated from experimental data. The fiber can move slowly, at the same speed as, or faster than the speed of the outside water. Figure 13 depicts the velocity $(v_z(r))$ and shear stress profiles $(\tau_{rz}(r))$ in such instances. A similar model was used previously to measure the tensile strength of bijels by creating a conical constriction in the flow channel.[39] When the device geometry is complex and several fluids are injected at different speeds through the channel, fluid modeling becomes more challenging.

2.4 Twisted Fibers and Their Importance

Helical structures are found in nature at both the micro- and macro-scales. Fabricating helical structures with controlled morphology and helicity is crucial in biology, physics, and materials science. [42]

The significance of helical structures is based primarily on space-saving configurations, mechanical strength and bending flexibility, and the development of composite materials. For example, to save space, staircases are built in a helical shape. Similarly, plant tendrils climb trees by following the helical path because it is the shortest path in 3D space.[44] DNA double helix is used to store genetic information in high density

at the molecular level. To increase tensile strength, textile fibers are twisted or braided together to form a rope. There are several methods for fabricating helices depending on their length scale.

Figure 14

Micrographs Representing Helical Stricture in Different Length Scale
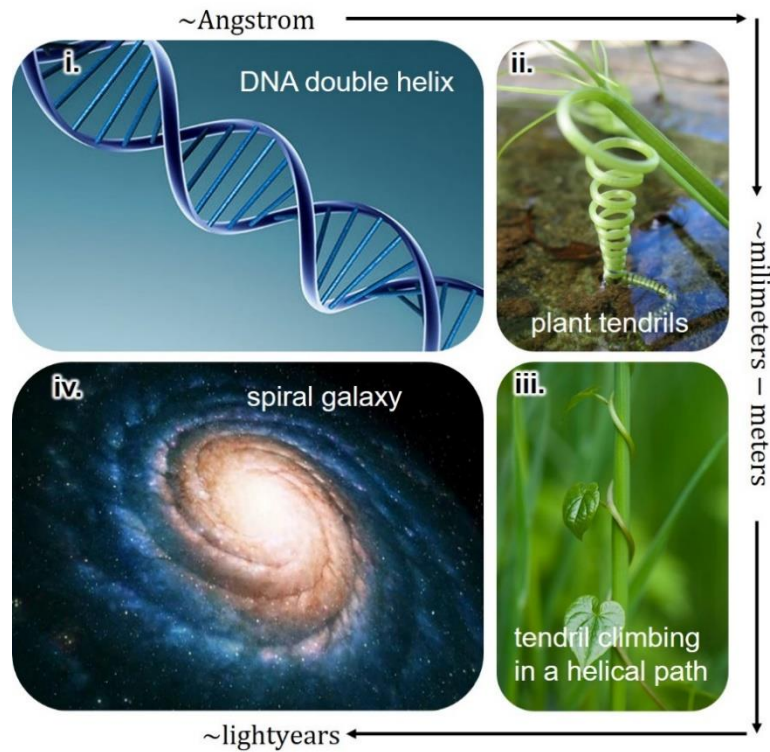
Note. (i) DNA double helix (ii-iii) Plant tendrils (iv) Spiral galaxy.

Helical structures are formed on a small scale using a variety of techniques such as vapor deposition,[45] entropy driven force,[46][47] DNA origami,[48] and molecular

chirality.[49][50][51] On a larger scale, however, the helical structures are formed by twisting the extrusion nozzles or collection substrates, which adheres to the batch protocol. Nanofibers generated by electrospinning have recently gained popularity due to their fabrication method and potential applications.[52][53] Twisting fibers and other materials into helical shapes remains easier if the mechanical strength of the fiber is sufficient to maintain the processing threshold during twisting. The twisting of numerous microfibers after their production with the aid of a motor-driven rotating system or a micro weaving machine is a straightforward way for constructing helical microfibers. To make twisted or helical micro fluids, a fundamentally different concept of a microfluidic technology is required, and the investigation of such methods is still ongoing. Twisting soft materials with low mechanical strength, such as bijel fibers,[9] reconfigurable printed liquids,[54][41] hydrogels,[55] capillary suspension,[56] high-internal phase emulsions, or colloidal gels,[57] necessitates a novel approach.

2.5 Rotational Flow and Centrifugal Microfluidics

In everyday life, rotating flow of fluids has been observed in a variety of ways. Centrifuges, for example, are commonly used pieces of laboratory and industrial equipment.[26] As a centrifuge-rotor spins, materials are separated based on their densities. Milkfat droplets, for example, move towards the rotational axis because they have a lower density than water. Bacteria, which are heavier than water, are drawn away from the rotational axis. Is similar behavior observed during the continuous rotation of fluids within the micro capillaries?

Along with the previously mentioned flow-control parameters such as device geometry, average velocities, viscosity, interfacial tension, and surface chemistry, three

other density-dependent forces emerge during rotational flow of fluids which are also known as Pseudo forces. The pseudo forces comprise the centrifugal force ($F_{centrifugal}$), Euler (F_{Euler}), and Coriolis ($F_{coriolis}$). These are inertial body forces acting on fluids or particles in rotating systems. To clarify the flow manipulation principle in a rotating system, I will go over the three density-dependent forces here. When such density dependent forces exist in rotational fluid flow, the flow is referred to as centrifugal microfluidics rather than rotational microfluidics. The forces exerted on a point-like body (mass density ρ) at position r in a system rotating with angular velocity ω are given in the following equations:

Centrifugal force density, $(F_{centrifugal}) = -\rho\omega \times (\omega \times r),$ *Equation 6*

Euler force density, $(F_{Euler}) = -\rho\left(\frac{d\omega}{dt}\right) \times r$, and   *Equation 7*

Coriolis force density, $(F_{coriolis}) = 2\rho\omega \times V.$ *Equation 8*

To study the flow of fluids in a rotating system with angular velocity (ω), the Navier-Stokes-Equation derived for a non-rotating system can be modified by including the effect of density dependent forces, i.e.

$$\rho\left[\frac{\partial}{\partial t}V + (V.\nabla)V\right] = -\nabla P + \mu\nabla^2 V - \rho\omega \times (\omega \times r) - \rho\left(\frac{d\omega}{dt}\right) \times r - 2\rho\omega \times V. \;\; \textit{Equation 9}$$

Here, r denotes the radial position, ρ the mass density and V the velocity of the fluid. The terms in the right side $\rho\omega \times (\omega \times r)$, $\rho\left(\frac{d\omega}{dt}\right) \times r$, and $2\rho\omega \times V$ represent the centrifugal, Euler and Coriolis effect, respectively. For the common situation where the velocity vector ω is perpendicular to the other two vectors r and V, the numerical values

for the centrifugal force density, Euler force density and Coriolis force density can be

expressed as: $F_{centrifugal} = \rho\omega^2 r$, $F_{Euler} = \rho r\left(\frac{d\omega}{dt}\right)$ and $F_{coriolis} = 2\rho\omega V$.

Figure 15

Centrifugal Microfluidics
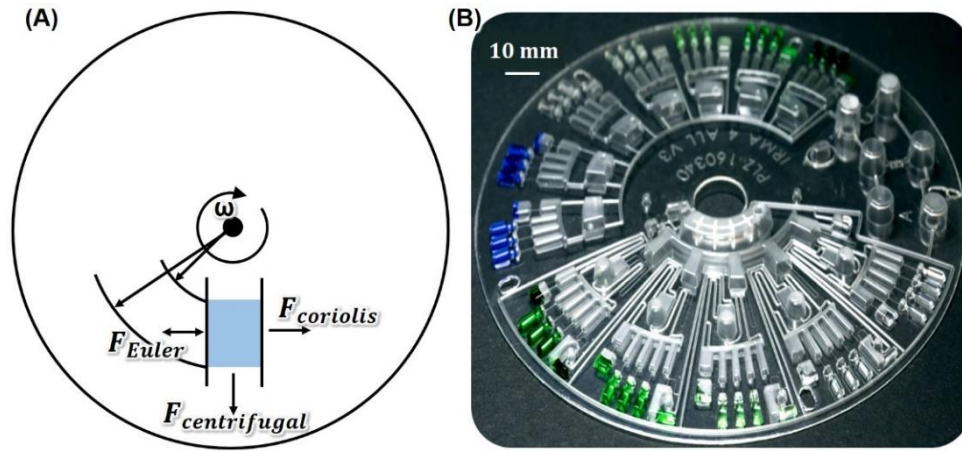
Note. (A) Schematics depicting the direction of the Centrifugal force, Coriolis force and

Euler force in a continuously rotating disk. (B) A micrograph of the microfluidic device

(lab on a disc) containing multiple channels designed for serial dilution of liquids. In the

front, decreasing intensity of green ink from left to right visualizes the result of the

automated serial dilution. (adapted from [58])

In the fields of biology, medical diagnostics, and material synthesis and separation

research, centrifugal microfluidic or lab-on-a-disc platforms[59] have been widely

employed by manipulating the influence of centrifugal, Coriolis, and Euler force effects. Most of the research works in centrifugal microfluidics are performed by using Lab on a disk platform (Figure 15B). By incorporating the channels assays and various forces, centrifugal microfluidics has been investigated for different unit operations of fluids such as pumping,[59] valving,[60][61][62] siphoning,[63] mixing [64][65] of different kind of fluid materials. However, continuous generation of microfibers, microbeads, hydrogel particles, and emulsion droplets by influencing the effects from centrifugal force, Coriolis forces and Euler force has not been investigated in detail.

In 2017, Yashuda et. al suggested a microfluidic twisting approach (Figure 17) based on fluid extrusion in a planetary centrifuge.[66] The planetary centrifuge can produce orbital rotation and axial spin at the same time, comparable to planets orbiting a fixed star. They successfully fabricated the hydrogel beads and twisted microfibers.

Figure 16

Schematic Depiction of Twisting Microfluidics by Using the Planetary Centrifuge
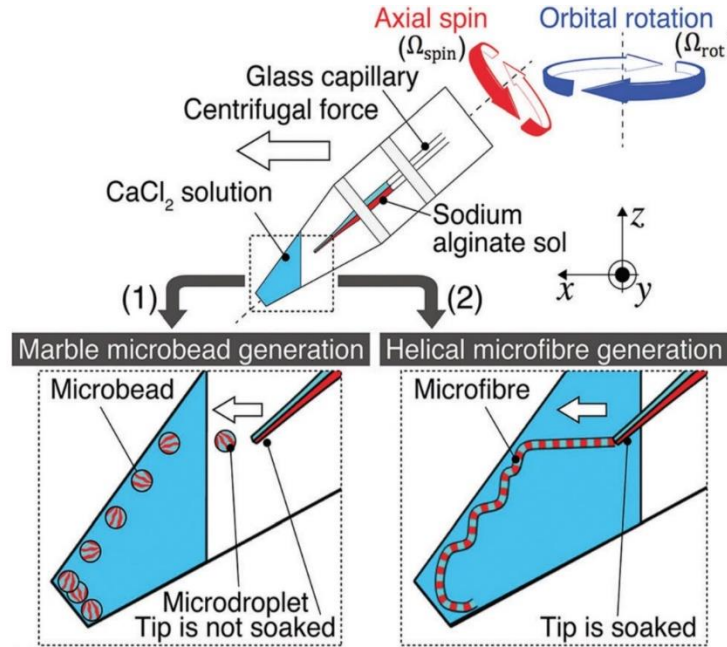
Note. The generation of twisted microbeads and microfibers are shown respectively in 1 and 2 (adapted from [66]).

The centrifugal force effect in microfluidic channels with actively rotating channel walls has another potential which not been investigated in detail. This dissertation presents a new microfluidic method to create helical flow of fluids by actively rotating micro capillaries (Figure 17) and later used to fabricate ropes made of STrIPS bijels in a continuous fashion

Following a broad and detailed discussion of background research on bijels, including fabrication methods, current research directions and relation with the

microfluidics, I will move on to the main topic of my PhD dissertation. First, I will discuss about our work on fabricating STrIPS bijels in a helical flow field (Chapter 3), and then I will show how to assemble a numerous helical STrIPS bijels by controlling the centrifugal force effect (Chapter 4). Finally, in Chapter 5, I will demonstrate how to use selective polymerization methods to create composite bijel ropes with high tensile strength. In addition, I will discuss composite hydrogel ropes derived from the bijel route.

Figure 17

Pseudo Forces in a Rotating Channel
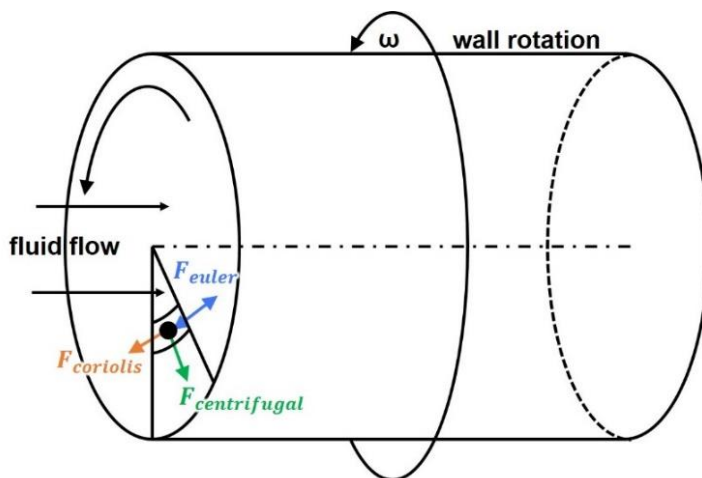
Note. A schematic representation to illustrate the capillary rotation and the direction of the Pseudo forces in the fluids during rotation.

Chapter 3

Microfluidic Twisting Production of Bijel Fibers

Some of the text and figures are reproduced and adapted with permission from the journal, Kharal, S.P., Hesketh, R.P., and Haase, M.F., "High-tensile strength, composite bijels through microfluidic twisting", Advanced Functional Materials, 30, 2003555, 2020, reference [67].

3.1 Introduction

Helices are ubiquitous structures in nature and technology. Their significance lies in their space saving configuration with importance both for macroscopic objects such as compact helical staircases, and for molecules such as the double helix of DNA with high genetic information density. While molecular or colloidal helices can be assembled by entropy,[46][47] molecular chirality,[49][50][51] DNA origami and vapor deposition techniques, [48][45] helices made of larger fibers can be obtained for example via the liquid rope coiling effect.[68][69]

Traditionally, ropes are fabricated by attaching the ends of multiple filaments to rotating tools, which twist them around each other.[70] This millennia old technique continuous to be applied for the bundling of electro spun nanofibers into micro ropes.[52] Simultaneous nanofiber extrusion and bundling has been realized by either rotating fiber collection substrates, or rotating fiber extrusion nozzles.[53][71] However, rope collection follows a batch protocol with limitations on the final bundle length. Moreover, the techniques are not applicable to delicate fiber materials that break easily upon mechanical load.

35

Here, we introduce an *in-situ* technique to continuously twist fibers into ropes in a single step fashion. Our technique relies on applying well defined hydrodynamic shear stresses and can be applied to combine fibers with different material properties.

We demonstrate hydrodynamic twisting for the bundling of fibers made of bicontinuous interfacially jammed emulsion gels (bijels)[7][8][36] formed by Solvent Transfer Induced Phase Separation (STrIPS).[9] Twisting bijel fibers into ropes introduces a versatile reinforcement strategy with manifold potentials. In this chapter, we analyze the hydrodynamic stresses during twisting and discover a subtle balance between axial and rotational forces. Controlling these allows for the formation of micro ropes with adjustable geometry.

3.2 Materials

Ludox TMA suspensions, CTAB (Bio Ultra > 99%), and diethyl phthalate (DEP) (99: 5%) were purchased from Sigma-Aldrich and used as received. Pure Water and pure ethanol (200% proof > 99: 5%) were used for all experiments.

3.3 Preparation of Suspension Solution

The ternary liquid mixture comprises 6 components: (i) pure ethanol (ii) a solution of 200 mM CTAB in ethanol (iii) Ludox TMA at pH 3 (iv) Ludox TMA particles in ethanol at pH 3 (v) pure water and (vi) DEP.

3.4 Microfluidics

The following is a step-by-step breakdown of the device fabrication technique.

Step-1: Four round-cross-section glass capillaries (50 μm inner diameter (ID) and 80 μm outer diameter (OD)) are each inserted into a round-cross-section capillary with an

ID of 100 μm and an OD of 170 μm. The capillaries are glued together using UV Norland 81 adhesive glue (Figure 18A (i-iii)) and a handheld UV-lamp. The 4 combined capillary assemblies are inserted in a larger outer round-cross-section capillary (Figure 18A iv-v)), which has an ID of 0.45 mm and an OD of 1 mm. After symmetrically aligning the inserted capillaries around the central axis of the round capillary of ID 0.45 mm, a drop of UV Norland 81 is applied around the middle of the extrusion capillary to bind them together (Figure 18A(vi)).

Step-2: In order to inhibit bonds between PDMS bearing and glass surface, the capillary surfaces are treated with tridecafluoro−2− (tridecafluorohexyl) decyltrichlorosilane. This task is performed in multistep fashion. First, the capillaries are washed in water plus 5% alkaline dish soap, sonicate for 2−5 minutes in the solution, and then air dry to reduce particles from the glass surfaces. Second, the glass surfaces are etched overnight (> 12 hrs.) in base bath solution (NaOH solution in Iso-propanol) to make capillaries more smooth. Third, the capillaries are cleaned with extensive DI water, and then air-dried capillaries are placed in Piranha acid [Conc. Sulfuric acid + Hydrogen Peroxide (3:1 volume ratio)] solution for at least 30 minutes in order to increase OH surface amount. Four, after cleaning with extensive DI water and drying with Nitrogen gas, the capillaries are treated in a solution of perfluromethyldecalin (3.98 ml) and tridecafluoro−2− (tridecafluorohexyl) decyltrichlorosilane (20 μl) > 48 hours.

Step-3: Figure 18Bi and 18Bii shows a fluorocarbon-treated round-cross-section capillary with an ID of 0.8 mm and an OD of 1 mm and a normal (untreated) square-cross-section capillary of ID 1.05 mm and OD of 1.40 mm. The round-cross-section capillary with 0.8 mm ID is inserted into the square capillary as shown in the Figure

18B(iii). Polydimethylsiloxane (PDMS) is next introduced in the region not occupied by the round and square capillaries Figure 18B(iv). The PDMS is cured for 20 minutes at 150 °C. Inside the PDMS bearing, the fluorocarbon-treated capillary can freely revolve on its axis. The capillary combination built in Figure 18B(iv) is subsequently placed from the right side into a holder square capillary, as shown in Figure 18B(v).

Figure 18

Step-By-Step Illustration for Making a Microfluidic Device
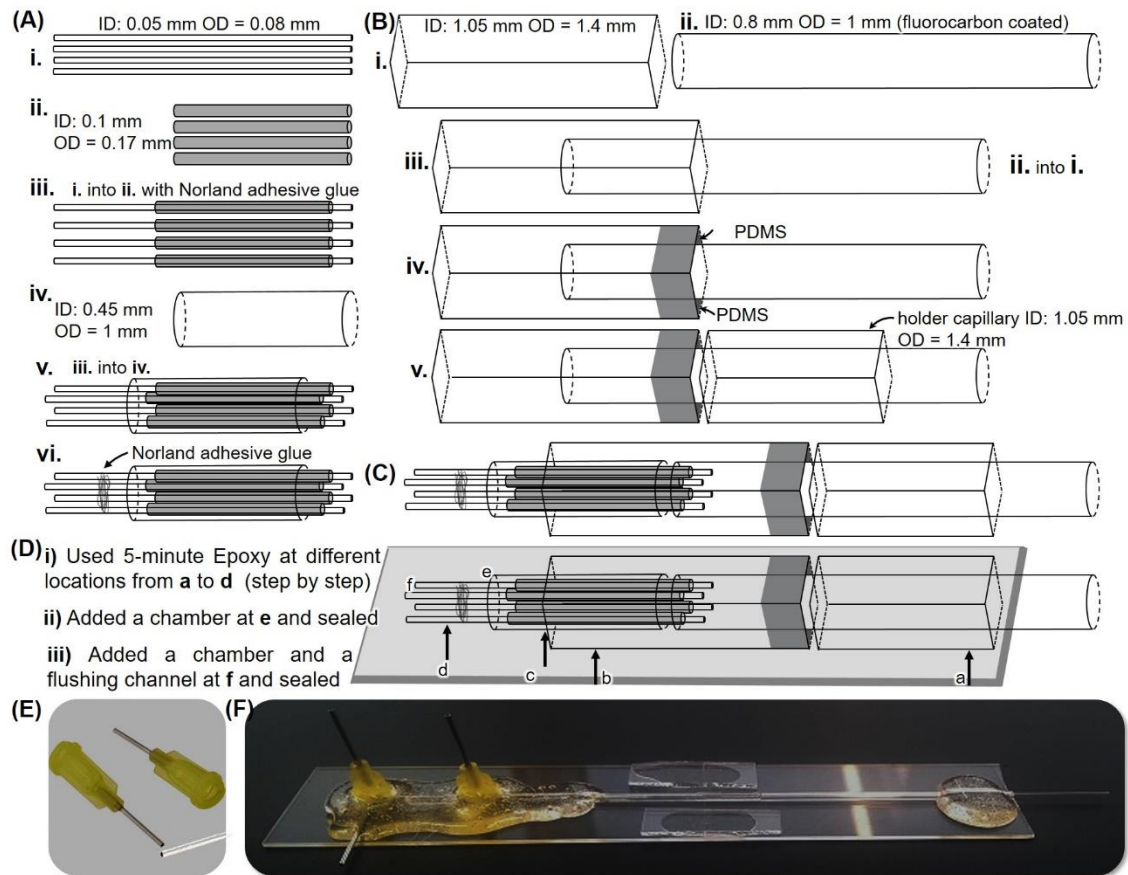
Note. (A) Capillary assembly to generate four fibers. (B) Capillary combination to create rotational flow in the flow channel. (C) Combination of (A) and (B). (D) Capillary assembly gluing stage on a microscope slide. (E) Dispensing needles that serve as injection chambers and flushing channel. (F) A micrograph of the microfluidic device after all the flow channels have been glued in place.

Step-4: The capillary combination shown in Figure 18A(vi) is then inserted into the capillary combination shown in Figure 18B(v). The entire capillary assembly (Figure 18C) is then mounted on a microscope slide and sealed with 5-minute epoxy (Devcon) glue (Figure 18D).

To inject fluids, we added one chamber with a flushing channel (ID 0.66 mm and OD 0.91 mm) at the inlet of 50 micrometer capillaries, and another chamber with a flushing channel at the inlet of 0.45 mm ID round capillary. The stainless-steel dispensing needles as illustrated in Figure 18E were used as chambers to get the final product (Figure 18F).

Step-5: We used different Lego parts to build a rotating device to twist bijel fibers, as illustrated in Figure 19(A-C). The motor (EV3 large servo) connected with the multiple gears (2 large gears with 40 tooths and 2 small gear with 8 tooths) can be programmed to control the rotation speed.

In addition, the Lego racket with numerous gears can slide in separate locations, allowing different sections of the fiber to be visualized during the experiment (Figure 19(B-C)). The most essential step is to connect the microfluidic device to the Lego racket's rotating gear. To do so, we create a tunnel of 1 mm diameter in the center of the axle pin

that fits inside the rotating gear, as shown in Fig 19D(i-iii). We place the free end of the fluorocarbon tube in the microfluidic device into the tunnel of the axle pin once all of the gears in the racket are connected. The microfluidic device is next aligned straight and bonded with the axle pin using 5 minute epoxy resin, as shown in Fig 19D(v). The complete design of the device including both the microfluidic device and rotating system is shown in the Figure 19E.

Figure 19

Lego Based Rotating System
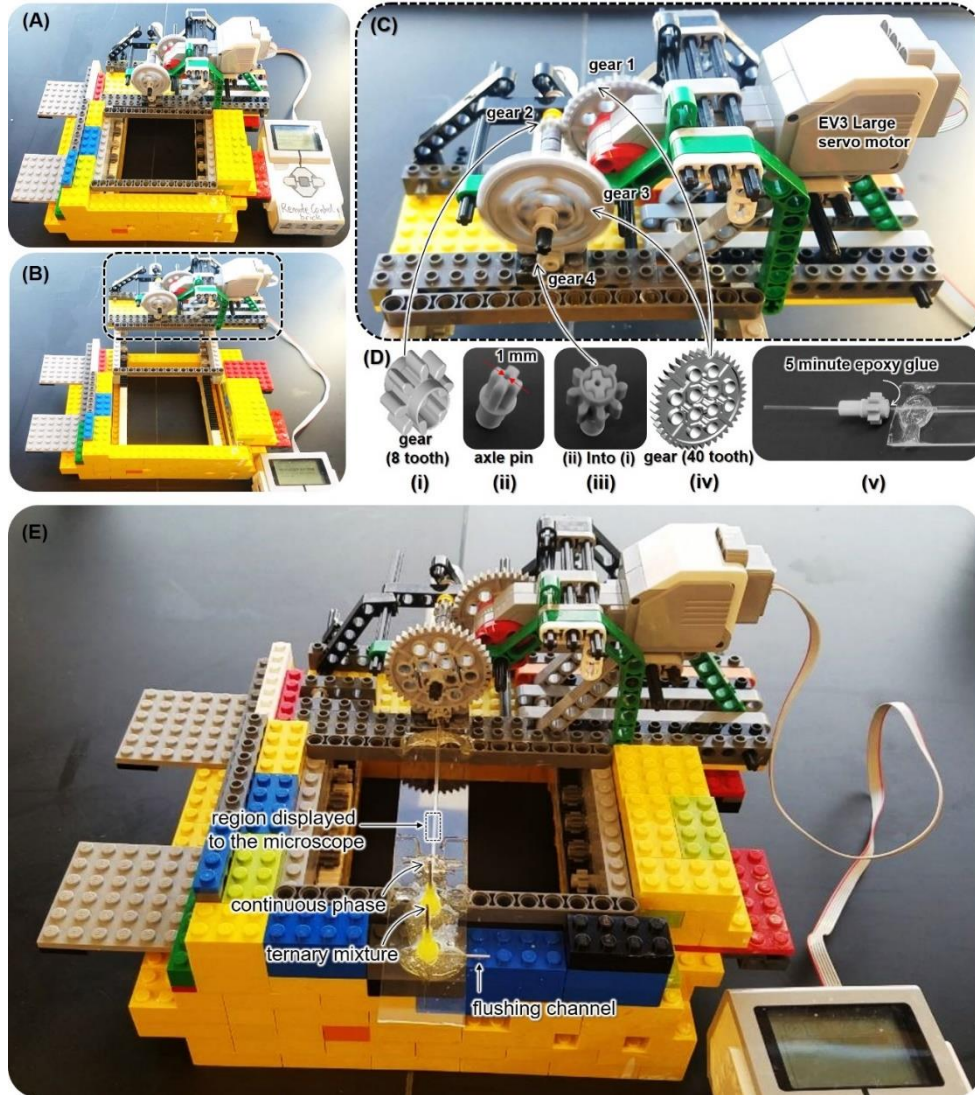
Note. (A) Lego-based rotating system with programmable DC motor. (B) The rotating system with multiple gears can slide to different locations on demand and a zoomed in view of the rotating system is shown in (C). (D) Illustration of how we connect device with the rotating system. (E) Rotating system with microfluidic device in its final configuration before injecting fluids to generate fibers.

41

To prevent the cohesion of bijels on the glass capillary surfaces during experiment, we coat the flow channel with PDADMAC (Poly(diallyldimethyl ammonium chloride)). To this end, we inject a PDADMAC solution (2 g/L of PDADMAC including NaCl concentration of 0.5 mol/L) into the device. Afterwards, excess PDADMAC solution is flushed with DI water and the device is dried with air.

Figure 20

A Schematic Illustration Demonstrating How We Carried Out the Experiments and Studied the Bijel Ropes
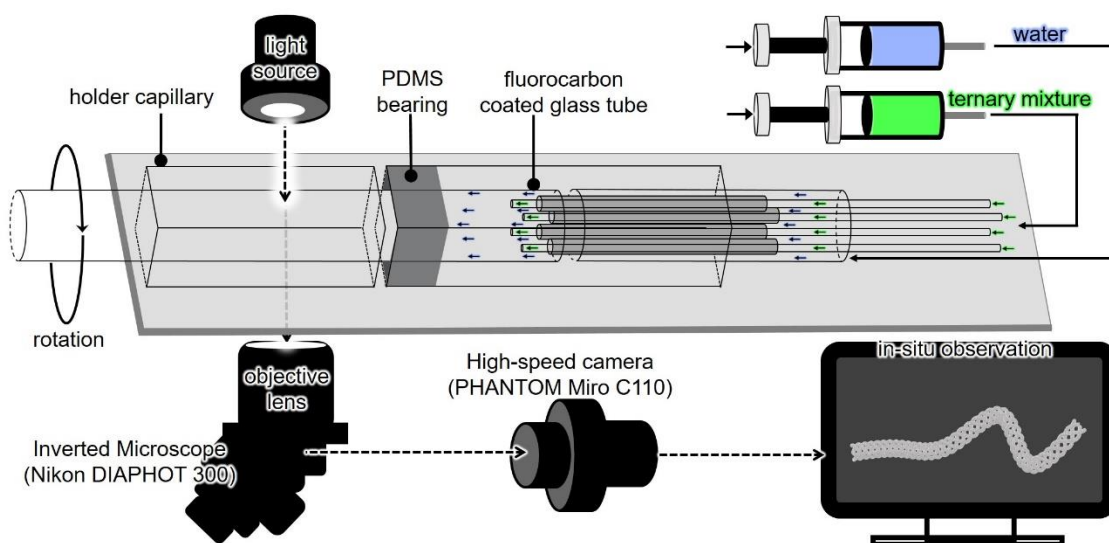
To extrude bijel fibers, water is pumped into the inlet connected to the 0.45 mm ID and 1 mm OD round capillary. A ternary liquid mixture is injected through the chamber connected to the inlet of the four glass capillaries (ID 50 μm), resulting in four parallel

fibers. Figure 20 depicts our experimental setup how we conducted the experiment. Using an inverted light microscope (Nikon Diaphot300) equipped with a high-speed camera (Phantom Miro C320), the in-situ production of the fibers and ropes is captured. By simply blocking specific extrusion nozzles during the fabrication of the device, the desired number of fibers (1 to 4) can be generated. By blocking the other three extrusion capillaries in the four-fiber combination, for example, a single fiber can be produced.

3.5 Steady State Ropes

To obtain bijel fiber helices, a coaxial extrusion device is employed (Figure 21A). The device is composed of four glass capillaries centered in a larger outer capillary. Water is pumped through the outer capillary by means of a syringe pump. Four parallel fibers are obtained by flowing a ternary liquid mixture composed of oil (diethyl phthalate or ethylene glycol dimethacrylate), ethanol, water, silica nanoparticles and cetyltrimethylammonium bromide (CTAB) under a pressure of 400 kPa through the four glass capillaries into the water stream.

Upon contacting the water stream, the ternary liquid mixture rapidly turns into a viscoelastic fiber, a process termed Solvent Transfer Induced Phase Separation (STrIPS).[9] In brief, ethanol diffuses from the ternary liquid mixture into the surrounding water. The rapid loss of ethanol causes water and diethyl phthalate (DEP) to phase separate.

During STrIPS, CTAB modified nanoparticles accumulate on the interface between DEP and water, rigidifying the interface by jamming. The resulting structure is named bicontinuous interfacially jammed emulsion gel (short bijel).[7] The bijel is composed of a bicontinuous oil/water channel network and stabilized by a percolating film of nanoparticles.[8][36]

Bijel fibers are twisted into a helix by rotating the larger capillary around its own axis via a DC motor (Figure 21B). The rotating capillary is mounted in a polydimethoxysilane (PDMS) bearing to facilitate leak proof operation. Smooth rotation in the PDMS bearing is possible because of the lubrication provided by a coating of tridecafluoro-2-(tridecafluorohexyl) decyl trichlorosilane on the outer capillary, inhibiting bonding between the glass surface and the PDMS bearing. Figure 21C shows a micrograph time series of fiber extrusion and helix formation upon outer capillary wall rotation.

Figure 21

Principle of In-Situ Hydrodynamic Twisting
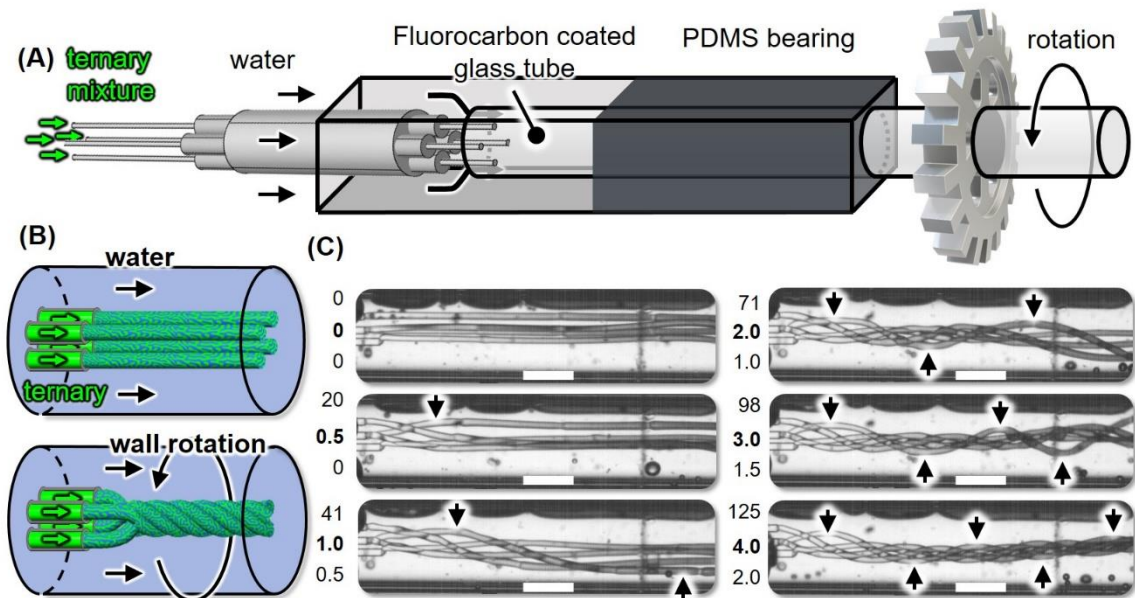
Note. (A) Schematics of the microfluidic device. A combination of capillaries with square and round cross-sections and different sizes are interdigitated and sealed with glue. A gear

is connected to the rightmost capillary to allow for rotation. (B) Schematics of bijel fiber helix formation upon activating the rotation of the outer channel wall. (C) Micrograph time series of helix formation upon initiation of the wall rotation at 1900 rpm for a water flow rate of 1 ml/min. Each micrograph has three numbers on the left, representing (top to bottom) (i) time in milliseconds, (ii) number of wall rotations, (iii) number of fibers twisted around the central axis. The arrows indicate half period (upward arrow) and full period (downward arrow) of the twisting for one selected fiber. All scale bars are 0.5 mm.

Twisting of fibers begins near the extrusion nozzles immediately after the rotation has been initiated. After 1 rotation of the outer cylinder the fibers have twisted half a period around the central axis (indicated by arrows). With the second wall rotation completed the fibers have twisted a full period around the central axis. This trend continues with each wall rotation adding another half period. Simultaneously, the fiber bundle becomes tighter indicated by a decreasing pitch length (horizontal length of a full twist): At 1 wall rotation the pitch length is 4.4 mm, at 2 wall rotations 2.0 mm and at 4 wall rotations it reaches a steady state value of 1.4 mm.

As expected, the rotational speed (revolutions per minutes) controls how tight the rope is twisted. The rope "tightness" is quantified by the helix angle α as depicted in Figure 22. The helix angle (α) can be calculated by measuring the bundle radius (r) and repetition length (H) through the following equation: $cos\alpha = \left[\left(\frac{r}{h}\right) + 1\right]^{-\frac{1}{2}}$ where, $H = 2\pi h$ is the helix-pitch (repetition length) and r = D/2 the bundle radius. Two example

measurements of the helix radius (r) and the helix pitch (H), as well as a schematic for the calculation are provided in Figure 22.

Figure 22

Example Measurements of the Helix Radius and the Helix Angle
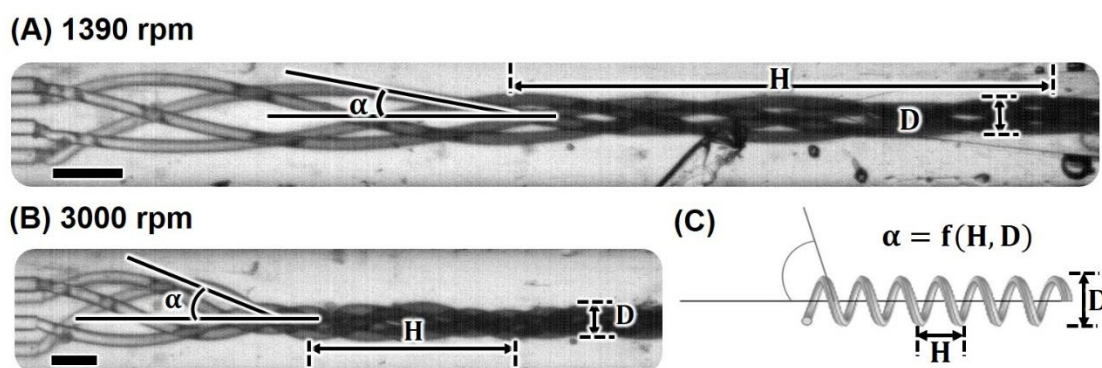
Figure 23A shows micrographs of steady state bundles at different *rpm*, constant water flow rate Q_w of 0.8 ml/min and ternary mixture pressure of 400 kPa. Increasing from 1390 *rpm* to 3000 *rpm* results in a linear increase of α from 10° to 27° (Figure 23C).

Interestingly, the rope geometry also depends on the water flow rate. Figure 23D shows micrographs of steady state fiber bundles at different Q_W, constant *rpm* of 3000 and ternary mixture pressure of 400 kPa. The ropes become progressively tighter with decreasing Q_w. The helix angle α decreases linearly from 37° at 0.5 ml/min to 18° at 1 ml/min (Figure 23E).

By adjusting the capillary nozzle organization ropes with different number of fibers can also be extruded. Micrographs of ropes having 3 fibers and 5 fibers are shown in the Figure 24 and Figure 25, respectively.

Figure 23

Hydrodynamic Study of Steady State Ropes (4 Fibers)
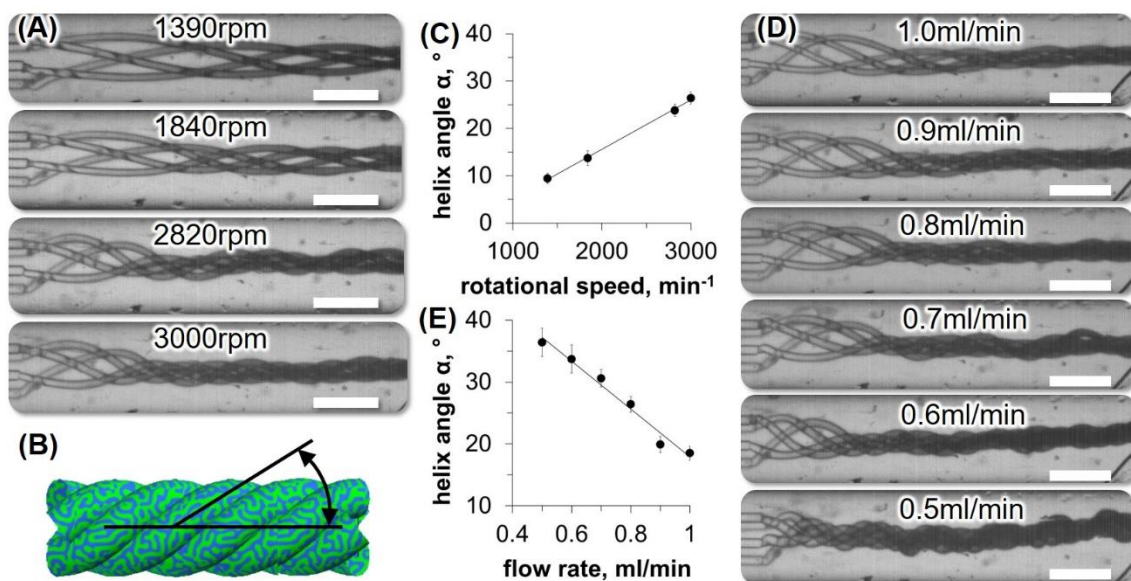
Note. (A) Micrographs for different rotational speeds (rpm) at constant water flow rate of 0.8 ml/min (B) An animation to depict helix angle measurements (C) Variation of helix angle against rpm (D) Micrographs for different flow rates at constant rotational speed (3000 rpm). (E) Variation of helix angle against water flow rate. All the scale bars are 0.5 mm.

As observed in the case of 4 fibers ropes, the tightness in 3 and 5 fibers can be controlled by varying the water flow rate (Q_W) and the outer wall rotation (rpm). The variation of helix angle looks similar in the case of 3, 4 and 5 fibers bundle. However, 5 fibers bundle exhibit higher helix angle while in comparison with the 3 and 4 fibers rope even at the similar flow rate and rotational speed.

Figure 24

Hydrodynamic Study of Steady State Ropes (3 Fibers)

Note. (A) Micrographs for different rotational speeds (rpm) at constant water flow rate of 0.8 ml/min (B) (i) Capillary nozzle organization (ii) Front view of the bundle (iii) An animation to depict helix angle measurements (C) Variation of helix angle against rpm (D) Micrographs for different flow rates at constant rotational speed (3000 rpm). (C) Variation of helix angle against water flow rate. All scale bars are 0.5 mm.

Our results show that the rope tightness depends on two control parameters: (i) rpm, and (ii) Q_W. This indicates a balance between forces in rotational and in flow direction. In the following, we approximate the forces acting on the fiber bundle based on a hydrodynamic model.

Figure 25

Hydrodynamic Study of Steady State Ropes (5 Fibers)

Note. (A) Micrographs for different rotational speeds (rpm) at constant water flow rate of 0.8 ml/min (B) (i) Capillary nozzle organization (ii) Front view of the bundle (iii) An animation to depict helix angle measurements (C) Variation of helix angle against rpm (D) Micrographs for different flow rates at constant rotational speed (3000 rpm). (C) Variation of helix angle against water flow rate. All scale bars are 0.5 mm.

3.6 Velocity and Shear Stress Profile on the Bijel Fibers Ropes

The calculations derived in the appendix A and B provides an analytical solution for the shear stress along θ direction ($\tau_{r\theta}$) and Z direction (τ_{rZ}). We considered the rope as inner solid cylinder with radius R_1, rotating along the θ direction with angular velocity ω_1, and translating along the Z direction with linear velocity U. The cylindrical channel has radius R_2 rotating with angular velocity ω_2, as shown in the Figure 26.

Figure 26

Schematic Demonstration to Study Flow Dynamics During Bundle Formation

(A)
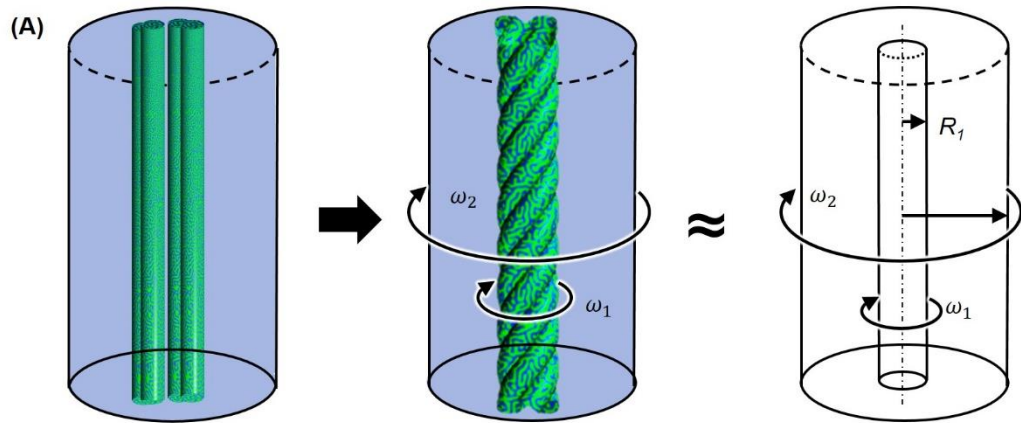
(B) Boundary conditions:
translation direction: (i) at $r = R_2$, $v_z|_{r=R_2} = 0$ (ii) $at\ r = R_1$, $v_z|_{r=R_1} = U$
rotation direction: (i) at $r = R_2$, $v_\theta|_{r=R_2} = \omega_2 R_2$ (ii) $at\ r = R_1$, $v_\theta|_{r=R_1} = \omega_1 R_1$

(C) Analytical equations:

$(i)\ [v_z] = -\dfrac{dp}{dz}\dfrac{R_2^2 - r^2}{4\mu} + \left[U + \dfrac{\frac{dp}{dz}(R_2^2 - R_1^2)}{4\mu}\right]\ln\left(\dfrac{R_2}{r}\right)/\ln\left(\dfrac{R_2}{R_1}\right)$ $\qquad (ii)\ [\tau_z] = \dfrac{\mu(U_0 - U)}{R_1}\,1/\ln\left(\dfrac{R_2}{R_1}\right)$

$(iii)\ [v_\theta] = \left(\dfrac{R_2^2}{R_2^2 - R_1^2}\right)\left[r\left(\omega_2 - \dfrac{\omega_1 R_1^2}{R_2^2}\right) - \dfrac{R_1^2}{r}(\omega_2 - \omega_1)\right]$ $\qquad (iv)\ [\tau_\theta] = -\dfrac{2\mu R_2^2 R_1^2(\omega_2 - \omega_1)}{(R_2^2 - R_1^2)} \times 1/r^2$

Note. (A) Left: 4 parallel fibers inside the flow channel Middle: rope formation upon activating outer wall rotation Right: Simplified hydrodynamic model where the rope is

assumed as a rotating solid cylinder. Boundary conditions as well as final analytical equations are shown in (B) and (C) respectively.

In the simplified model, the flow space for the water around the bijel rope is approximated as a cylindrical annulus. The outer wall rotates uniformly with angular velocity ω_2 around the axis of a centered cylinder. The centered cylinder approximates the shape of the bundle, which itself rotates with angular velocity ω_1 and translates with velocity U. The bundle surface velocities U can be determined by measuring the movement of irregularities on the fiber surface via high-speed video-microscopy.

3.7 Surface Velocity Measurements

Figure 27

Micrographs to Demonstrate How We Calculated Bundle Surface Velocity
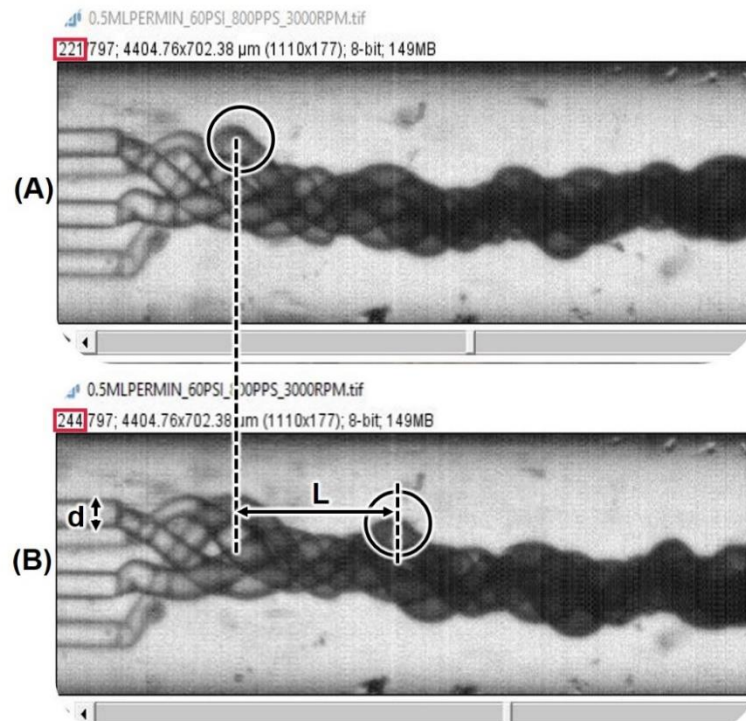
The method of bundle surface velocity measurement is described as follows:

Let us suppose, number of frames per second $= x$, time of 1 frame $= 1/x$ seconds, time that passes during y frames $T = y/x$ seconds. The travel distance L can be measured by tracking the travelling distance of irregularities on the fiber surfaces. The linear velocity calculates to $U = L/T$. An example measurement is shown in Figure 27.

For the calculation of shear stress along the translation direction Z, we have performed measurements of rope surface velocity U at steady state. The results are plotted in the Figure 28 and used for our calculations of the shear stress on the bundle surface. For a given Q_T and rpm, U increases approximately linearly with Q_W (see Figure 28A). U also depends on the capillary orientation.

For a given Q_T and rpm, D decreases approximately linearly with Q_W. The extrusion of a bijel fiber depends on the combination of the volumetric flow rates of the ternary mixture (Q_T) and the water phase (Q_W). This combination controls the shear stress on the fiber surface. By increasing Q_T at a constant Q_W, the shear stress exerted from the water phase on the fiber surface reduces. The effect of increasing Q_T on the fiber extrusion is shown in Figure 28C.

At low Q_T the high shear stress causes periodic fiber pinch-off due to yielding of the fiber. Continuous extrusion of uniform fibers takes place at intermediate Q_T. At high Q_T the shear stress is insufficient to facilitate uniform fiber extrusion. This dependence has been analyzed in detail in the study by Haase et al.[39] The limitations imposed by the fiber yielding at low Q_T and nonuniform fiber extrusion at high Q_T restricts our experimental range for rope formation. It is possible to increase Q_T and still extrude uniform fibers, but

then also Q_W needs to be increased. However, to maintain the same twist angle an increase

of Q_W requires an increase of the rotational speed of the capillary (rpm). The simultaneous

increase of Q_T, Q_W and RPM does not change the rope size, but the rope extrusion speed.

Figure 28

Rope Velocity and Diameter Against Water Flow Rates
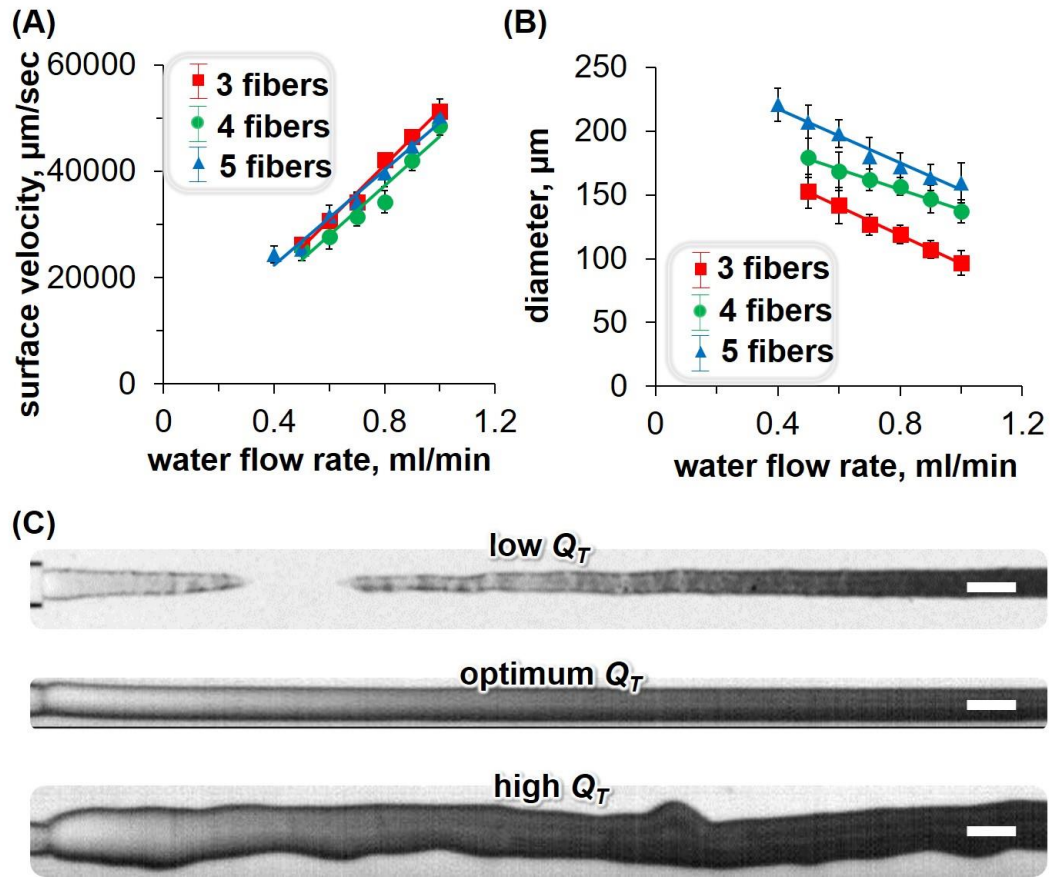
Note. (A) Measurements of the bundle surface velocity (*U*) plotted against water flow rate

(Q_W) (B) Measurements of the bundle diameter (*D*) plotted against water flow rate (Q_W)

(C) Micrographs to demonstrate the effect on fiber size.

For the calculation of shear stress along the rotation direction, we have performed measurements of rotation frequency ω_1 of the ropes by considering steady states. The results are plotted in the Figure 29. The graph shows that the bundle rotation frequency ω_1 depends linearly with the frequency of the outer wall rotation ω_2.

Figure 29

Bundle Rotation Frequency (Rpm) Vs. Wall Rotation Frequency (Rpm)
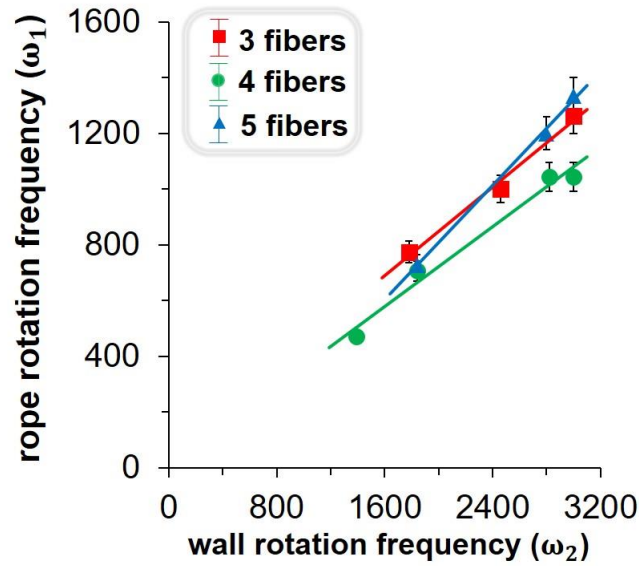
3.8 Helix Angle Dependence on Shear Stress Ratio

The shear stress ratio $\tau_{r\theta|R_1}/\tau_{rz|R_1}$ is defined to approximate the forces on the rope surface. The dependence of α on the shear stress ratio is approximately linear in the studied range and shows the combined effect of the hydrodynamic forces. Interestingly, for all experiments, $\tau_{r\theta|R_1}/\tau_{rz|R_1}$ is always smaller than 0.2, indicating that hydrodynamic forces

in axial direction dominate over the rotational shear stresses. When $\tau_{r\theta|R_1}/\tau_{rz|R_1}$ is gradually increased from 0.05 to 0.18, α increases from 10° to 37° (Figure 30).

An alternative representation of the shear stress ratio is given by the angle β, which represents the direction of the resulting vector with the components $\tau_{r\theta|R_1}$ and $\tau_{rz|R_1}$. A plot of α against β is shown in the inset of Figure 30C. The slope of this linear dependence can be interpreted as the resistance of the fibers against twisting, which is likely a function of the fiber bending modulus, as well as the packing constraints in the rope. However, additional experimental research probing the dependence of the slope on the fiber material properties is needed to develop an analytical prediction. The variation of helix angle against shear stress ratio and the direction of the resulting vector for 3, 4 and 5 fibers rope are shown in the Figure 31A and Figure 31B, respectively.

Figure 30

Helix Angle Against Shear Stress Ratio
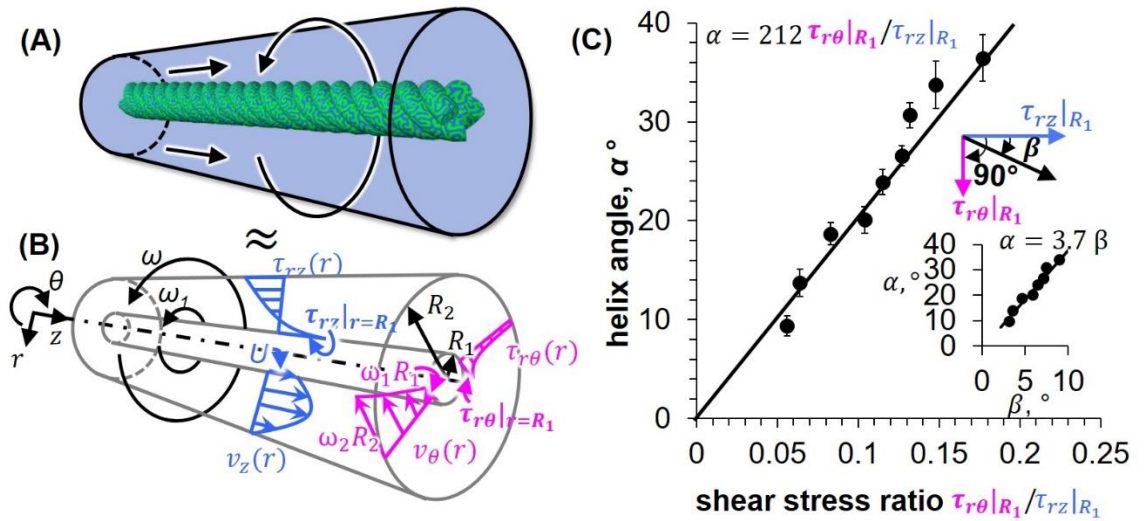
Note. **(A) 3-**Dimensional depiction of bijel bundle in flow channel with arrows indicating flow direction of water and rotation direction of outer wall **(B)** cylindrical annulus geometry used to approximate fiber rope in channel for hydrodynamic calculations. **(C)** Measurements of the helix angle α plotted against calculated values for the shear stress ratio $\tau_{r\theta}|_{R_1}/\tau_{rz}|_{R_1}$. Error bars correspond to the standard deviation of 5 measurements. The inset shows a schematic of the angle β and the variation of α with respect to β.

Figure 31

An Alternative Representation of Shear Stress Ratio
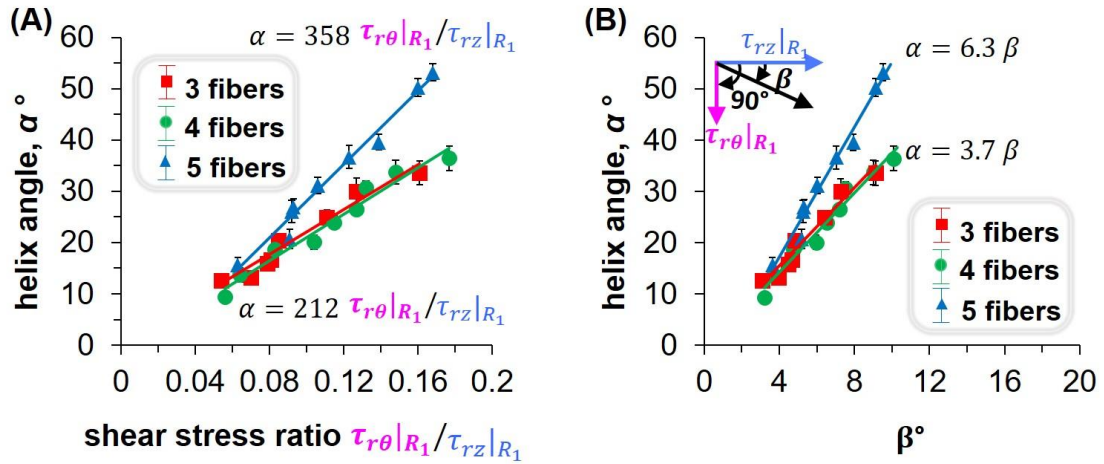
Note. **(A)** Measurements of the helix angle α plotted against calculated values for the shear stress ratio $\tau_{r\theta}|_{R_1}/\tau_{rz}|_{R_1}$ for 3, 4 and 5 fibers bundle together. **(B)** Measurements of the helix angle α plotted against the calculated values of β for 3, 4 and 5 fibers rope. Error bars correspond to the standard deviation of 5 measurements.

3.9 Pitch Length and Rope Diameter Against Shear Stress Ratio

We compared rope diameter (D) with respect to shear stress ratio ($\tau_{r\theta|R_1}/\tau_{rz|R_1}$) which shows that D increases approximately linearly with increase in the shear stress ratio (Figure 32A). Also, we performed measurements for the linear distance (H) travelled by each fiber during one twist at steady state. The pitch length (H) is plotted against the shear stress ratio ($\tau_{r\theta|R_1}/\tau_{rz|R_1}$) which is shown in the Figure 32B. The pitch length decreases approximately quadratically with increase in the shear stress ratio.

Figure 32

Rope Diameter and Pitch Length Against Shear Stress Ratio
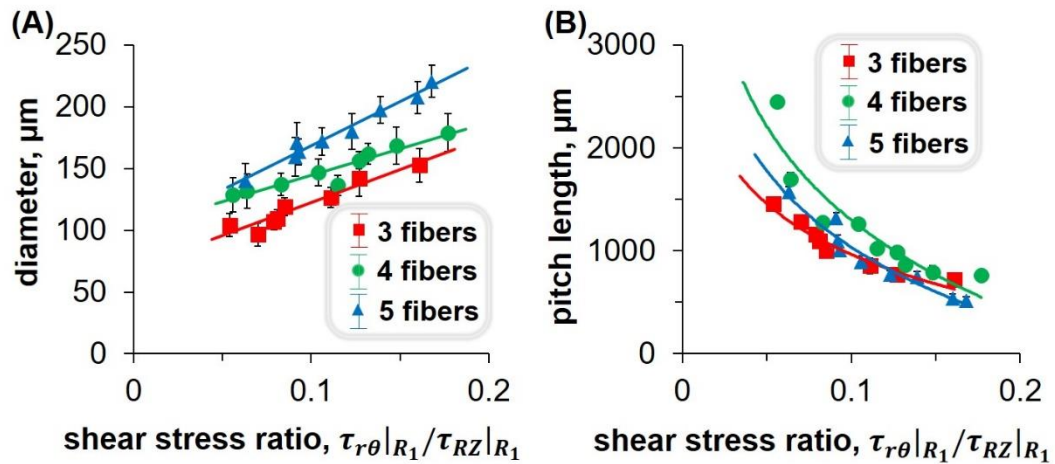
Note. (A) Measurements of the diameter (D) of the twisted fibers against values of the shear stress ratio ($\tau_{r\theta|R_1}/\tau_{rz|R_1}$). **(B)** Measurements of the pitch length (H) of the twisted fibers against values of the shear stress ratio ($\tau_{r\theta|R_1}/\tau_{rz|R_1}$).

3.10 Ropes with Larger Diameter Exhibit Higher Helix Angle

The measurements of the diameter (D) are also compared with the measured values of the helix angle. The measurements of the diameter (D) are also compared with the measured values of the helix angle (α) which shows that the bundles with higher D also exhibit higher α (see Figure 33A). It means 5 fibers bundle exhibit higher α than 3 and 4 fibers bundle even at similar values of $\tau_{r\theta|R_1}/\tau_{rz|R_1}$. An illustration is shown in the Figure 33B to visualize the dependencies of bundle diameter against helix angle. The helix angle dependence for 3 and 4 fibers in a bundle is nearly identical, and a single master curve describes both trends. However, for 5 fibers, α increases more steeply with $\tau_{r\theta|R_1}/\tau_{rz|R_1}$. We attribute this to the larger diameter of the 5 fiber ropes. Two effects are at play: bundles with larger diameters require (i) a larger α for the same number of twists and (ii) require a higher number of twists per length (and consequentially higher α) for a closed packed configuration of the individual fibers.

Figure 33

Ropes with Various Diameters and Helix Angle
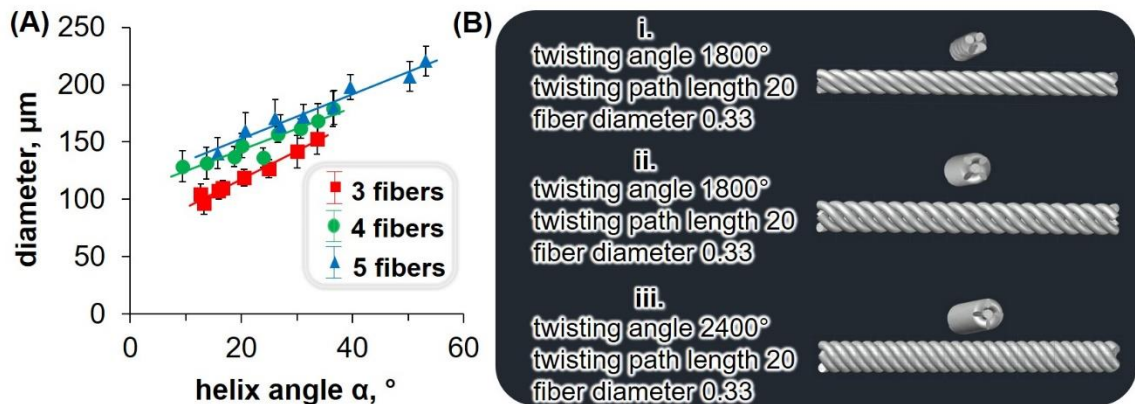
Note. (**A**) Measurements of the bundle diameter plotted against helix angle. (**B**) An illustration to show bundles with higher diameter exhibit higher helix angle. (i) 4 fibers: twisting angle 1800 degrees, twisting path length 20, and fiber diameter 0:33 unit. (ii) 5 fibers: twisting angle 1800 degrees, twisting path length 20, and fiber diameter 0:33 unit. (iii) 5 fibers: twisting angle 2400 degrees, twisting path length 20, and fiber diameter 0:33 unit.

3.11 Inertial Force and Operation Limit for Stable Bundles

To probe the impact of inertial forces we calculated the Reynolds numbers for the water around the fibers in rotational ($R_{e\theta}$) and translational (R_{eZ}) directions (Figure 34). For our experiments with bundles made of 4 fibers $R_{e\theta}$ ranges from $20 - 45$, and R_{eZ} ranges from $10 - 23$. The ratio $R_{e\theta}/R_{eZ}$ increases from 1 to 4 when the helix angle increases from $10 - 38°$. These calculations confirm laminar flow in both directions and that inertial effects are larger in rotational direction.

Figure 34

Helix Angle vs. Reynolds Numbers
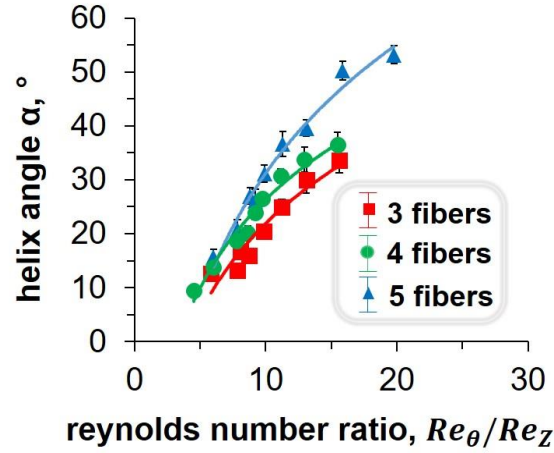
Note. A graph showing variation of helix angle (α) against Reynolds number ratio Re_θ/Re_Z for 3, 4 and 5 fibers bijel bundle.

The flow rate of the ternary mixture Q_T is controlled by the pressure. All experiments are performed at a pressure of 400 kPa. For lower pressures periodic fiber pinch-off occurs due to fiber yielding, while for higher pressures nonuniform fiber extrusion takes place[24]. It is possible to increase Q_T and still extrude uniform fibers, but then also Q_W needs to be increased to maintain enough shear stress. However, in order to obtain significant twist angles an increase of Q_W requires an increase of the *rpm*. The simultaneous increase of Q_T, Q_W and *rpm* increases the bundle extrusion speed at a constant bundle size.

Figure 35

Operation Limits for Bundle Fabrication and Example Micrographs
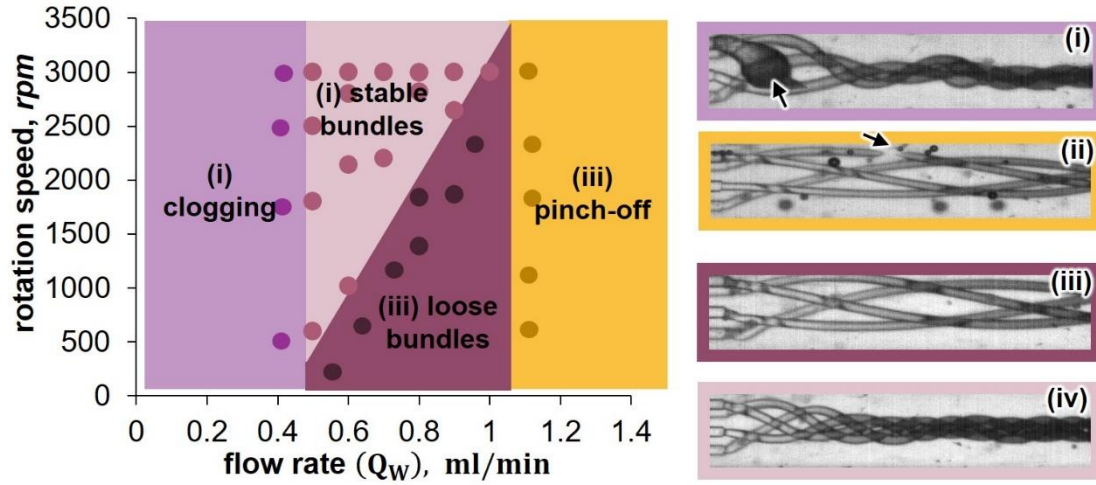
Note. The different colored regions depict 4 distinct phenomena shown in the micrographs on the right. (i) nozzle clogging by the solidifying ternary mixture at $Q_W < 0.5$ ml/min. (ii) fiber pinch-off for high shear rates at $Q_W > 1.0$ ml/min, (iii) loose bundle formation at insufficient rotational shear stress, (iv) stable bundle formation at $500 < $ rpm $ < 3000$ and $0.5 < Q_W < 1.0$ ml/min.

At the constant pressure of 400 kPa for the ternary mixture, stable bundles can be obtained within a range of Q_w from 0.5 ml/min to 1.0 ml/min Outside of this range 3 distinct phenomena are observed: (i) clogging of the extrusion capillary by the solidifying ternary mixture ($Q_w < 0.5$ ml/min), (ii) pinch-off of individual fibers ($Q_w > 1$ ml/min), (iii) loose bundle formation for low rpm values. Figure 35 depicts these operational limits graphically.

3.12 Conclusion

We have introduced microfluidic in-situ twisting to generate bijel fiber bundles. We demonstrate the control of geometrical features of the bundles based on balancing hydrodynamic stresses in rotational and translational directions. The microfluidic twisting method can produce bundles with pitch lengths from 500 µm to 2400 µm and helix angles from 10° to 36°. Microscopic bundles at a rate of 5.6 cm^3/hr can be produced with our device, but higher rates are possible when increasing feed pressure and rotational speed. Our method is suitable for soft fibers with elastic moduli below 1 MPa and yield strengths ranging from hundreds of Pa to MPa. Microfluidic twisting is applicable to fibers made of bijels, reconfigurable printed liquids,[54] hydrogels,[55] capillary suspensions,[72] high-internal phase emulsions or colloidal gels.[73]

Chapter 4

Microfluidic Assembly of Helical Bijel Fibers Via Centrifugal Forces

4.1 Introduction

The control over microfluidic flows is essential for research in biology,[74] cancer therapeutics,[75] medical diagnostics[76] optics,[77] as well as material[78] - and separation science.[79] The simplest microfluidic flow has a parabolic velocity profile. However, microfluidic operations such as mixing,[80] separation,[81] particle sorting and self-assembly,[82] as well as droplet formation[23] require more complex fluid flows. For example, microfluidic channels with herringbone patterned ridges enable transverse flows that can mix fluids chaotically.[83] Rotating flows can also be realized in intravascular 3D passive mixers realized by printing hydrogels via stereolithography.[84] Alternatively to manipulating flows via the channel geometry, fluids can be actively twisted in a microfluidic channel by the movement of the channel wall. A helical flow field results when pumping a liquid through a rotating microcapillary. The resulting forces can for instance be used to coil microfibers around each other.[66][67] Microfluidic fabrication of microfibers made of polymers,[85] hydrogels,[55][86][87] emulsion gels,[57] or phase separated proteins[88] has recently gained more attention due to their applications as building blocks for functional three-dimensional (3D) objects. Actively rotating the microfluidic channel has additional unexplored potentials for the centrifugal assembly or

separation of particles during microfluidic flow. Yet, the centrifugal effect in microfluidic channels with rotating walls has not been investigated in detail.

Here, we show how controlling the centrifugal forces during the flow through a rotating capillary enables the continuous assembly and collection of infinitely long microropes. The assembly and collection of the microropes depends on the direction of the centrifugal force, which is determined by the density difference between the individual rope filaments and the surrounding fluid. The rope filaments in our work are composed of bicontinuous interfacially jammed emulsions gels (bijels) [8][89] formed via solvent transfer induced phase separation (STrIPS).[9][17][13][40] Interestingly, the density of these bijel fibers changes over the course of their formation due to a changing composition during the STrIPS process. The initially low density facilitates microrope assembly, but as the fiber density increases over time the centrifugal force results in collision of the microrope with the rotating capillary wall, damaging the assembled fibers. To understand this transition quantitatively, we introduce a model of the diffusion dynamics, predicting the density increase over time. The prediction of the model agrees well with the observed experimental behavior, confirming the centrifugal effect as the cause of the microrope/wall collision.

4.2 Materials

Ludox TMA suspensions, CTAB (Bio Ultra > 99%), Butyl acrylate (BA), Diethyl phthalate (DEP), and Ethylene glycol dimethacrylate (EDMA) were purchased from Sigma-Aldrich and used as received. Pure Water, Ethanol and Methanol (200% proof > 99: 5%) were used for all experiments.3.3 Preparation of Suspension solution.

4.3 Confocal Microscopy

Fluorescence dye (Nile red) is added to the fiber casting mixture to image the bijels under the confocal fluorescence microscope (IX-73 OLYMPUS connected to Thorlabs confocal scanner). The polymerized bijels are washed with ethanol before being soaked in diethyl phthalate (DEP) for refractive index matching. To observe the bicontinuity in fibers, they are illuminated with blue laser light (488 nm) and imaged using a confocal microscope. We also used Scanning Electron Microscope to image bijel ropes.

4.4 Microfluidics

Microfluidic twisting involves the rotation of a cylindrical capillary (ID 0.8 mm) around its axis. The cylindrical capillary is coated with tridecafluoro-2-(tridecafluorohexyl) decyl trichlorosilane and mounted in a polydimethoxysilane bearing, allowing it to freely rotate without water leakage (Figure 18).

The rotation is controlled with a DC motor, resulting in an angular velocity profile of water over the capillary radius (Figure 19). Simultaneously, water is pumped through the capillary by means of a syringe pump, generating an additional parabolic fluid velocity distribution in axial direction (Figure 20). 3-dimensionally, the two velocity profiles combine to helical streamlines in the capillary. The helical streamlines facilitate the twisting of four semisolid fibers into a continuous microrope.

4.5 Ternary System

The fibers are generated by flowing a liquid mixture composed of butylacrylate (BA), water, methanol, silica nanoparticles and cetyltrimethylammonium bromide (Figure 36) out of four (non-rotating) capillaries, coaxially aligned in the rotating outer capillary. Once the four separate streams enter the water stream, they transform into semisolid fibers

due to BA/water phase separation and gelation of the silica nanoparticles. The progress of phase separation and gelation becomes apparent by the increasing opacity of the fibers as they wind helically around each other.

4.6 Ternary Phase Diagram and Critical Composition Determination

The ternary phase diagram for the mixture of BA, water and methanol is obtained by using turbidimetry test. In this experiment, we measured the weight of each component in the miscible solution of BA and methanol. Water is then added dropwise to the solution until it turns cloudy, and the weight of the water portion is calculated (Figure 36A).

The weight of each component are transformed to volume fractions and plotted in a ternary phase diagram (Figure 36B). The ternary plot of the volume fractions yields a curve known as the binodal curve (blue solid line in Figure 36B). We determined the critical point by approaching the transition from BA-in-water (oil/water) to a water-in-BA (water/oil) emulsions.

We determine this composition by adding the fluorescent dye Nile Red to immiscible ternary mixtures at different points next to the binodal line, Here, we used confocal microscope to identify the emulsion type. Nile red partitions to the oil phase and the fluorescence emission during confocal imaging helps to determine the type of emulsion. The critical point results with $\phi_{BA} = 0.38$, $\phi_{methOH} = 0.44$ and $\phi_{water} = 0.18$.

Figure 36

Ternary Phase Diagram and Critical Composition
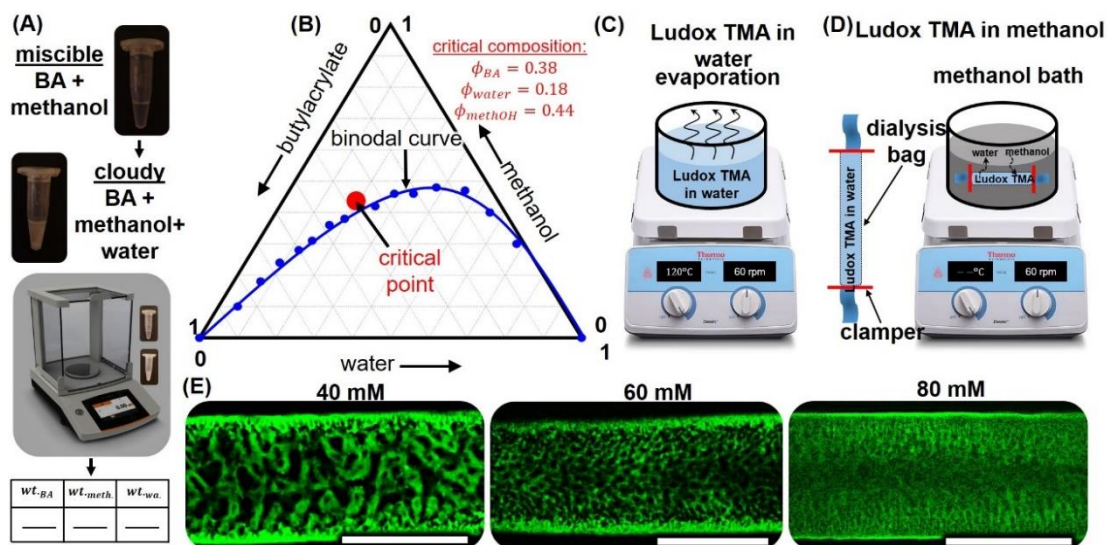
Note. (A) Schematic representation of measuring weight fraction of BA, methanol and water. (B) Ternary phase diagram demonstrating binodal curve and critical point. (C) Schematic demonstration of Ludox TMA preparation in water. (D)   Schematic demonstration of Ludox TMA preparation in methanol. (E) Confocal micrographs pf the bijel fibers with various CTAB concentrations. The black domain represents water phase and the green domain represents the polymerized oil phase, scale bar 0.1 mm.

4.7 Fiber Casting Mixture Preparation

To determine appropriate compositions of the fiber casting mixture, we also add nanoparticles at pH 3 and CTAB in the ternary mixture solution. In general, we prepare Ludox TMA dispersion in two different ways:

4.7.1 Ludox TMA Dispersion in Water

Ludox TMA dispersed in water at pH3 is concentrated from 34 wt.% to (40-50) wt.% by simply evaporating water content (Figure 36C). After centrifuging the concentrate to eliminate any aggregates created during the evaporation process, particle concentration and density are determined.

4.7.2 Ludox TMA Dispersion in Methanol

Ludox TMA dispersed in water at pH 3 is dialyzed for 48 hours in methanol solution to replace water in the dispersion with methanol (Figure 36D). After dialysis the pH, the particle concentration, and density are measured.

Next, the fiber casting mixture is prepared with the obtained particle dispersion upon mixing it with stock solutions of CTAB in methanol, BA and water. In addition, we also add 2-Hydroxy-2-methyl-propiophenone (1 wt. % of BA) as the photo-initiator for polymerization, and Nile red dye for visualization under a confocal microscope. However, we investigated undulation behavior of fibers and ropes without adding photo-initiator and dye to the fiber casting mixture. Example compositions of the fiber casting mixture for three different CTAB concentrations are given in the tabular form in the Appendix C.

4.8 Fiber Extrusion and Structure Optimization

We used a simple coaxially aligned microfluidic device to get bijel fibers. The device is fabricated by coaxially aligning a round-cross-section capillary (ID 50 μm, OD 80 μm) inside a round-cross-section capillary (ID 300 μm and OD 400 μm) by means of a square-cross-section holder capillary (ID 100 μm, OD 200 μm). The generated fibers are polymerized under UV light source and the fibers are washed with ethanol. Then, these

fibers are soaked in DEP oil for refractive index matching and visualized under confocal microscope. The three composition chosen yielded bijel structures (Figure 36E). After analyzing the structure evolution with different CTAB concentration, we selected the composition formed with 60 mM CTAB for further investigation.

4.9 Fiber Casting Mixture with Various Nanoparticle Weight Fractions

The optimized composition obtained by varying CTAB concentration in the fiber casting solution is selected for other experiments. We varied the nanoparticle concentration in the composition and obtained fiber casting mixture with various initial densities (see Appendix D). The final composition of five different fiber casting mixtures with their densities are presented in the tabular form in the Appendix E.

4.10 Microfluidic Twisting and Fiber Assembly

Microfluidic twisting always results in the assembly of the fibers into microropes (Figure 37A). Our previous work has shown how the shear stresses in rotational and axial direction control the tightness of the resulting microropes.[67] However, two distinct behaviors during microrope assembly remain unexplained. When the fiber casting mixture contains a volume fraction below ϕ_{SiO2}= 0.05 silica nanoparticles, the microrope travels for long distances in the center of the rotating capillary (Figure 37B-i). In contrast, when the fiber includes a nanoparticle fraction above $\phi_{SiO2} = 0.07$, the microrope begins to undulate after a few millimeters axial travel length (Figure 37B-ii). What is the reason for this different behavior in dependence of the initial silica nanoparticle volume fraction? To answer this question, we will systematically investigate the fiber properties in the following and begin with a simplified experiment.

Figure 37

Straight and Undulating Microropes
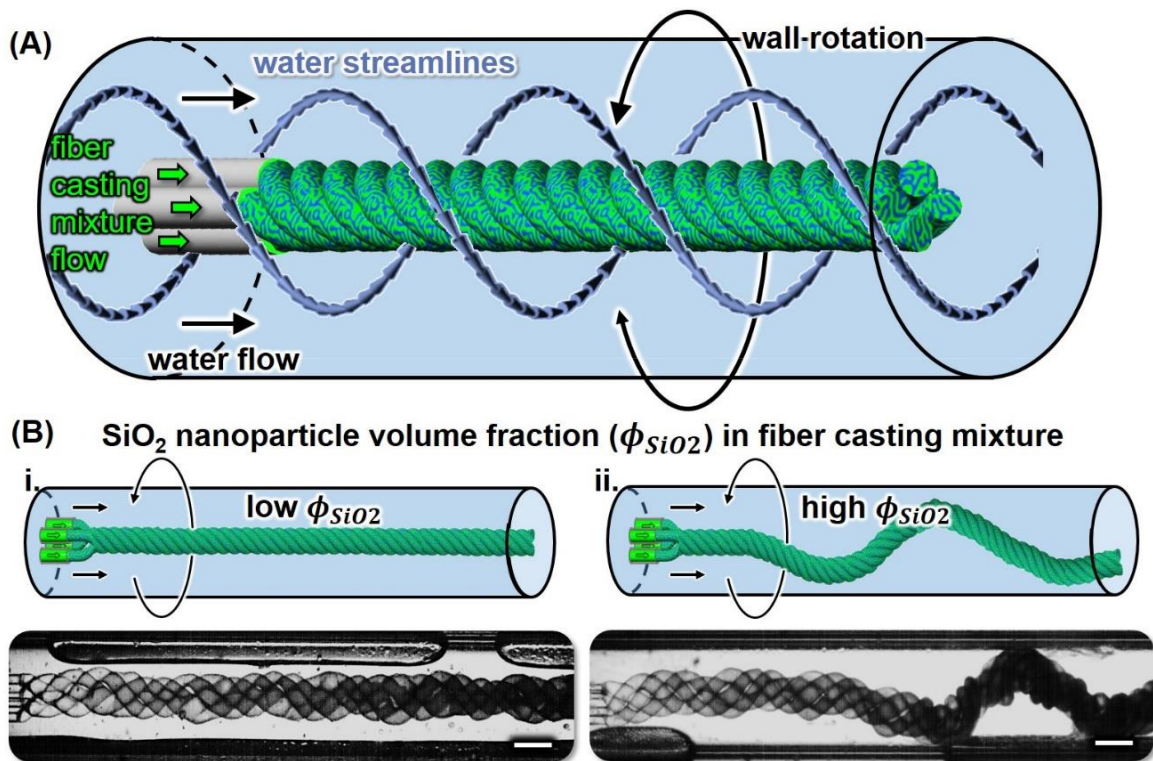
Note. (A) Schematic depicting the generation of a microrope by flowing four fibers into a helical flow field obtained by the superposition of a pump driven axial flow and wall rotation driven drag flow. (B) Schematic and micrographs showing a straight and an undulating microrope at low and high nanoparticle volume fractions ϕ_{SiO_2} in the fiber casting mixture.

4.11 Single Fiber Extrusion

The first clue to explain the behavior can be found when flowing a single fiber into a stagnant reservoir of water. The experiment utilizes a vertically oriented microfluidic

device in which one fiber is flown into a water stream (Figure 38A). The fiber travels along a straight path inside of the microfluidic device due to the shear stresses caused by the co-flowing water.[39] As the fiber enters vertically into the stagnant water reservoir, it coils because of a mismatch between the fiber and the water velocity (Figure 38B&C). More importantly, instead of continuing to travel downwards, the fiber takes a turn and travels upward for several millimeters until it sinks down again (Figure 38C). This behavior shows that the density of the fiber changes along its traveling distance. Initially, buoyancy causes the fiber to rise because the density of the fiber is smaller than the density of the surrounding water. After some traveling length, the fiber density exceeds the water density and gravity pulls it down. This peculiar behavior changes as the initial silica nanoparticle volume fraction in the fibers is increased in steps from $\phi_{SiO2} = 0.051$ to 0.085 (see Appendix 2 and Appendix 3). The higher the initial silica volume fraction, the shorter is the ascending distance of the coiled fiber (Figure 38C). We will analyze next how the density evolution can be quantified for fibers with different ϕ_{SiO2}.

During STrIPS, the solvent (methanol) with a density $\rho_{methOH} = 0.789 \ g/cm^3$ diffuses out of the fiber. In exchange, water with a density $\rho_{water} = 0.998 \ g/cm^3$ diffuses into the fiber. This exchange of a lower density fluid by a higher density fluid results in an increase of the overall density of the fiber over time. The other major components in the fiber including BA ($\rho_{BA} = 0.894 \ g/cm^3$) and silica nanoparticles ($\rho_{SiO2} = 2.2 \ g/cm^3$) remain in the fiber and their volumes do not change over time. With the volume fractions ϕ_i of the respective components, the time dependent composite density of a bijel fiber can be approximated as follows.

Figure 38

Density Change of the Fiber Over Time
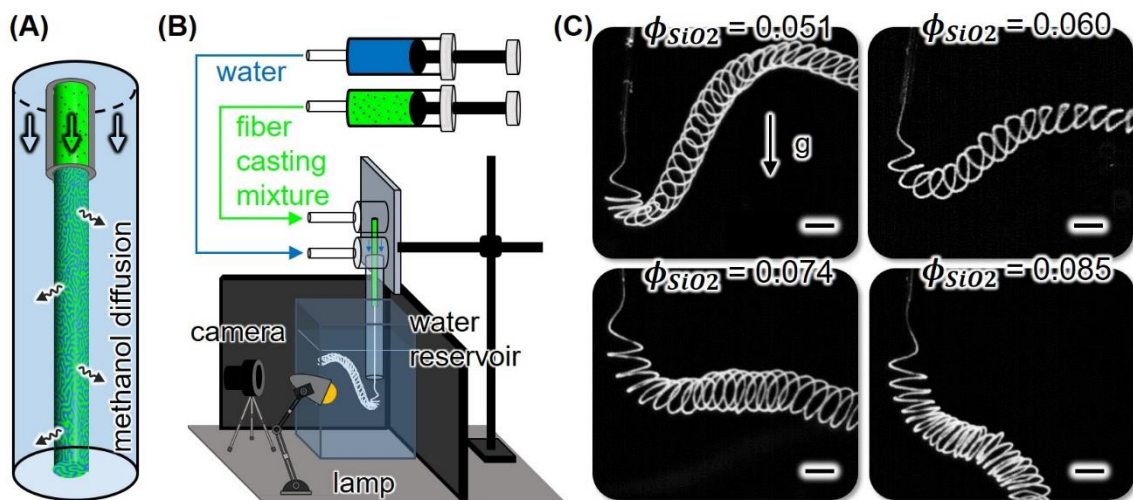
Note. (A) Schematic of bijel fiber extrusion in a device made of coaxially aligned glass capillaries. (B) Schematic of experimental setup to visualize the gravity driven movement of the fiber. (C) Photographs of the moving fiber as it coils in the water reservoir after emerging from the microfluidic device (scale bar 1mm).

4.12 Composite Density of Fiber

During STrIPS, methanol diffusion alters the density of bijel fibers. To estimate the composite density of the fiber during the diffusion process, we consider the following assumptions.

1. The initial volume of the Butyl Acrylate (BA) added to the fiber stays in the fiber. Let $\phi_{BA}(t_0)$ is the volume fraction of BA in the ternary mixture at the beginning. So, $\phi_{BA}(t_0) = \phi_{BA}(t)$.

2. The initial volume of nanoparticles added to the fiber stays in the fiber. Let $\phi_{SiO2}(t_0)$

is the volume fraction of nanoparticles in the ternary mixture at the beginning. So,

$\phi_{SiO2}(t_0) = \phi_{SiO2}(t)$.

3. The initial volume of surfactant ($C_{16}TAB$) added to the fiber stays in the fiber. Let

$\phi_{C_{16}TAB}(t_0)$ is the volume fraction of $C_{16}TAB$ in the ternary mixture at the beginning. So,

$\phi_{C_{16}TAB}(t_0) = \phi_{C_{16}TAB}(t)$.

4. The volume fraction of methanol diffusing out is replaced by water diffusing in the fiber.

(Justification: the overall volume of the fiber remains constant, no change in diameter is

observed). Let $\phi_{methOH}(t_0)$ and $\phi_{water}(t_0)$ are the volume fraction of the solvent and

water phase in the fiber casting mixture at the beginning,

so, $\phi_{methOH}(t_0) + \phi_{water}(t_0) = \phi_{methOH}(t) + \phi_{water}(t)$,

i.e., $\phi_{water}(t) = \phi_{methOH}(t_0) + \phi_{water}(t_0) - \phi_{methOH}(t)$.

Combining the above definitions from 1 to 4 in terms of composite density, the density at

the beginning is

$\rho(t_0) = \rho_{water}\phi_{water}(t_0) + \rho_{methOH}\phi_{methOH}(t_0) + \rho_{BA}\phi_{BA}(t_0) + \rho_{SiO2}\phi_{SiO2}(t_0) +$

$+\rho_{C_{16}TAB}\phi_{C_{16}TAB}(t_0)$.

In addition, the density after time "t" is

$\rho(t) = \rho_{water}\phi_{water}(t) + \rho_{methOH}\phi_{methOH}(t) + \rho_{BA}\phi_{BA}(t) + \rho_{SiO2}\phi_{SiO2}(t) +$

$+\rho_{C_{16}TAB}\phi_{C_{16}TAB}(t)$. Where $\phi_{water}(t) = \phi_{methOH}(t_0) + \phi_{water}(t_0) - \phi_{methOH}(t)$,

and rest of the terms remain constant.

Therefore, composite density of fiber as a function of time can be rearranged as:

$$\rho(t) = \rho_{water}\{\phi_{methOH}(t_0) + \phi_{water}(t_0) - \phi_{methOH}(t)\} + \rho_{methOH}\phi_{methOH}(t) +$$

$$\rho_{BA}\phi_{BA}(t_0) + \rho_{SiO2}\phi_{SiO2}(t_0) + +\rho_{C_{16}TAB}\phi_{C_{16}TAB}(t_0).$$

All the terms in the equation can be measured experimentally except the volume fraction of methanol over time.

4.13 Density Evolution Over Time – COMSOL Simulation

To obtain methanol concentration over time in the bijel fiber, we developed a simple model in COMSOL Multiphysics software. In this model, Fick's second law of diffusion is used to relate the change in concentration gradient of methanol over time through the following differential equation: $\frac{\partial C_{methOH}}{\partial t} = D_{methOH}\frac{\partial^2 C_{methOH}}{\partial r^2}$, where D_{methOH} is the diffusion coefficient. Here, we created a cylindrical geometry of 100 um diameter to describe the fiber during extrusion in a water channel of diameter 800 μm (Figure 39A). At the beginning, the methanol concentration in the inner cylinder can be calculated by using the following formula:

$$C(t_0) = \frac{\phi_{methOH}(t_0)\cdot\rho_{methOH}}{M_{methOH}} = \frac{0.44\times\frac{790kg}{m^3}}{\frac{0.032kg}{mol}} = 10849\frac{mol}{m^3}.$$ However, the outer cylinder is

filled with the water with net methanol concentration of $0\frac{mol}{m^3}$ (Figure 39B). Here, we further consider the following assumptions to study the transient diffusion model:

(i) Concentration dependent diffusion coefficients: The concentration dependence of the diffusion coefficient D_{methOH} for methanol in water can be found in the literature.[90] For the diffusion simulation, D_{methOH} is calculated using linear interpolation algorithms between data points (Figure 39C) to solve the following diffusion equation:

$$\frac{\partial c_{methOH}}{\partial t} = D_{methOH} \left(c_{methOH}\right) \frac{\partial^2 c_{methOH}}{\partial r^2}.$$

Figure 39

Solvent Concentration Over Time
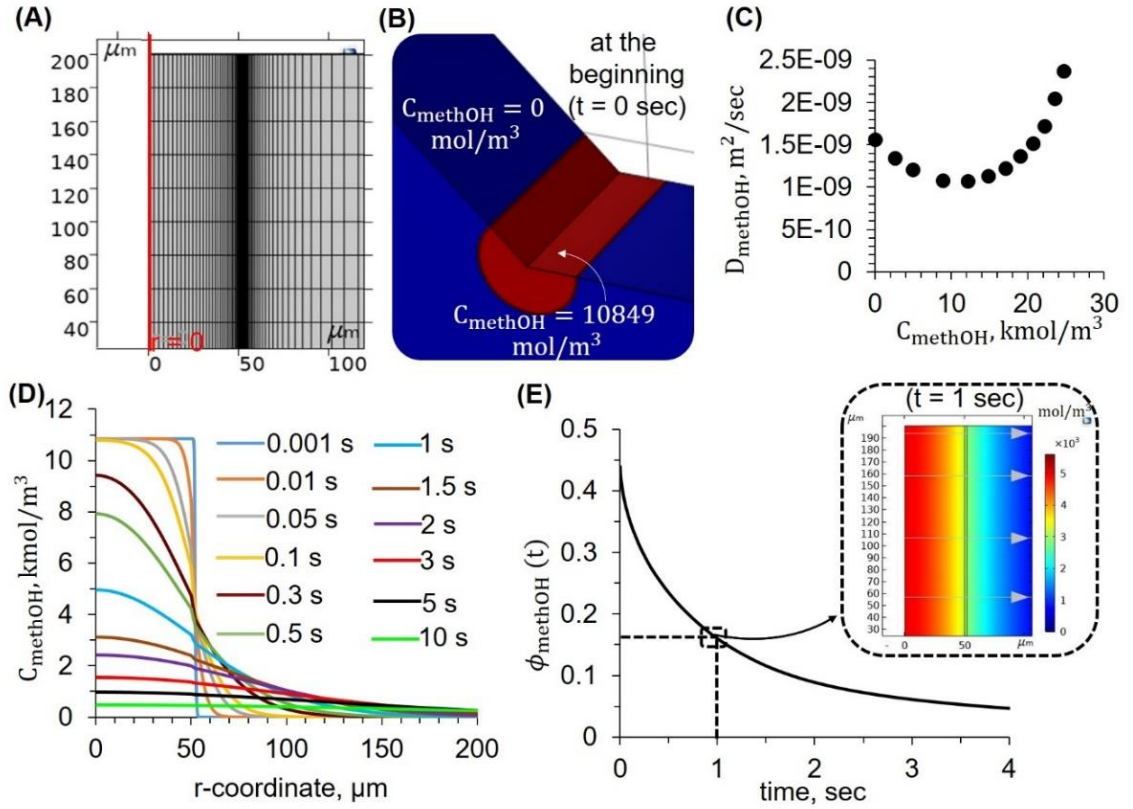
(ii) A thin diffusion barrier on the surface of the fiber to model the smaller bijel surface pores: The bijel fiber surface is normally covered with silica particles reducing porosity for the molecular diffusion. To account for this in the model, we assume over a thickness of 2 μm below the fiber surface a diffusion coefficient of $D_{methOH} \left(c_{methOH}\right)/3$.

Note. (A) Mesh representing nodes for the numerical calculation of the concentrations used in the simulation. (B) Cutaway 3D drawing of the fiber segment at the beginning of the simulation (t = 0). (C) Diffusion coefficient for methanol in water dependence of the methanol concentration. (D) Radial concentration profile of methanol at different time intervals. (E) Methanol volume fraction (ϕ_{methOH}) over time computed by integrating the local concentration in 3D space in the fiber geometry. The inset is a 2D sample plot of the methanol concentration at time t = 1 sec.

In addition, the concentration gradients along the radial directions at different time intervals are studied. We observed that within 1 second of the diffusion process more than half of the methanol diffuses out from the fiber into the water phase (Figure 39D). We used the local concentration of methanol in the radial direction to determine the volume fraction of the methanol in the fiber over time by performing the following integration:

$$\phi_{methOH}(t) = \frac{\int_0^L \int_0^{2\pi} \int_0^R \phi_{methOH}(r,t)\cdot r dr\cdot d\theta\cdot dz}{\int_0^L \int_0^{2\pi} \int_0^R r dr\cdot d\theta\cdot dz} = \frac{M_{methOH}}{\rho_{methOH}} \frac{\int_0^{2\pi} \int_0^R C_{methOH}(r,t) r dr d\theta}{\pi R^2}, \text{ with}$$

$\phi_{methOH}(r,t)$ the local volume fraction, r the radial coordinate, θ the angular coordinate, z the axial coordinate, R the outer radius of the fiber, L the length of the analyzed fiber segment, and $C_{methOH}(r,t)$ the local methanol concentration. Here, we performed the integration in COMSOL and the obtained result $\varphi_{methOH}(t)$ is plotted against the time in Figure 39E.

Snapshots from the simulation visualizing the time dependent methanol concentration are shown in Figure 40A. We assume that the volume of methanol diffusing out of the fiber is fully replaced by water diffusing in, since microscopy shows that the

volume (diameter) of the fiber stays constant along its travelling distance. This gives the

expression $\phi_{water}(t_0) + \phi_{methOH}(t_0) = \phi_{water}(t) + \phi_{methOH}(t)$, enabling the

calculation of $\rho(t)$ with the simulation result for $\phi_{methOH}(t)$. Figure 40B plots the

calculated density evolution for different ϕ_{SiO2}. For fibers with ϕ_{SiO2} = 0.043, 0.051,

0.060, 0.074 and 0.085 the initial densities calculate to $\rho(t_0)$ = 0.911 g/cm³, 0.923 g/cm³,

0.936 g/cm³, 0.952 g/cm³, and 0.966 g/cm³, respectively.

Figure 40

Density Estimation of Fibers Over Time
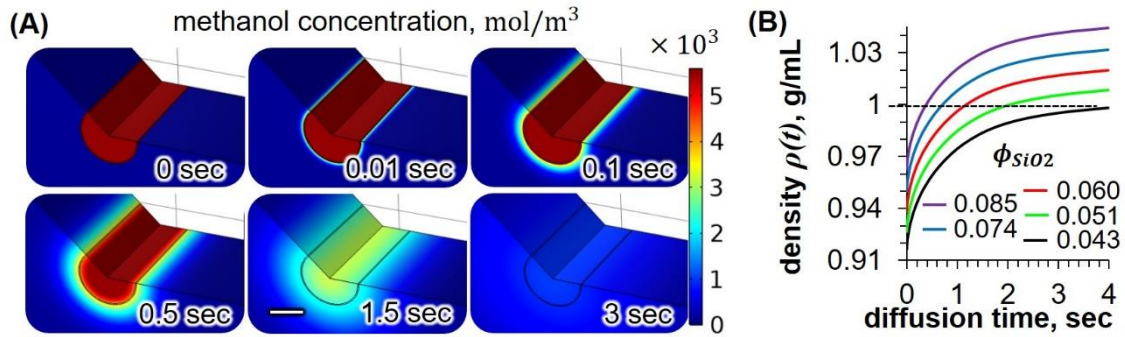
Note. (A) 3D color plot and color legend showing the simulation result of the methanol

concentration in and around the fiber over time scale bar 50 μm. (B) Calculated density

evolutions of fibers with various initial silica volume fractions.

The simulation shows that the densities of the fibers increase asymptotically with

time. Moreover, the simulation predicts that it takes shorter times for $\rho(t)$ to reach

$\rho_{water} = 0.998 g/cm^3$ when ϕ_{SiO2} increases (dashed horizontal line in Figure 40B). This

trend agrees with the shorter times of the buoyancy driven fiber ascend with increasing

ϕ_{SiO2} (Figure 38C). With this quantitative understanding, we can now analyze the effect

of $\rho(t)$ on a single fiber during microfluidic twisting.

Figure 41

COMSOL Simulation Combining Diffusion and Convection
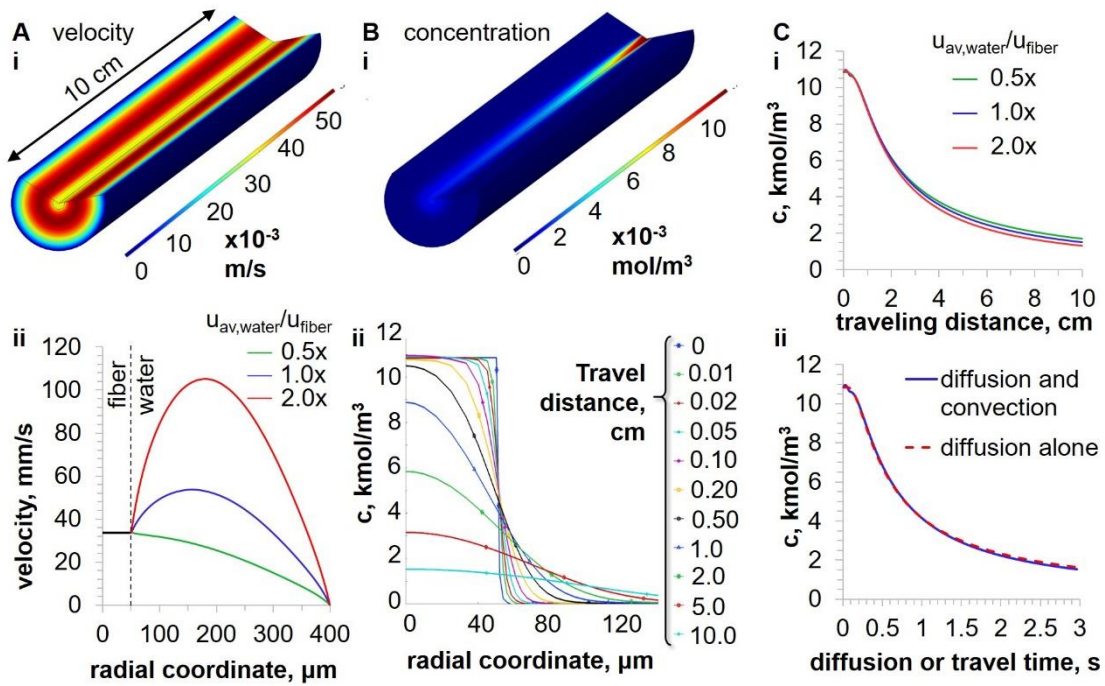
Note. (A-i) 3D velocity plot in a channel with 800 μm diameter with a fiber of 100 μm

diameter. (A-ii) Radial velocity profiles for different average water velocities $u_{av,water}$ at

constant fiber velocity u_{fiber}. (B-i) 3D concentration plot of methanol. (B-ii) Radial

concentration of methanol for different fiber travelling distances (both B-i and B-ii for

$\frac{u_{av,water}}{u_{fiber}} = 1$). (C-i) Methanol concertation in center of fiber against travel distance for

different $\frac{u_{av,water}}{u_{fiber}}$. (C-ii) Methanol concentration in center of fiber for different travel times $(t = L/u_{fiber})$. The red dashed curve shows the center methanol concentration from the diffusion simulation in Figure S6 without convection.

To show that in our experiments radial diffusion dominates over axial dispersion, we develop a steady state COMSOL simulation combining the transport of diluted species and the laminar flow modules. A 10 cm long cylindrical channel of 800 μm diameter contains a cylindrical fiber of 100 μm diameter. The fiber moves via plug flow through the center of the channel at a volumetric flow rate Q_1, while water flows around the fiber at a volumetric flow Q_2. Figure 41A-i shows a 3D surface plot of the velocity distribution. In the simulation we vary the water velocity around the fiber to probe the effect of convection on the diffusion process of methanol. Figure 41A-ii shows the three different water velocity profiles around the fiber, given as multitudes of the fiber velocity.

The fiber enters the flow region with a methanol concentration of 10849 mol/m^3. The methanol has a constant diffusion coefficient of $1.3*10^{-9}$ m^2/s both in the fiber and in the surrounding water. Figure 41B-i shows the 3D surface plot of the methanol concentration for $\frac{u_{av,water}}{u_{fiber}} = 1$. The methanol concentration gradually decreases along the axial travel length of the fiber due to diffusion into the surrounding water. Figure 41B-ii shows the corresponding radial methanol concentration profiles at different travel distances of the fiber.

In Figure 41C-i the methanol concentration in the center of the fiber is plotted against the travel distance for the three different water velocities. The graph shows that the

velocity of water around the fiber has an insignificant effect on the concentration evolution.

We can convert fiber travel distance L into fiber travel time t by dividing L by the fiber velocity u_{fiber} (0.0337 m/s). With the fiber travel time t, we can compare the simulation considering convection to the simulation based on pure diffusion (Figure 39). Figure 41C-ii shows the methanol concentration in the center of the fiber with convection ($\frac{u_{av,water}}{u_{fiber}} = 1$, fiber travel time) and without convection (diffusion time) plotted against the time. The two curves are practically identical, confirming that radial diffusion dominates the methanol transport in comparison to axial dispersion.

4.14 Single Helical Fiber Extrusion

Figure 42

Microfluidic Twisting of Single Fibers
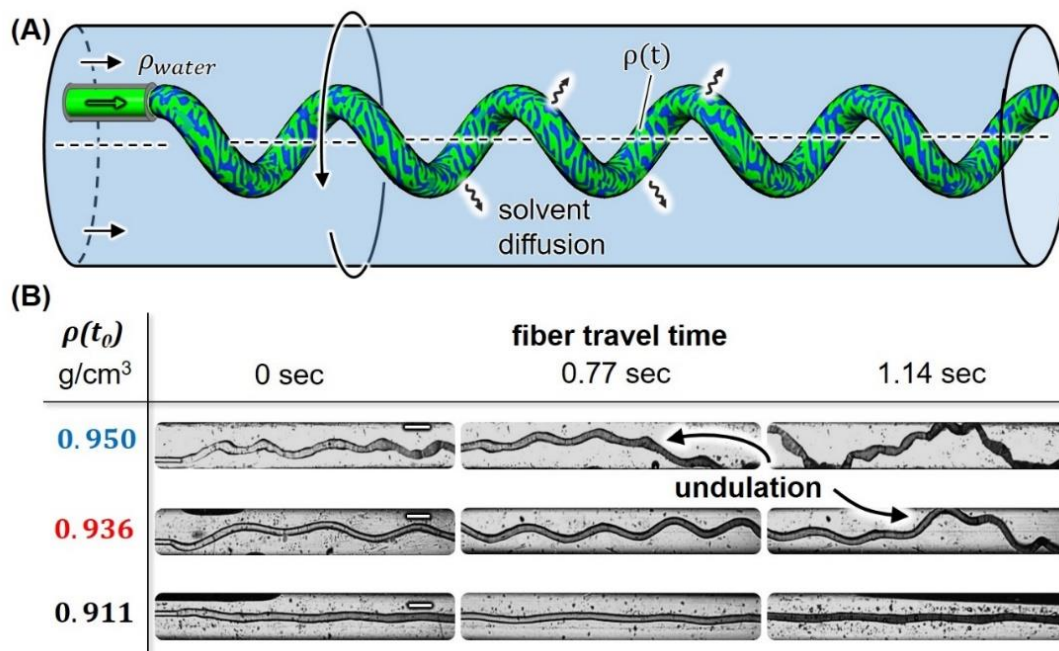
Note. (A) Schematic of a microfluidic device to flow a single helical fiber into a rotating channel. (B) Micrographs of helical bijel fibers with variable initial densities flowing

through the rotating channel at different axial travelling distances (given as fiber travelling times), scale bar 0.5 mm.

Figure 42A shows a schematic of flowing a fiber into a rotating capillary with water co-flowing from left to right. Regardless of the radial position of the extrusion nozzle, the helical fiber moves initially towards the center of the rotating channel. However, after characteristic travel distances, the fiber begins to undulate. We convert travel distance to travel time based on the measurement of the fiber speed as described next.

4.15 Travel Time Estimation until Undulation

Figure 43

Travel Time Estimation
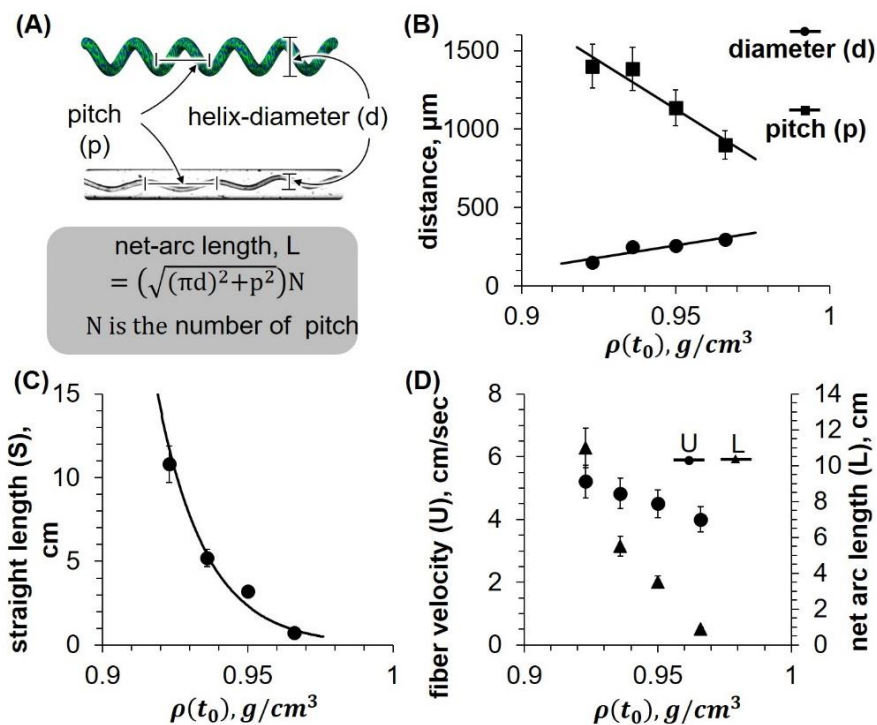
Note. (A) A picture demonstrating how we estimated the helical diameter (d) and pitch length (p) of the twisted bijel fiber (top), and formula that was used to estimate the net arc

81

length (bottom). (B) A graph demonstrating variation of d and p with respect to $\rho(t_0)$. (C) Experimentally measured straight length of the helical fiber until undulation against $\rho(t_0)$. (D) Fiber velocity and net arc length against $\rho(t_0)$. The net arc length (L) and fiber velocity (U) were used to estimate the net travel time before undulation.

We measured the straight travel distance of the helical fibers until the undulation begins. As depicted in Figure 43A the straight travel distance of the helical fibers can be converted into an arc length measuring the diameter (d) and pitch length (p) via the equation: net arc length (L) $= \sqrt{((\pi d)^2 + p^2)}\, N$, where N is the number of pitch. The total number of pitch (N) can be estimated by dividing the straight travel length (S) by the pitch length (p). The variation of the helical diameter (d), pitch length (p) against the various initial density of the ternary mixture is shown in the Figure 43B.

Experimentally measured straight travel distance (S) of the fiber before undulation against $\rho(t_0)$ is plotted in the Figure 43C. In addition, we estimated the velocity of the fiber by measuring the travel distance and corresponding time by tracking the irregularities on the fiber surface.

The fiber velocity (U) and estimated net arc length (L) with respect to the initial density of the ternary mixture are plotted in the Figure 43D. The net arc length (L) is divided by the fiber velocity (U) to estimate the travel time until undulation begins.

The micrograph table in Figure 41B shows that the travel time for a fiber (100µm diameter) to undulate depends on $\rho(t_0)$. Fibers with $\rho(t_0) = 0.950 g/cm^3$ and $\rho(t_0) = 0.936 g/cm^3$ undulate after 0.23 sec and 1.14 sec, respectively. In contrast, the fiber with

$\rho(t_0) = 0.911 g/cm^3$ stays in the channel center and does not undulate over the entire

length of the capillary (10 cm).

4.16 Travel Time Comparison

Figure 44

Travel Time Comparison
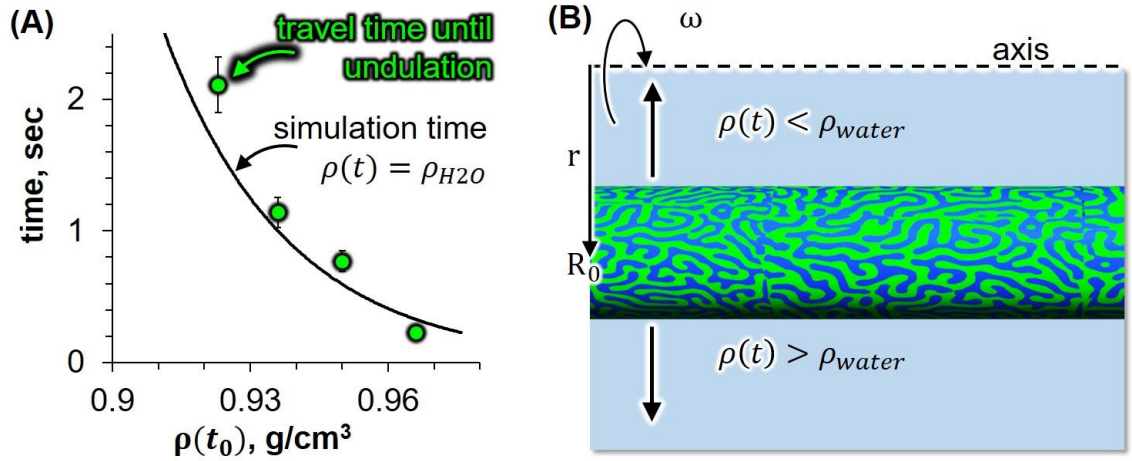
Note. (A) Plot of the experimentally determined fiber travel time until undulation starts in

dependence of the initial density of the fiber (green points). Error bars correspond to the

standard deviation of 5 measurements. For comparison, the solid curve represents the time

for the fiber density to reach the density of the surrounding water (from simulation). (B)

Schematic drawing depicting the direction of centrifugal force for different fiber densities.

We now compare the experimental travel time of the fiber before undulation starts with the calculated time for $\rho(t)$ to reach ρ_{water}. Figure 44A shows that the two times agree reasonably well, strongly suggesting that crossing the density of water triggers the undulation of the fiber in the channel. This can be understood by considering that the sign of the centrifugal force changes as the density difference $\rho_{water} - \rho(t)$ becomes negative. The centrifugal force F_c per volume V of fiber calculates to $F_c/V = (\rho_{water} - \rho(t))\omega^2 R_0$ with R_0 the radial distance from the rotational axis, and ω the angular velocity (Figure 44B).[26] When F_c/V is positive, the fiber is pulled towards the center of the channel. On the other hand, when F_c/V becomes negative, the fiber is pulled radially outwards and collides with the channel wall. Thus, the comparison of simulation with experiment explains that the fiber undulation in Figure 42B results from the change of the direction of the centrifugal force since the fiber density $\rho(t)$ exceeds the water density ρ_{water}. Moreover, the formula for F_C/V also explains why the helical radius of the fibers in Figure 42B depends on $\rho(t_0)$. For $\rho(t_0) = 0.911$ the value of $(\rho_{water} - \rho(t))$ is larger than for $\rho(t_0) = 0.936$. The helical radius is smaller, because the fiber is pulled more strongly towards the center.

4.17 Centrifugal Force Effect on Bijel Ropes

Figure 45

Undulation of Microropes with Variable Initial Densities of the Fibers at Constant Density of the Coflowing Water Phase
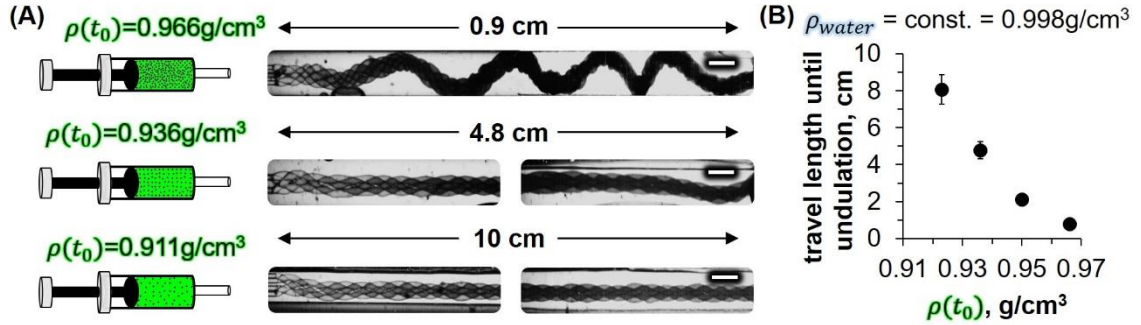
Note. (A) Schematics of the syringes containing the fiber casting fluids with different volume fractions of silica nanoparticles, micrographs showing the corresponding microropes formed during microfluidic twisting. (B) Plot of the travel time until undulation starts against the initial fiber density $\rho(t_0)$. All experiments are performed at the same pressure for the fiber casting fluid ($Q_T = 400\ kPa$), flow rate for the water phase ($Q_W = 1\ mL/min$) and rotational speed of the wall ($rpm = 3000$).

Does the centrifugal force have the same influence when multiple fibers are twisted? In the following, four fibers undergo microfluidic twisting, first with a variable initial fiber density $\rho(t_0)$, then with a variable density of the co-flowing water. Figure 45A shows micrographs of microropes generated with three different fiber casting fluids of variable $\rho(t_0)$ (realized by changing ϕ_{SiO2}). The microrope made of the heaviest fibers

with $\rho(t_0) = 0.966g/cm^3$ undulates immediately, while the microrope with $\rho(t_0) = 0.936g/cm^3$ travels for 4.8 cm before undulation starts. In contrast, for a microrope with $\rho(t_0) = 0.911g/cm^3$ no undulation is observed over a travel distance of 10 cm. The trend is plotted on the Figure 45B and supports the centrifugal effect as the driving force for undulation. The microropes with various water flow rates are shown in the Figure 46.

Next, we show that increasing the density of the co-flowing water (ρ_{water}) also enables longer microrope traveling distances before undulation begins. This can be explained by considering that for larger values of ρ_{water} the density difference $\rho_{water} - \rho(t)$ stays positive for longer times during the increase of the fiber density $\rho(t)$. To elevate ρ_{water} above 0.998 g/cm³, we add variable volume fractions of silica nanoparticles (Ludox TMA) to the co-flowing water.

Figure 47A shows snapshots of microropes travelling through the rotating channel for values of ρ_{water} ranging from 1.03 g/cm³ to 1.07 g/cm³ for a constant initial fiber density of $\rho(t_0) = 0.966g/cm^3$. A microrope formed with this high value of $\rho(t_0)$ starts to undulate immediately in pure water of 0.998 g/cm³ (Figure 45A). However, with coflowing water of $\rho_{water} = 1.03g/cm^3$, the microrope travels for 2.5 cm until undulation starts (Figure 47 B). Moreover, when ρ_{water} is raised to $1.07cm^3$, the fiber remains in the center of the channel along the entire length (10 cm). The density calculation in Figure 40B shows that $\rho(t)$ never reaches $1.07cm^3$, thus $\rho_{water} - \rho(t)$ will remain positive permanently and the direction of the centrifugal force always keeps the microrope in the center of the channel.

Figure 46

Ropes with Various Water Flow Rates

(A) i. $\rho(t_0) = 0.911$ g/mL 1.0 ml/min **ii.** $\rho(t_0) = 0.923$ g/mL 1.1 ml/min **iii.** $\rho(t_0) = 0.936$ g/mL 1.2 ml/min

0.9 ml/min 1.0 ml/min 1.1 ml/min
0.8 ml/min 0.9 ml/min 1.0 ml/min
0.7 ml/min 0.8 ml/min 0.9 ml/min
0.6 ml/min 0.7 ml/min 0.8 ml/min

iv. $\rho(t_0) = 0.950$ g/mL 1.3 ml/min **v.** $\rho(t_0) = 0.966$ g/mL 1.4 ml/min

1.2 ml/min 1.3 ml/min
1.1 ml/min 1.2 ml/min
1.0 ml/min 1.1 ml/min
0.9 ml/min 1.0 ml/min

0.5 mm

(B) 270

diameter, μm

$Q_{water} = 1 \dfrac{mL}{min}$

0.9 0.95 1

$\rho(t_0), g/cm^3$
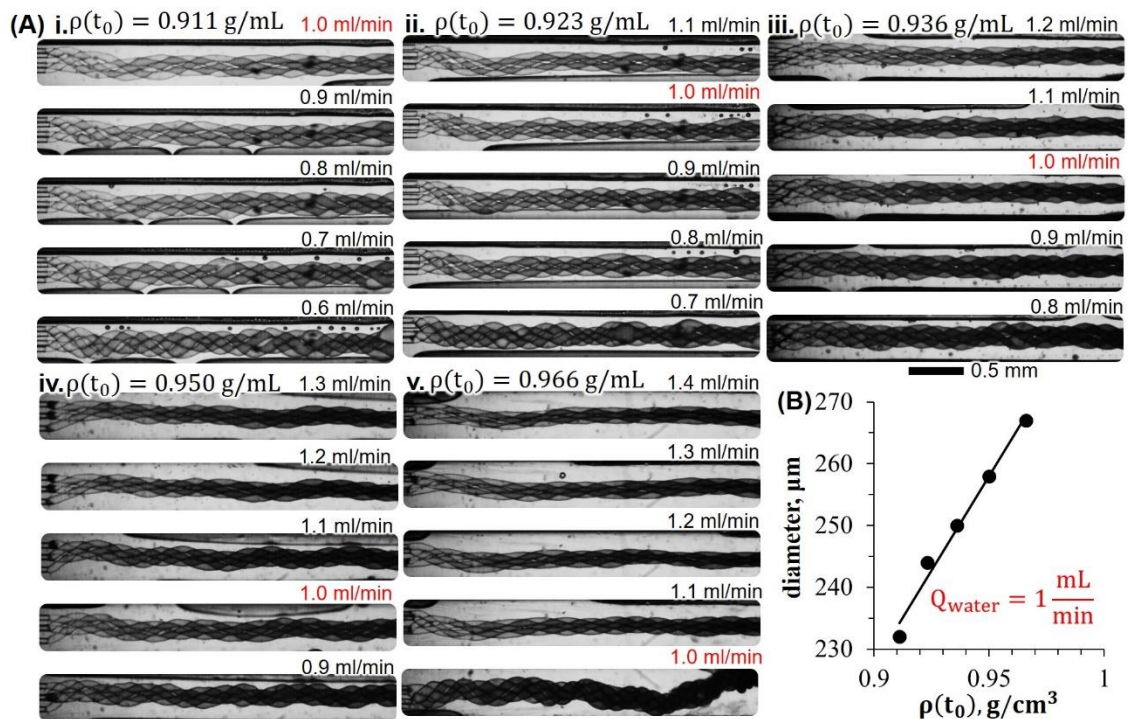
Note. (A) Micrographs representing the beginning segment of the bijel rope at different flow rate of the water phase: (i) $\rho(t_0) = 0.911 \ g/cm^3$ (ii) $\rho(t_0) = 0.923 \ g/cm^3$ (iii) $\rho(t_0) = 0.936 \ g/cm^3$ (iv) $\rho(t_0) = 0.952 \ g/cm^3$ (v) $\rho(t_0) = 0.966 \ g/cm^3$. (B) A graph-representing diameter of the rope against $\rho(t_0)$ at constant flow rate of the water phase.

Increasing ρ_{water} also allows the formation of microropes with oil phases of higher densities. In all prior experiments butylacrylate (BA) was used as the oil with a comparably low density of $0.894 \ g/cm^3$. The oil ethylene glycol dimethacrylate (EDMA) has a density

of $1.051 \ g/cm^3$, resulting in a fiber casting fluid density of $\rho(t_0) = 0.977 g/cm^3$. In a

water phase of $\rho_{water} = 0.998 g/cm^3$ a microrope made with EDMA undulates promptly.

In contrast, the microrope remains perfectly centered in the channel with a continuous

phase of $\rho_{water} = 1.05 g/cm^3$ (Figure 47C).

Figure 47

Undulation of Ropes with Various Density of the Continuous Phase
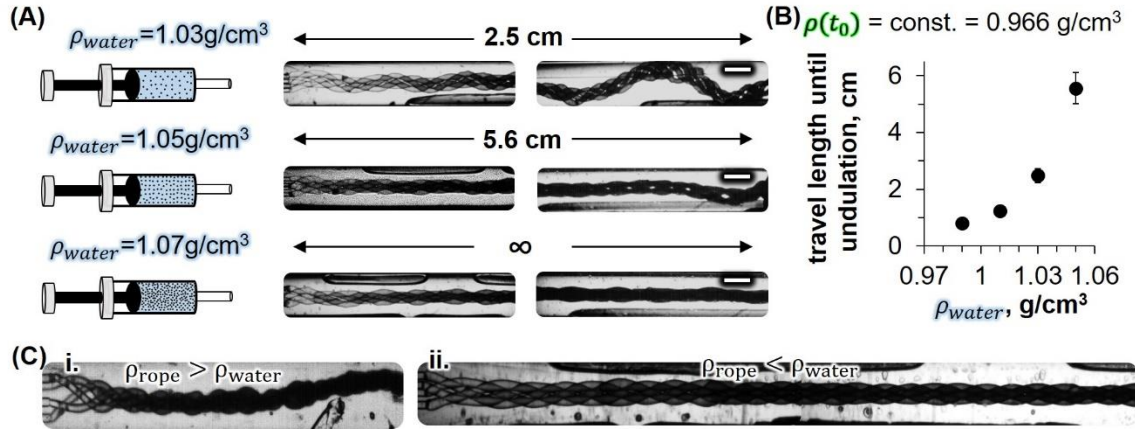
Note. (A) Schematics of the syringes containing the water phase with variable amounts of

added silica nanoparticles, micrographs showing the corresponding microropes (B) Plot of

the travel time until undulation against the water phase density ρ_{water}. (C) (i) Undulating

rope with the fiber casting solution composed of EDMA, water and methanol at $\rho(t_0) =$

$0.977 \ g/cm^3$ and $\rho_{water} = 0.998 \ g/cm^3$. (ii) Straight rope without undulation with the

same ternary mixture $(\rho(t_0) = 0.977 \ g/cm^3)$ but at the increased density of the water

phase $(\rho_{water} = 1.05 \ g/cm^3)$. All experiments are performed at the same pressure for the

fiber casting fluid ($Q_T = 400\ kPa$), flow rate for the water phase ($Q_W = 1\ mL/min$) and rotational speed of the wall ($rpm = 3000$).

These findings confirm that the direction of the centrifugal force on the microropes determines whether or not undulation occurs. To continuously generate infinitely long straight microropes, the density of the fibers ($\rho(t)$) must be smaller than the density of the surrounding water (ρ_{water}).

4.18 Conclusions

In conclusion, the centrifugal effect on microropes generated by microfluidic twisting has been analyzed. The direction of the centrifugal force determines whether microropes undergo destructive wall collisions during microfluidic twisting. Due to a changing density of the microropes over time, they become heavier than the co-flowing water, causing the centrifugal force to pull them towards the rotating wall of the microfluidic twisting device. This can be avoided by decreasing the density of the fiber casting mixture, or upon increasing the density of the co-flowing water, enabling a controlled and continuous collection of uniform microropes (Chapter 5). We envision microfluidic twisting to enable the fabrication of new composite materials with applications in flexible electronics,[91] micro robotics,[92] actuators [93], and tissue engineering.[94] Furthermore, the knowledge gained from this work will facilitate future studies of microfiber twisting, as well as the assembly of particles, emulsion droplets or biological cells via microfluidic twisting.

Chapter 5

High-Tensile, Strength Composite Bijels and Derived Materials

Some of the text and figures are reproduced and adapted with permission from the journal, Kharal, S.P., Hesketh, R.P., and Haase, M.F., "High-tensile strength, composite bijels through microfluidic twisting", Advanced Functional Materials, 30, 2003555, 2020, reference [67].

5.1 Introduction

Multifunctional micro-fibers have piqued curiosity for decades due to their outstanding characteristics of large surface area, different mechanical properties, diversified topologies, and flexibility to be folded, braided, or twisted into 3D composites.[95][96][87] Twisting numerous fibers into higher order helices or ropes combines the properties of the individual fibers and presents a versatile reinforcement approach with a wide range of applications.[97] The primary importance of higher order helices is based on space-saving configurations, bending flexibility, and the formation of composite materials by incorporating materials with varying physical and chemical properties. In previous chapters, The microfluidic twisting method of bijel fibers into a rope by manipulating translation shear stress, rotation shear stress, and centrifugal force density has been discussed. In this chapter 5, we introduce a mechanism for collecting infinitely long straight microropes and investigate tensile strength of a composite bijels. Additionally, the bijel ropes are transformed into stimuli-responsive composite hydrogel ropes.

5.2 Materials

Ludox TMA suspensions, CTAB (Bio Ultra > 99%), Diethyl phthalate (DEP),

tertiary Butyl Acrylate (t-BA), and Ethylene glycol dimethacrylate (EDMA) were

purchased from Sigma-Aldrich and used as received. Pure Water and pure methanol

(200% proof > 99: 5%) were used for all experiments.

5.3 Preparation of Suspension Solution

The ternary liquid mixture comprises 6 components: (i) pure methanol (ii) a

solution of 200 mM CTAB in ethanol (iii) Ludox TMA at pH 3 (iv) Ludox TMA particles

in methanol at pH 3 (v) pure water and (vi) one of the oil component in each mixture (DEP,

EDMA, t-BA)

5.4 Rotating System Made of Metals

We used a Lego-based rotating system to twist bijel fibers, which were then

visualized under a microscope equipped with a high-speed camera. To transfer the bijel

ropes from the continuously rotating micro-capillary to the external collection vial, we

devised a rotating system comprised of various metallic parts.

The majority of the metallic parts were purchased from McMaster and used exactly

as received. The metallic tunnel and base plate for the microfluidic system, on the other

hand, were designed in AutoCAD and fabricated in the machine shop. Figure 48 depicts

the metallic base plate and tunnel in 2D and Figure 49 depicts the 3D view. Figure 50

shows the different metallic parts as well as the assembled product.

In order to reduce the potential impacts on ropes from the rotating channel wall the

distance between extrusion nozzles and collection vial should be minimized. To realize this

in the new rotating system made of metals, previous microfluidic system is modified. In the previous design, a round tube treated with tridecafluoro-2-(tridecafluorohexyl) decyl trichlorosilane is rotated with the help of PDMS mounting. This means the square tube holding PDMS is fixed in a glass slide and the inserted round tube rotates (Figure 18).

Figure 48

Autocad Drawing of Metallic Base Plate with Dimensions
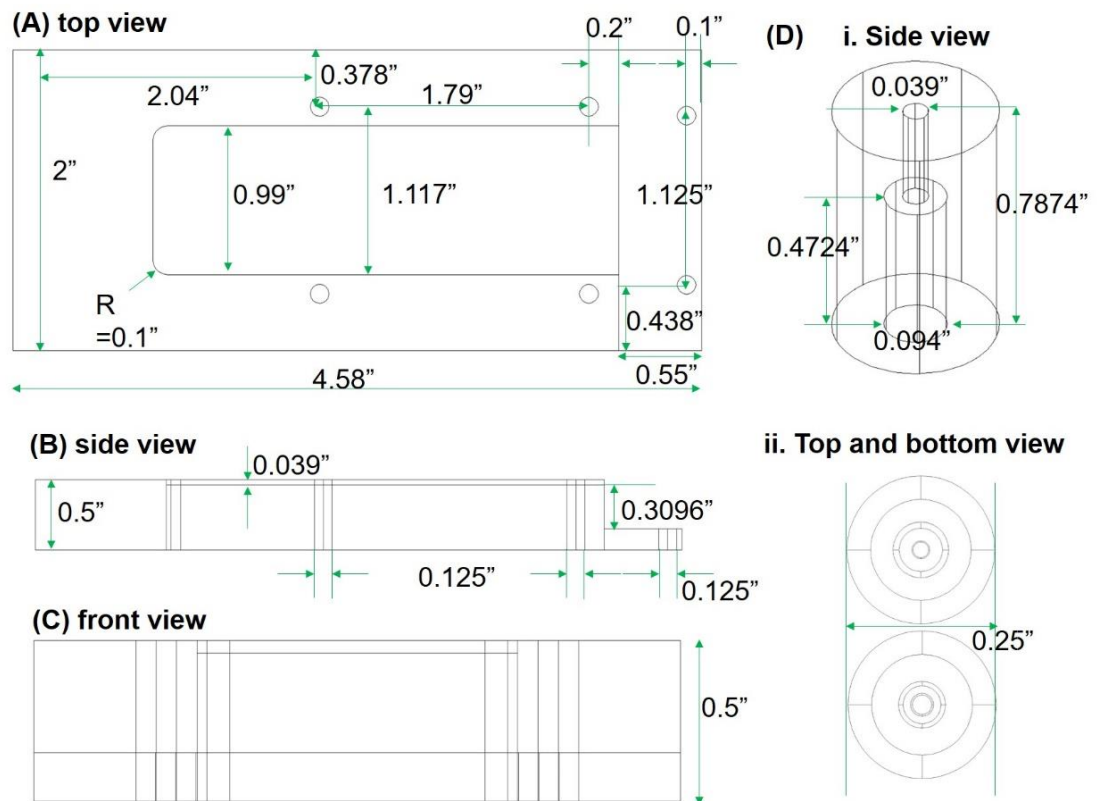
Note. (A) Top view. (B) Side view. (C) Front view. (E) AutoCAD drawing of a metallic tunnel with its dimensions: (i) Side view (ii) Top and bottom view.

Figure 49

Autocad Drawing 3D View
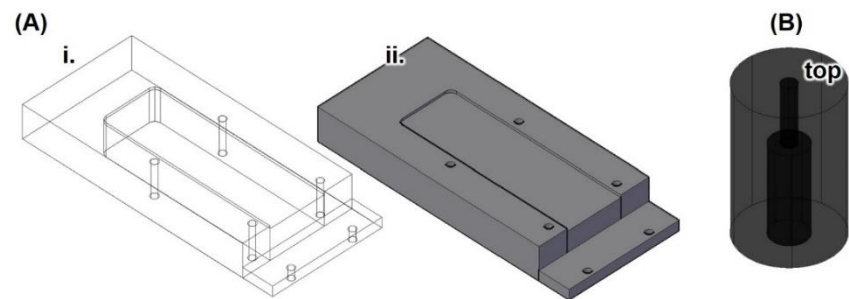
Note. AutoCAD drawing of metallic base plate (A) and the metallic tunnel in 3D view (B).

Figure 50

Figures Depicting Metallic Parts Needed to Build a Rotating System
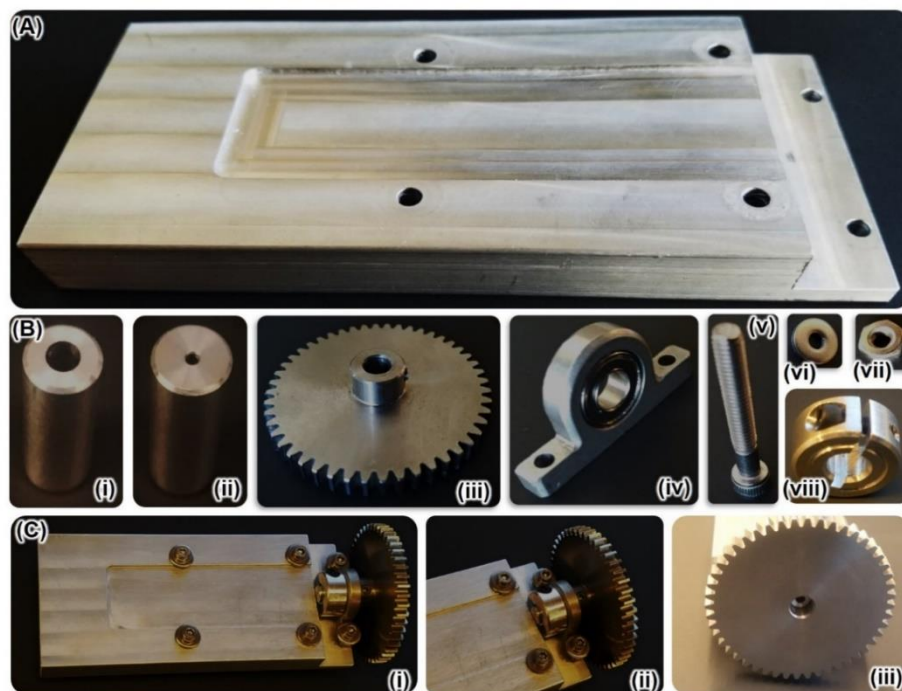
Note. (A) The custom made metallic base plate. (B) Custom made metallic tunnel with its bottom view (i) and top view (ii). (C) Metallic parts ordered from McMaster [(i) Metallic gear (ii) Low profile mounted shielded steel ball Bearing (iii) Socket head screw (iv) Washer (v) Screw nuts (vi) Clamping shaft collar]. (D) Metallic rotating system after assembling all parts at appropriate positions. (i) top view (ii) A picture representing a gear segment. (iii) Front view.

In the modified design, however, the situation is reversed. The distance between the extrusion nozzles and collection vial can be shortened significantly by keeping the round tube fixed and the square tube containing PDMS spinning. For the device manufacturing, a detailed explanation has already been provided in Chapter 3. However, the next section discusses how we coupled the glass capillaries together in the modified microfluidic design.

Figure 51A(i) and Figure 51B(i) show two different fluorocarbon-treated round-cross-section capillary with similar OD of 1 mm but dissimilar ID of 0.45 mm and 0.55 mm respectively. Each round tubes are inserted in a normal (untreated) square-cross-section capillary of ID 1.05 mm and OD of 1.40 mm (Figure 51A(ii) and Figure 51B(ii)), as shown in the Figure 51A(iii) and Figure 51B(iii). Polydimethylsiloxane (PDMS) is next introduced in the region not occupied by the round and square capillaries Figure 51A(iv) Figure 51B(iv). The PDMS is cured for 20 minutes at 150 °C. Inside the PDMS bearing, the fluorocarbon-treated capillary can freely revolve on its axis. The extrusion capillary combinations are made as described in chapter 3. Here, we can use two capillary combinations as shown in the Figure 51A(v-vii) and Figure 51B(v-vii). The capillary

combinations are then inserted into the capillary combinations designed in Figure 51A(iv) and Figure 51B(iv).

Figure 51

Step-By-Step Illustrations for Making A Microfluidic Device
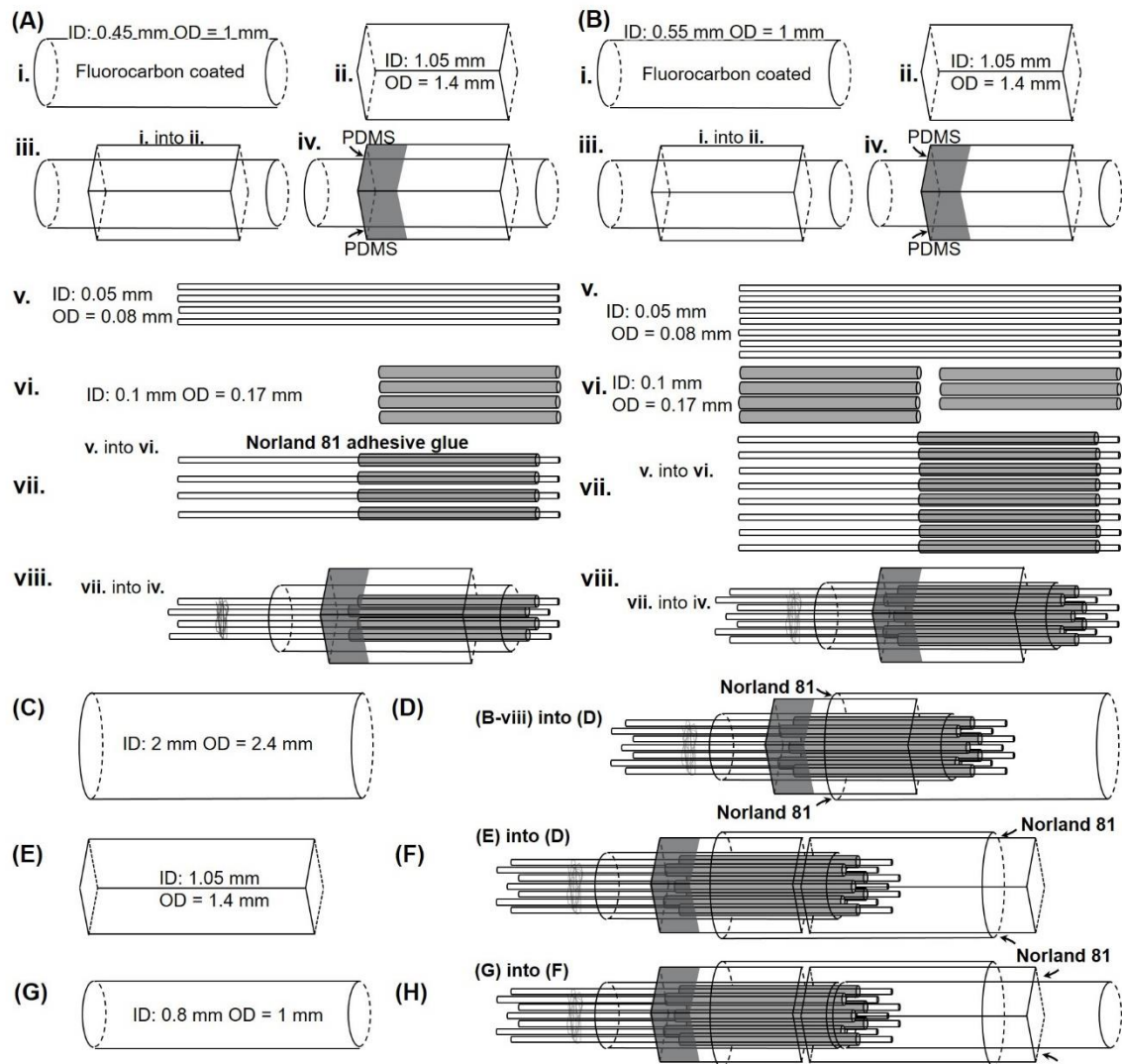
Note. (A) Capillary combination to create rotational flow of water in the flow channel to generate 1-4 fibers. (B) Capillary combination to create rotational flow of water in the flow

channel to generate 1-7 fibers. (C)-(H) Addition of round, square and round capillary step by step to make the device compatible in the rotating system made of metal.

After assembling the capillaries with the PDMS and the extrusion capillary combination, a round capillary of ID 2 mm and OD 2.4 mm, square capillary of ID 1.05 mm and OD 1.4 mm, and a round capillary of ID o.8 mm and OD 1 mm are connected from the right side as shown in the Figure 51C-H. The capillary combination is glued by using 5 minute epoxy and feeding chambers are added at the suitable location as introduced in the chapter 3. Figure 52A shows the final design of the microfluidic system and the rotating metallic parts. The gear connected with the device is attached to the external gear attached in a DC motor to activate rotation during the experiment.

5.5 Continuous Fabrication of Bijel Ropes

Continuous collection of bundles is realized by submerging the outlet of the microfluidic device into a rotating water filled container. Figure 52B shows a schematic depiction and a photograph of the microrope collection in a rotating water bath. The microrope emerges from the rotating capillary of the microfluidic twisting device, which is submerged in the rotating water bath. The rotation of the water in the container drags the microrope into a horizontal orientation. The density difference between the microrope and the water determines now whether the microrope will sink or rise along a helical path in the rotating collection container. If the microrope has a lower density, it will float up to the air/water interface and after one container rotation destructively collide with the rotating capillary of the microfluidic twisting device.

In contrast, if the microrope density is higher than the water density, it will sink down to the bottom of the container and heap up continuously as shown in the photograph of Figure 52C. However, this second preferred collection mechanism conflicts with the criterion necessary for the microrope to remain centered during microfluidic twisting, which requires the microrope to have a lower density than the surrounding water.

Figure 52

Continuous Collection of Microropes
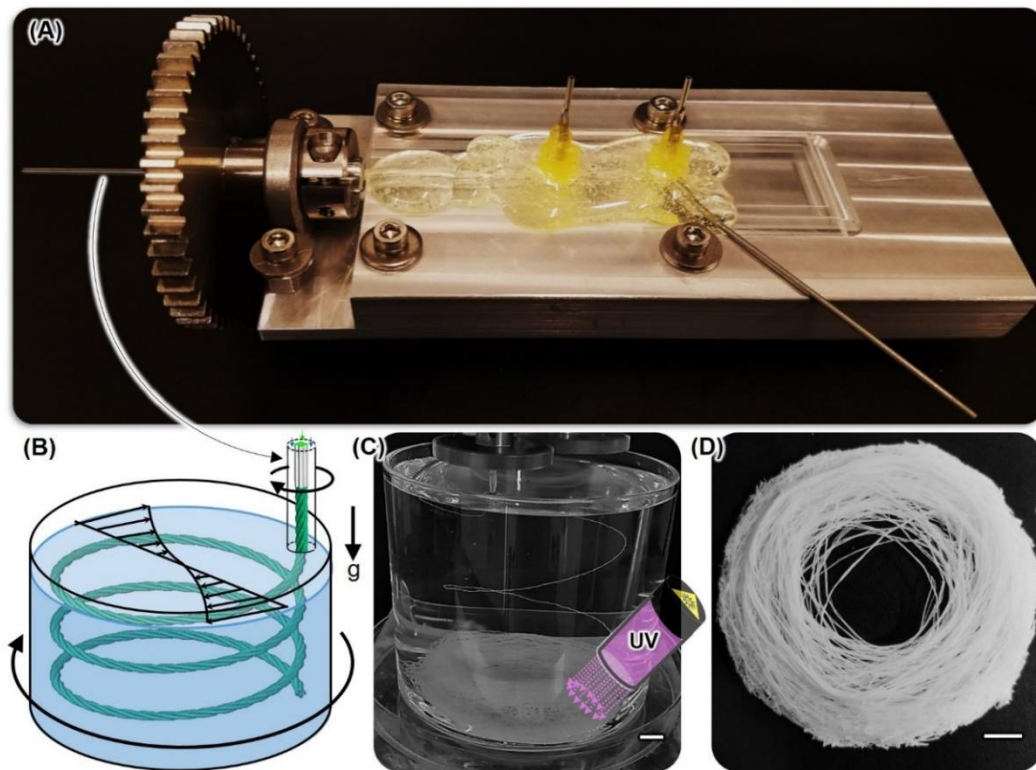
Note. (A) Final design of the microfluidic device attached in the rotating system. (B) Schematics depicting the collection of microropes in a water filled rotating cylinder. Photograph of microrope collection, scale bar 1 cm. (C) Micrographs of collected and

photopolymerized microropes, and a micrograph of the coil of polymerized rope is shown in (D). Thus, the density of the microrope must be lower than the water density while it is still in the microfluidic twisting device. But, as the microrope emerges into the collection container, the density must exceed the water density. This can be realized by keeping the length of the rotating capillary slightly shorter than the microrope travelling distance to reach $\rho(t) = \rho_{water}$. Then, the microrope will not undulate in the microfluidic device, and as it emerges into the collection container sink down. We realize this successfully as shown in Figure 51C. A coil of microropes collected via this approach are shown in Figure 51D.

5.6 Scanning Electron Microscopy (SEM)

We used Scanning Electron Microscope (SEM) (Phenom Pure Desktop SEM) to image bijel ropes. Dry samples are sputter-coated with gold particles before being imaged by scanning electron microscope. Solid fiber ropes can be obtained after polymerization by UV-light exposure on bijels with acrylic monomers as the oil phase (e.g. butanedioldiacrylate). Figure 53 shows the SEM images of straight and contorted ropes.

Up to 7 fibers can be twisted into a single bundle with the capillary combinations employed here. To this end, a desired number of extrusion capillaries (50 µm nozzle diameter) are positioned within the outer tube (0.8 mm inner diameter). Figure 54A illustrates the nozzle configuration and twisting process of bundles made with 3, 4, 5 and 7 fibers. Scanning electron microscopy shows the bundle geometry and the asymmetric internal fiber structure (Figure 54C).

The nozzle positioning controls the bundle organization. With 3 and 4 nozzles, extrusion takes place at the same radial position. As a result, the fibers twist uniformly around each other. However, for 5 and 7 nozzles the fibers are twisted around one central fiber as illustrated in Figure 54A. A collection of longer segment of bijel ropes with various number of fiber strands is shown in the Figure 55.

Figure 53

Scanning Electron Microscopy (SEM) Imaging
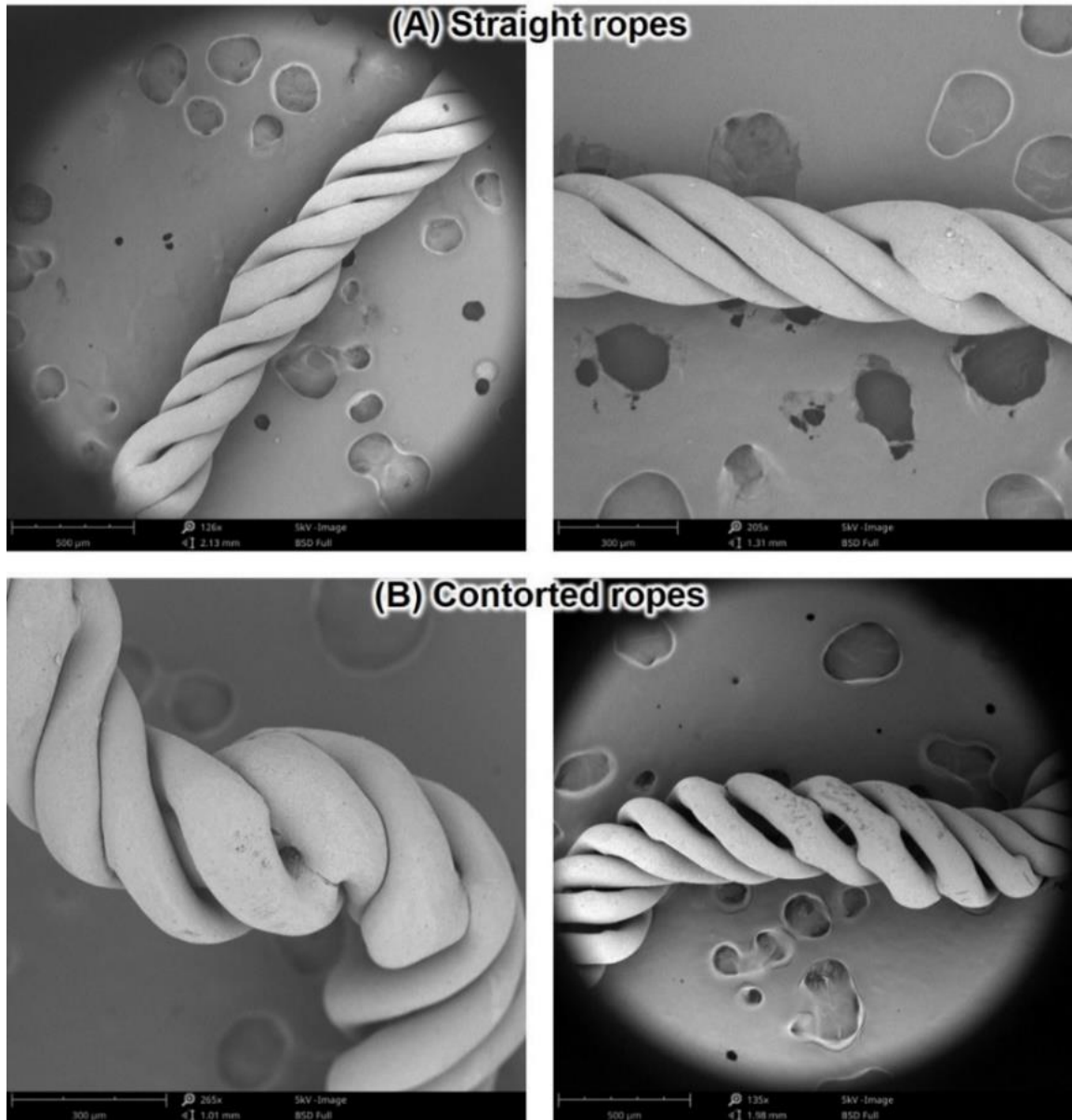
Note. **(A)** Straight ropes when the ropes stays at the center of the channel during experiment

(B) Contorted ropes because of the undulation during experiment.

Figure 54

Fabrication of Ropes with Variable Number of Fibers and SEM Images
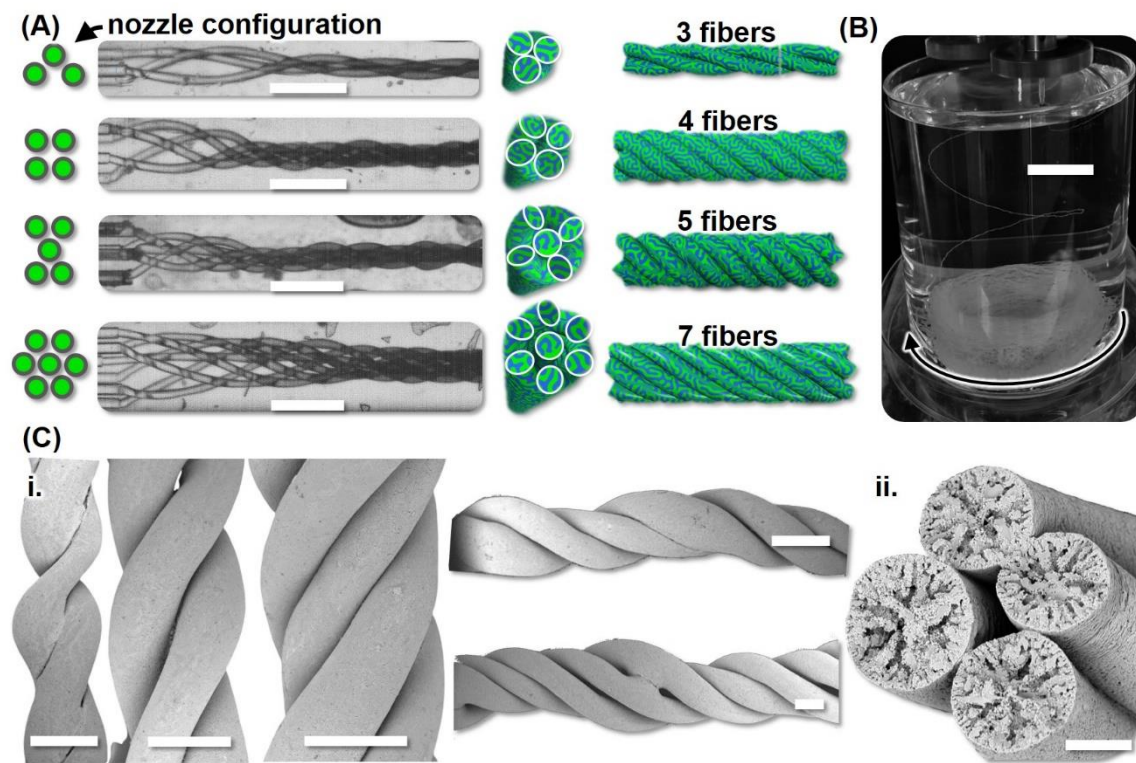
Note. (A) Left: Schematics showing radial positions for different numbers of extrusion nozzles. Middle: Corresponding micrographs of bundles with 3, 4, 5, and 7 fibers at 3000 rpm and 0.8 ml/min water flow rate (scale bar: 0.5 mm). Right: 3-dimensional schematics of cross-sectional and side views of fiber bundles with $3, 4, 5, and\ 7$ fibers. (B) Photograph of a bundle exiting the microfluidic device into a rotating water filled vial (scale bar: 1 cm). (D) Scanning electron microscopy, (i): Side views of bundles with 2, 3, and 4 fibers (scale bar: 0.1 mm). (ii): Cross sectional view of a bundle (scale bar: 0.05 mm).

Figure 55

Micrographs of the Various Kind of Collected Ropes in Larger View
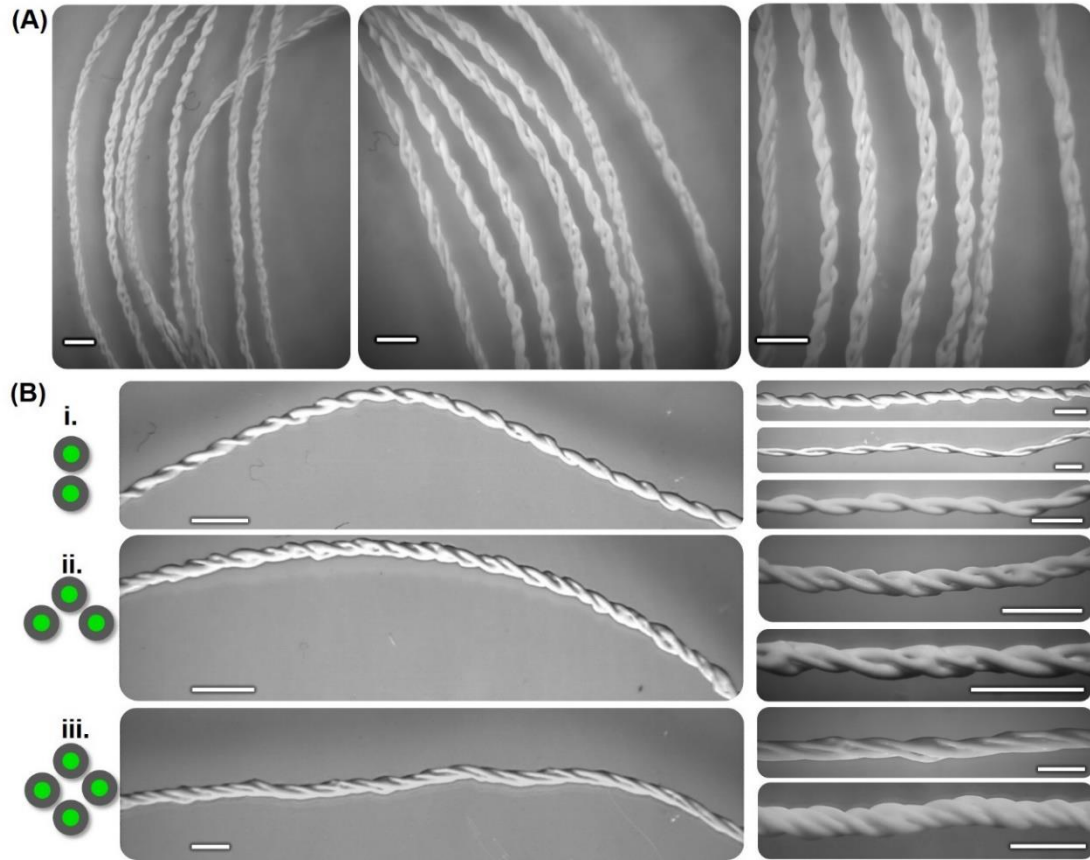
Note. (B) 2, 3 and 4 fibers rope with their nozzle orientation in the left, a longer view of the correspond rope at the middle and ropes with various helix angle and diameters are shown on the right. Scale bar 0.5 mm.

5.7 Confocal Microscopy

Fluorescence dye (Nile red) is added to the fiber casting mixture to image the bijels under the confocal fluorescence microscope (IX-73 OLYMPUS connected to Thorlabs

confocal scanner). The polymerized bijel ropes are washed with ethanol before being soaked in diethyl phthalate (DEP) for refractive index matching. To observe the bicontinuity in fibers, they are illuminated with blue laser light (488 nm) and imaged using a confocal microscope. Figure 56 shows the confocal images of various kind of bijel ropes. It further proves that the bijel structure remains preserved during microfluidic twisting production.

Figure 56

Confocal Images of Bijel Microropes
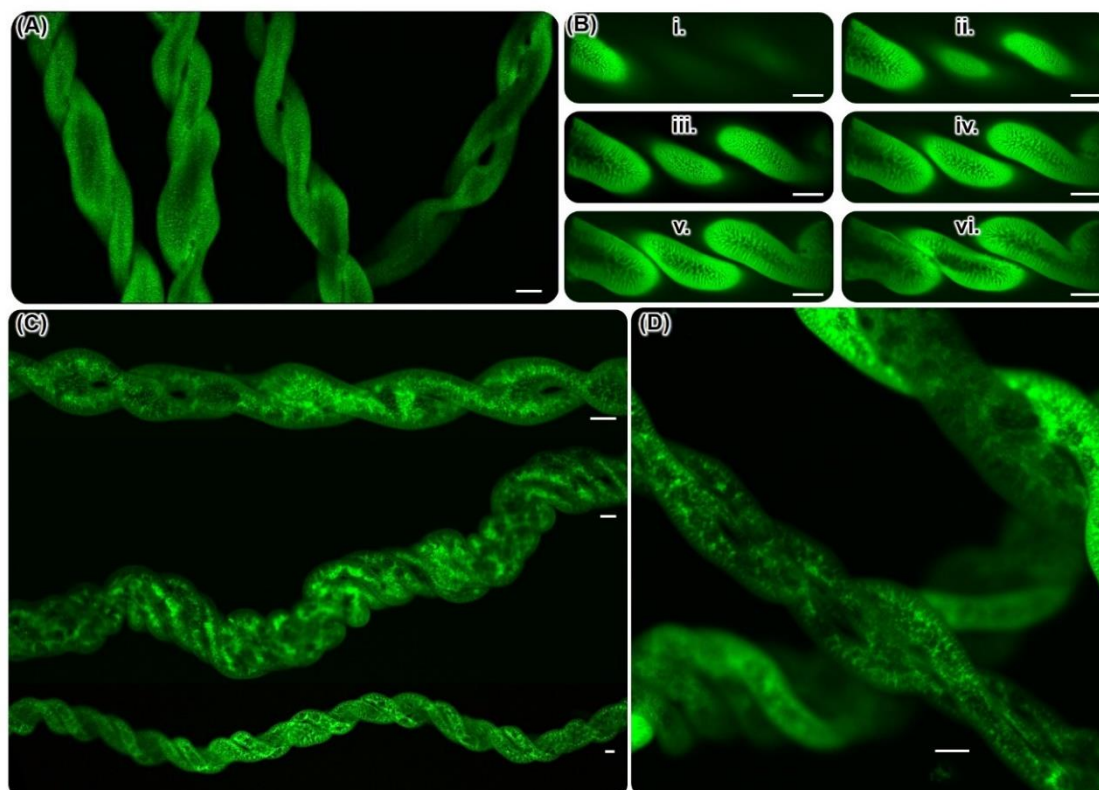
Note. (A) Micrograph representing collection of two fibers ropes. (B) Micrographs representing different lateral planes of the ropes from bottom to equatorial plane (i-vi). (C-D) Micrographs representing a longer segment of 2, 3 and 4 fibers ropes. Scale bar 50 μm.

5.8 Composite Bijels

Feeding the extrusion nozzles with separate liquid casting mixtures enables the formation of composite bijel fiber bundles. This is realized by making some of the fiber extrusion nozzles longer than others, and fiber casting mixtures of various kinds are feeded through the extrusion nozzles separately. We demonstrate this by introducing two fluorescent dyes (Nile Red and Coumarin 6) into different bijel casting mixtures. The polymerized bundles made of fiber strands containing different dyes are visualized with a confocal laser scanning microscope operated in dual channel mode (channel 1: 500-550nm, channel 2: >630nm) (Figure 57). 2 and 4 fibers rope along with their capillary organization is shown in the Figure 58.

Figure 57

Absorption (Left) and Fluorescence (Right) Spectra of Nile Red and Coumarin 6
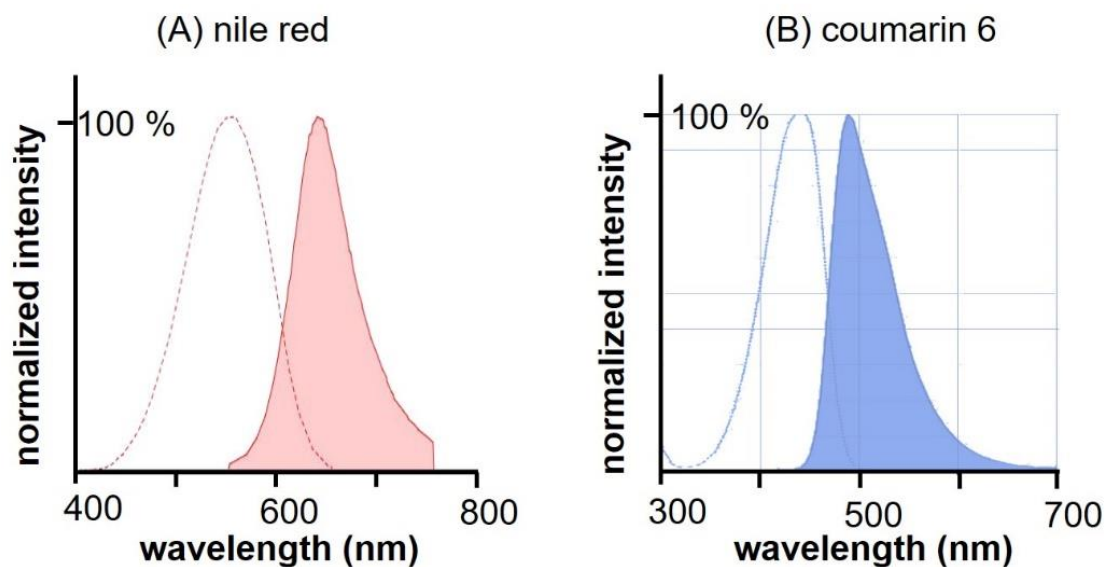
Figure 58A shows how we carried out experiments to fabricate composite bijel ropes from 2 and 4 fiber strands. Figure 58B-C shows confocal laser scanning micrographs of composite bijel fiber bundles. As discussed earlier, bundles formed with 2, 3, and 4 extrusion nozzles contain exclusively twisted fibers. In contrast, with 5 extrusion nozzles the central fiber remains untwisted. This unique architecture enables the formation of high-tensile strength bijel fiber ropes by selective polymerization.

Figure 58

Microfluidic Device Design to Fabricate Composite Bijel Ropes (2 And 4 Fibers)
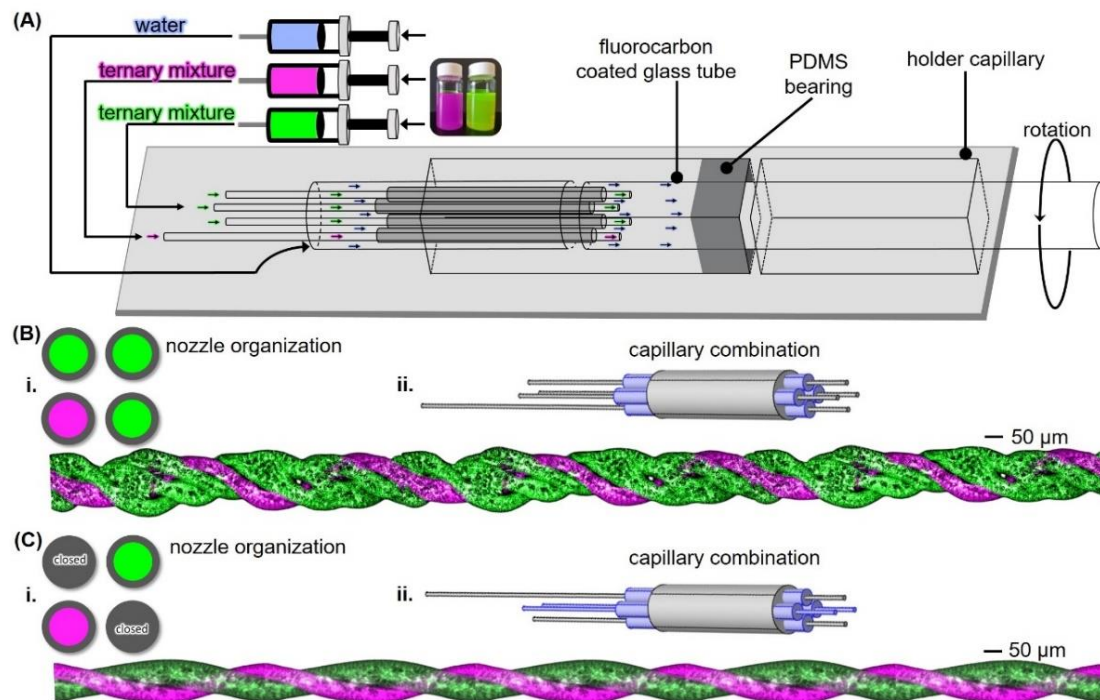
Note. (B) Composite ropes formed by feeding one ternary mixture via 3 extrusion capillaries (green) and another kind of ternary mixture via another capillary (pink): (i) nozzle organization (ii) capillary combination (iii) composite rope. (C) Composite ropes formed by feeding one ternary mixture via 1 extrusion capillaries (green) and another kind of ternary mixture via another capillary (pink). Rest of the two capillaries are closed by using Norland 81 adhesive glue. (i) nozzle organization (ii) capillary combination (iii) composite rope.

5.9 Selective Polymerization and Tensile Strength Measurements

Figure 59

Microfluidic Device Design to Fabricate Composite Bijel Ropes (5 Fibers)
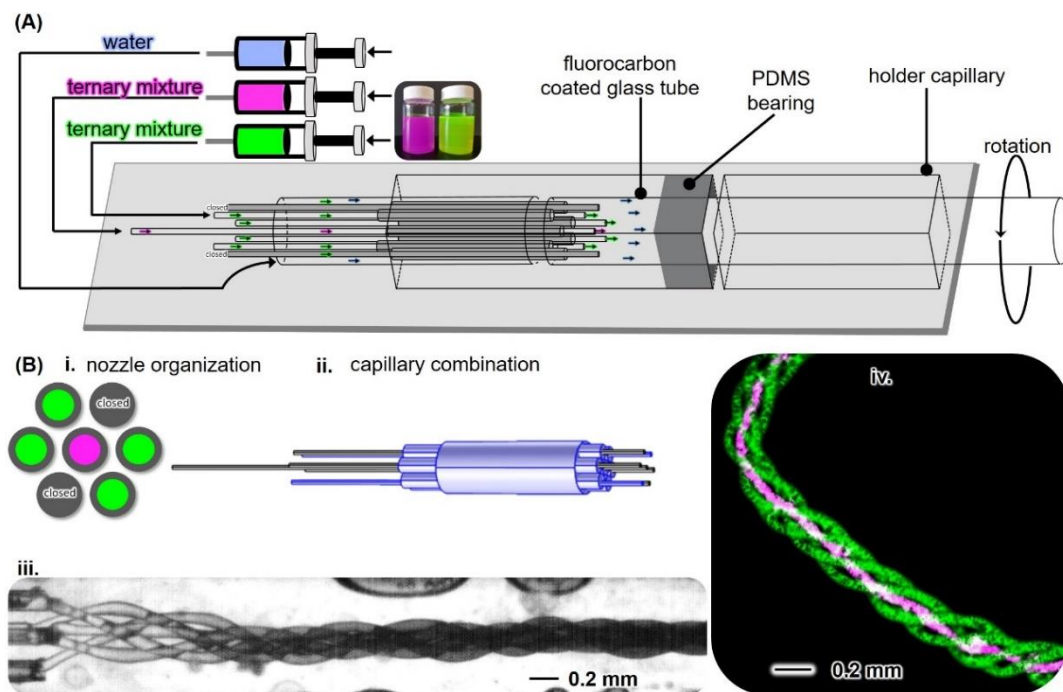
Note. (A) Microfluidic device design to fabricate composite bijel ropes of 5 fiber strands. (B) (i) Nozzle organization (ii) Capillary combination (iii) Micrograph representing 5 fibers ropes during extrusion captured by using high speed camera. (iv) Confocal image of 5 fibers rope with 4 liquid fibers around central polymeric fiber strand.

A bijel rope made of 5 fiber strands can be fabricated by blocking two extrusion nozzles in the 7-fiber capillary combination (Figure 59A). In this capillary combination the central fiber remains straight while outer 4 fibers twist around the central fiber. The

capillary nozzle organization, capillary combination, a micrograph of the ropes during extrusion and confocal image of the ropes after collection is shown in the Figure 59B.

Selective polymerization is carried out while twisting 4 fibers made of diethylphthalate around a central fiber containing monomer and photoinitiator (ethylene glycol dimethacrylate and 2-hydroxy-2-methylpropiophenone). UV-light irradiation polymerizes only the central fiber, while the 4 twisted fibers remain liquid (Figure 59B-iv). Unlike unpolymerized bundles, the polymer/liquid fiber composite can be picked up with tweezers without breaking. We mount this composite in a tensile tester and record the stress vs. strain curve. The bundles with a cross section A and an original length L_0 are elongated by ΔL via an applied force F. The strain $\varepsilon = \Delta L / L_0$ and the stress $\sigma = F/A$ are then calculated. The original stress-strain curves are non-linear due to straightening of the curved bundle during the experiment (Figure 60A). However, after straightening, the bundles elongate linearly. The linear parts of 3 averaged and rescaled stress-extension measurements are shown in Figure 60C. An average tensile strength of 20 ± 3.1 MPa is found, which is roughly 4000 times higher than that of the liquid bijel [39] fibers. The slope of the linear stress/strain trend gives the elastic modulus E. The average elastic modulus amounts to 1.1 ± 0.4 GPa, reflecting the stiff nature of the highly cross-linked poly(ethylene glycol).

While the unpolymerized liquid twisted fibers remain fragile, the polymerized central fiber acts as a backbone for the unpolymerized twisted fibers. Our tensile strength measurement captures only the mechanical strength of the central fiber since the contribution of the twisted fibers to the tensile strength is negligible. Measuring the stress-extension of a single polymerized fiber shows the same magnitude of tensile strength as

the composite bundle (13 ± 3 MPa, Figure 61F). The slightly lower tensile strength of the individual fiber is related to differences in the initial ternary mixture used for fiber extrusion, resulting in a lower connectivity of the polymerized domains within the internal structure of the fiber (Figure 61 F).

Figure 60

Stress vs. Strain Curve of Ropes (Linear Section)
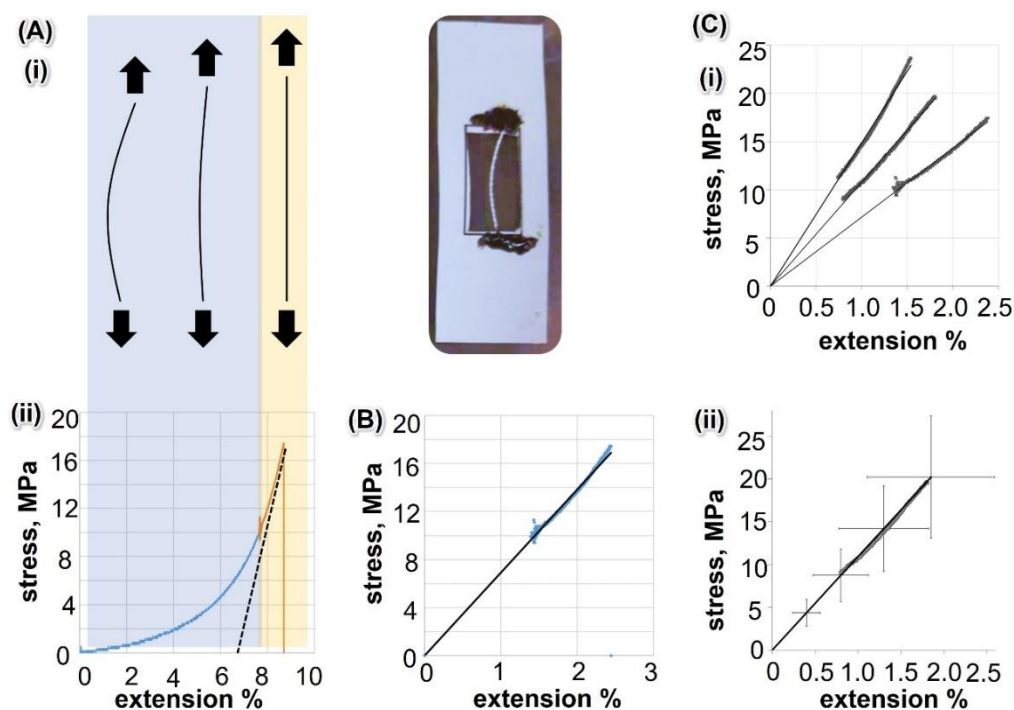
Note. (A) (i) A diagram depicting how composite rope straightens under load (left), and a sample prepared for tensile strength testing (right). (ii) An example of a stress-strain curve measurement obtained from the experiment. (B) Linear part of the elongation. (C) The linear sections of three separate measurements are displayed (i), as well as the averaged and rescaled stress-strain curves for those measurements (ii).

Figure 61

Selective Polymerization
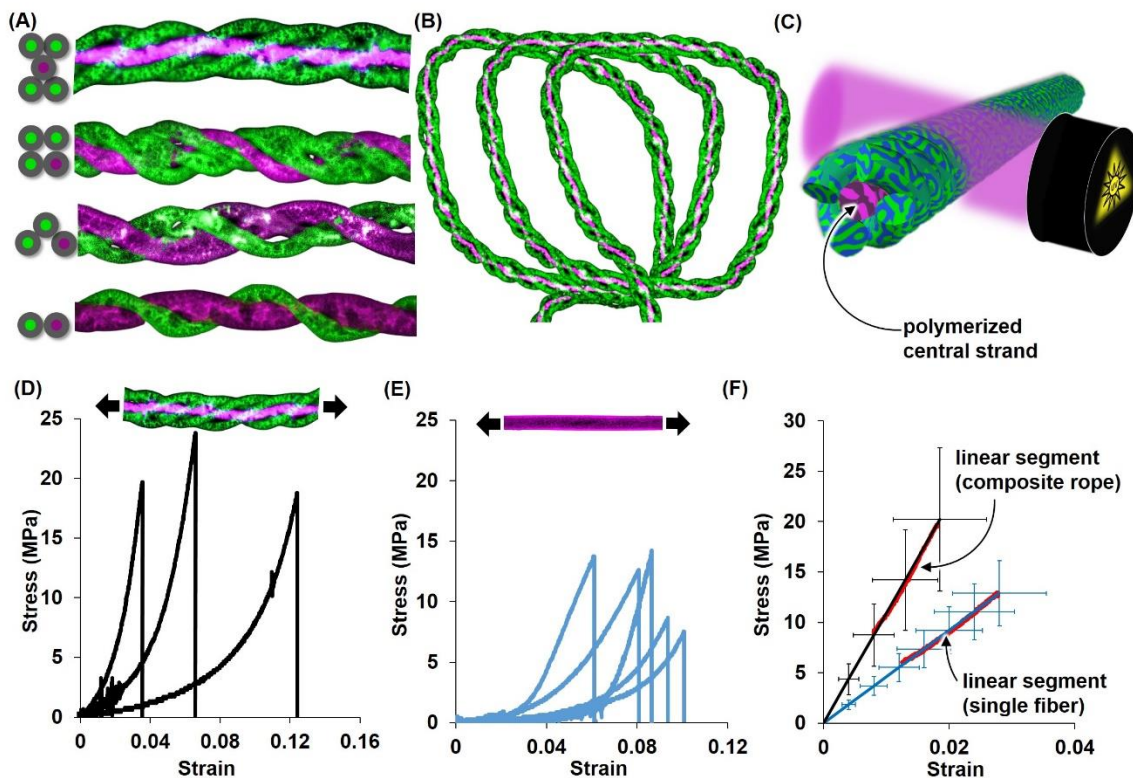
Note. (A) A collection of composite ropes with variable number of fiber strands. (B) A larger view of a five-fiber rope, showing the center polymerized fiber strand (magenta) and the surrounding four liquid fibers weaving around it (green). (C) Diagrams illustrating selective polymerization of the center fiber in a five-fiber bundle. (D) Tensile strength of a rope containing one polymerized center fiber and four unpolymerized twisted fibers. (E) Single polymerized bijel fiber and tensile strength measurement (5 different samples). (F) Stress-strain variation during deformation as a result of applied load, only reflecting the linear segment, as described in Figure 60.

During mechanically demanding applications of the composite bijel fiber bundle, the polymerized central fiber will uptake the main load, with minimal mechanical stress and deformation of the 4 twisted liquid bijel fibers. This configuration is advantageous, because it allows to exploit the liquid like properties of the unpolymerized bijel fibers with potentials in fluid transport and biphasic catalysis, while simultaneously providing the high mechanical strengths of a polymeric material.

Our experimental work includes the mechanical tests for a bundle with one centered polymerized fiber and 4 twisted fibers at a constant angle of 42 degrees. Since the central fiber provides the main mechanical support, changing α or the number of unpolymerized fibers does not significantly affect the tensile strength. The diameter of the central polymerized fiber will change the absolute force needed for breaking, but not the cross-sectional area normalized tensile strength. The main control parameter to change the tensile strength is the composition of the ternary mixture used to generate the central polymerized fiber. The ternary composition affects the interconnectivity of the polymerized domains within the central fiber. However, more experimental research is needed to understand the mechanical properties of the composite bundles in dependence of the ternary mixture composition.

5.10 Bijel-Derived Hydrogels

A hydrogel is a three-dimensional network of hydrophilic polymers that can swell in water and hold a large amount of water while retaining their structure due to chemical or physical cross linking of individual polymer chains.[98] For a material to be classified as a hydrogel, water must account for at least 10% of its total weight (or volume). Because of their high water content, hydrogels have a high degree of flexibility. The presence of

hydrophilic groups such as -COOH, -OH, -CONH, and others contribute to the network's hydrophilicity.

In response to certain physical and chemical stimuli, hydrogels undergo a significant volume phase transition or gel-solution phase transition. Temperature, electric and magnetic fields, solvent composition, light intensity, and pressure are examples of physical stimuli, whereas pH, ions, and specific chemical compositions are examples of chemical or biochemical stimuli.[99][100][101] However, in the vast majority of cases, such conformational transitions are reversible. As a result, the hydrogels can return to their original state. The nature of the monomer, charge density, pendant chains, and degree of cross linkage all influence the response of hydrogels to external stimuli. The magnitude of response is also directly proportional to the applied external stimulus.

Any pH sensitive polymer contains acidic (e.g., carboxylic and sulfonic acids) or basic (e.g., ammonium salts) groups that respond to pH changes in their environment by gaining or losing protons. Poly electrolytes are polymers with a high concentration of ionizable groups. Anionic poly electrolytes, such as poly (acrylic acid) (PAA), are deprotonated in a basic environment, causing electrostatic repulsions between the chains to increase dramatically, allowing water molecules to penetrate and causing the hydro-gel to swell dramatically. In an acidic environment, however, the acidic polymer protonates, resulting in a decrease in charge density and polymer volume collapse.[102]

Cationic poly electrolytes, on the other hand, such as poly (N, N9-diethylaminoethyl methacrylate), become ionized and swell in acidic pH. Because amphilic hydrogels contain both acidic and basic moieties, they have two phase transitions in both acidic and basic environments, rather than just one in neutral media.

Twisted soft material fibers have recently attracted interest in the field of mechanosensitive materials such as soft robots, actuators, wearable electronic devices, and so on. Is it possible to use composite bijels as mechanosensitive materials? It has already been demonstrated that pH responsive poly (acrylic acid) (PAA) hydrogel fibers can be derived from bijels composed of HDA cross-linked poly (tertiary butyl acrylate).[103] In a basic solution with higher flexibility, these bijel-derived hydro-gel fibers swell dramatically. These stimuli responsive fibers were predicted to be a promising candidate for use as smart fibers that open/close their surface pores in the presence of different pH values.

However, the swelling behavior of such hydrogels in response to varying amounts of cross linker has yet to be realized. The understanding behind the swelling behavior of these bijel-based hydrogel fibers based on cross-linker concentration variation could be important step in the application towards mechanosensitive materials. Furthermore, the mechanical response of hydrogels derived from various bijel structures such as fibers, hollow fibers, helices, and ropes with varying cross linker concentration can have different applications in soft robotics. For example, if a single hydrogel-helix made of bijels exhibits shrinking and expanding behavior at low and high pH environments, it may be used to create a pH responsive mechanical spring.

To address this curiosity, we conducted a systematic study of the mechanical behavior of hydrogel ropes derived via the bijel route. This task is completed by selecting a suitable ternary mixture combination in which the fibers generated will be able to transform into hydrogels after post-processing.

5.11 Ternary Composition of t-BA, Water and Methanol

Figure 62

Ternary Phase Diagram: Tertiary Butyl Acrylate, Water and Methanol System
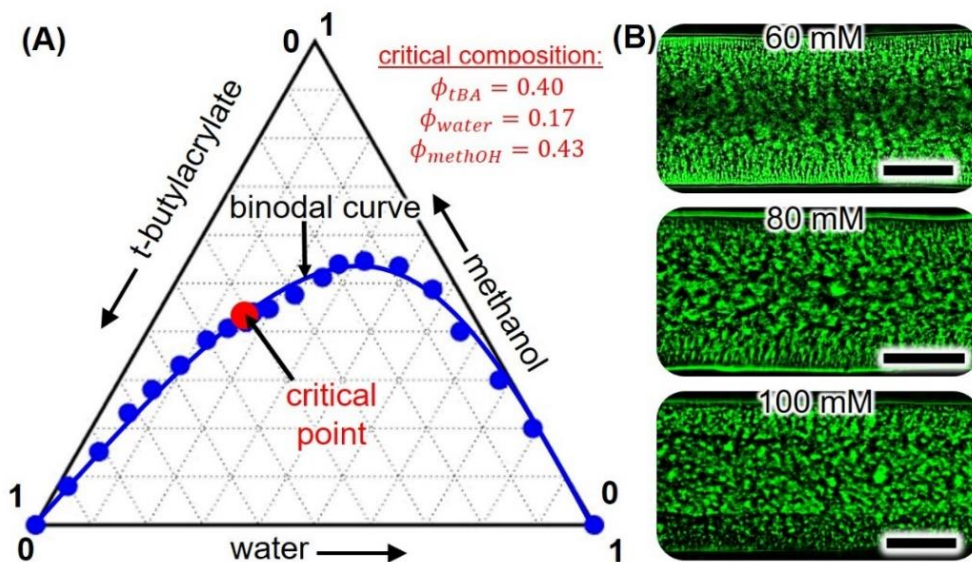
Note. (A) Ternary phase diagram demonstrating binodal curve and critical point. (B) Confocal micrographs of the bijel fibers with various CTAB concentrations. The black domain represents water phase and the green domain represents the polymerized oil phase, scale bar 50 μm.

We used the same method described in chapter 4 to determine the ternary composition of t-BA, water, and methanol. The binodal curve is obtained from turbidimetry measurements, and the critical composition is determined by observing the emulsion transition. By examining the transition from tBA-in-water (oil/water) to water-in-tBA (water/oil) emulsions, we were able to identify the critical point. We determined this

composition by using a confocal microscope to detect the emulsion type by adding the fluorescent dye Nile Red to immiscible ternary mixes at different points near to the binodal line. The fluorescence emission during confocal imaging helps determine the kind of emulsion since Nile red partitions to the oil phase. The critical point results with $\phi_{tBA} = 0.40$, $\phi_{methOH} = 0.43$ and $\phi_{water} = 0.17$ (Figure 62A).

The critical composition is used to make fibers with different CTAB concentrations by using a simple microfluidic device. The composition that produces the best bijel structure is chosen for further investigations. Micrographs representing bijel structures at various CTAB concentrations is shown in the Figure 62B.

5.12 Fibers with Various Cross-linker Conc. in the Fiber Casting Mixture

Figure 63

SEM and Confocal Images of t-BA Fibers
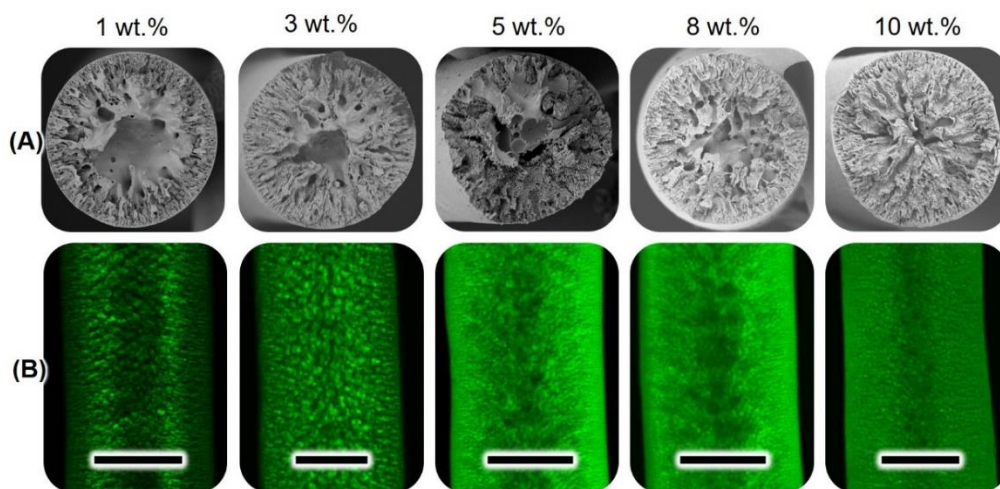
Note. **(A)** SEM micrographs representing the cross-section of the fiber at different cross linker concentration in the fiber casting mixture. **(B)** Confocal image of the fiber

representing the equatorial plane of the fiber at different cross-linker concentration in the fiber casting mixture. Scale bar 50 μm.

In the ternary mixture, we use poly (tert-butyl acrylate) as an oil phase and a small amount of ethylene glycol dimethacrylate (EDMA) as a cross-linking agent in poly (tert-butyl acrylate) (tert-butylacrylate). We varied the cross-linker concentration from less than 1% to 30%, and their bijel structures were investigated (Figure 63). The polymerized fibers are then subjected to hydrolysis procedures in order to be converted into polyacrylic acid (PAA) hydrogels.

5.13 Hydrolysis Scheme

The hydrolysis scheme is shown in Figure 64A. For 12 hours, the polymerized fibers are immersed in a mixture of 20% formic acid and trifluoroacetic acid. The acid mixture is replaced three times with ethanol and then with water. The fiber swelling behavior is then studied by varying the pH of the surrounding environment around the fibers.

In a basic solution, these bijel derived hydrogel fibers swell dramatically (Figure 64B). When the pH of the buffer solution is reduced, fibers regain their previous shape and size. At a crosslinker concentration of 1 wt. % and below, the diameter of the bundles increases by about two times, and it reduces approximately exponentially as the cross-linker concentrations increase (Figure 64C). Interestingly, we observed that the length of the fiber also increases dramatically at high pH. Our observation shows that the fiber swells in the longitudinal and lateral directions with the same aspect ratio. Why the fibers

deform in the similar ratio in longitudinal and lateral direction? We believe the reason could be the bicontinuous porosity in the fibers, or due to the cross-linker chain evolution within the bijel, but it is too early to answer this question which requires more experimental results.

Figure 64

Hydrolysis Scheme
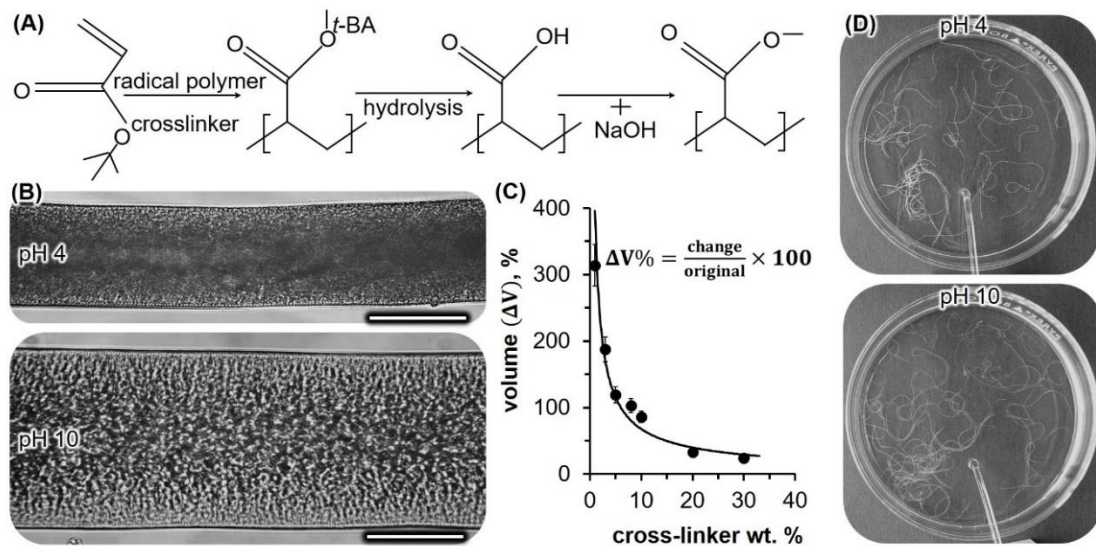
Note. **(A)** Scheme to fabricate pH-responsive poly (acrylic acid) hydrogel by hydrolysis of bijels composed of EDMA cross-linked poly (tert-butyl acrylate). **(B)** Micrographs (bright field) representing bijel fibers at pH4 and pH 10, scale bar 100 μm. (C) A graph representing percentage change in volume during swelling in the basic solution (pH 10) against the cross linker concentration in the fiber casting mixture. (D) Micrographs representing multiple fibers at different pH environment.

5.14 Bijel Derived Hydrogel Ropes

We used 4 fibers capillary combination to extrude bijel ropes with twisted fiber strands from 2 to 4. The bijel ropes are collected continuously by controlling the shear stresses (chapter 3) and the centrifugal force effect (chapter 4). After UV induced polymerization, we hydrolyze the EDMA cross-linked poly (tert-butylacrylate) ropes in a mixture of trifluoroacetic acid and formic acid to create the EDMA cross-linked poly(acrylic acid) hydrogel ropes. The swelling and shrinking behavior of these ropes are then investigated (Figure 65).

Figure 65

Bijel Derived Hydrogel Ropes

(B) $$\alpha = f(H, D) = \cos^{-1}\left[\left(\frac{r}{h}\right) + 1\right]^{-\frac{1}{2}}$$

$D = 2r$
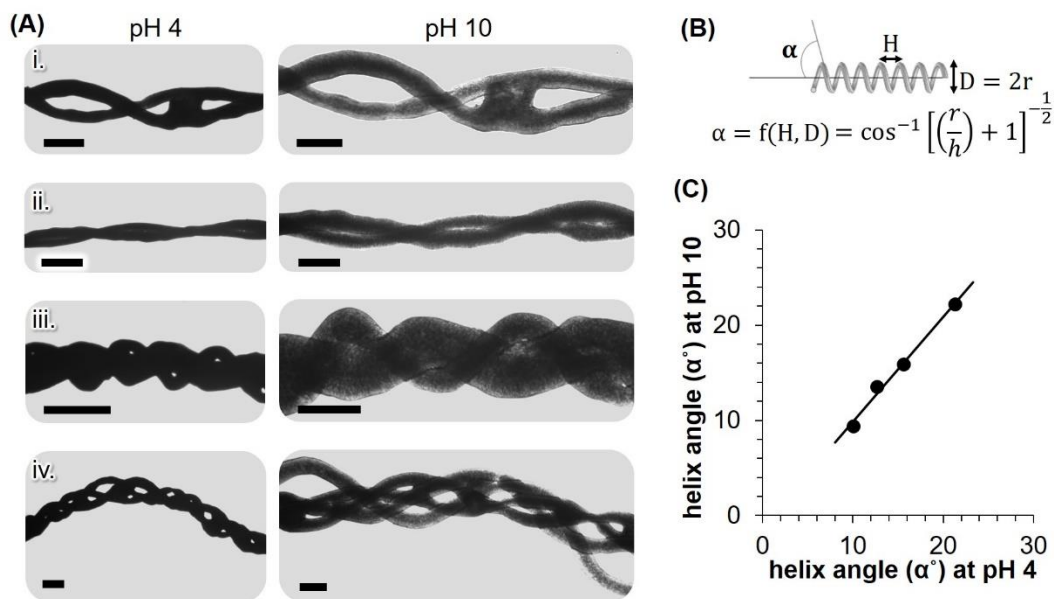
Note. (A) 2 and 4 fibers ropes with various helix angle at various pH, pH4 (left) and at pH 10 (right), scale bar 0.2 mm. (B) Schematic illustration how we measured pitch length and

diameter for the estimation of helix angle. (C) Helix angle of the ropes at pH 10 against at pH4.

In a basic solution, these ropes swell dramatically in the same way that a single fiber does. They also return to their original shape and size when the pH of the environment is restored to its original level. They show transient kinetics during swelling and shrinking due to water intake during swelling and water uptake during shrinking, but we couldn't identify any chirality during deformation. We also calculated the helix angle for each rope at low and high pH levels and discovered the same value (Figure 65C). The aspect ratio of deformation remains constant in both the longitudinal and lateral directions. This demonstrates that the rope's identity is preserved regardless of the environment. By feeding ternary solutions including various cross-linker concentrations and active ingredients, this method can be used to produce composite hydrogel ropes in future.

5.15 Conclusion

Based on the understanding of shear stresses and centrifugal force effect, we successfully demonstrated the collection of long microropes without destructive wall collision. The confocal imaging and Scanning electron microscopy imaging shows that the bijel structures during twisting remains preserved. In addition, combining multiple bijel fibers of different compositions enables the introduction of polymeric support fibers to raise the tensile strength to tens of megapascals, while simultaneously preserving the liquid like properties of the bijel fibers for transport applications. Moreover, we fabricated stimuli responsive hydrogels derived from bijel routes and studied the deformation behavior at different pH environment.

Chapter 6

Conclusions and Future Directions

In this thesis, we studied a new direction in the field of microfluidics, which we call helical microfluidics because it arises from continuous rotational and translational flow of fluids. We advanced our understanding of the helical flow field by quantifying three fundamental physical quantities involved: translation shear stress, rotation shear stress, and centrifugal force effect. Controlling the effect of shear stress allows us to control the geometrical features of the suspended objects, while estimating the centrifugal force effect within the fluids allows us to manipulate the location of the suspended objects. In addition, helical flow of fluids can be used to develop composite materials by incorporating the fluids with the device geometry.

We believe that composite ropes fabricated by employing helical microfluidics can be transferred into adaptive smart materials by coupling their internal and external environment. We have demonstrated continuous production of microscopic ropes, which have potential applications as composite materials in catalysis, tissue engineering, soft robotics, and additive manufacturing. In the future, conductive polymer ropes could be developed to make mechanosensitive micro machines in the presence of external electromagnetic field. We have successfully demonstrated helical microfluidics for fiber twisting, centrifugal assembly of fibers and fabricating new composite materials. We think that by incorporating helical microfluidics and fluid properties, we can use it for mixing and separation process.

Moreover, the knowledge gained from this work can be applied on other researches beyond bijel fiber assemblies. We have demonstrated three distinct direction of helical microfluidics to be used for twisting, assembly, and composite material synthesis. Another potential application of helical microfluidics can be mixing and separation of colloidal fluids depending on their inherent characteristics. With these advantages, we believe that helical microfluidics can become a new unit operation in microfluidics, advancing high-throughput screening, lab-on-a-chip diagnostics, biochemical assays, and material synthesis. The outlook of this dissertation based on our experimental results is presented in the chart below.

Figure 66

Outlook of the Dissertation Illustrating the Applications of Helical Microfluidics
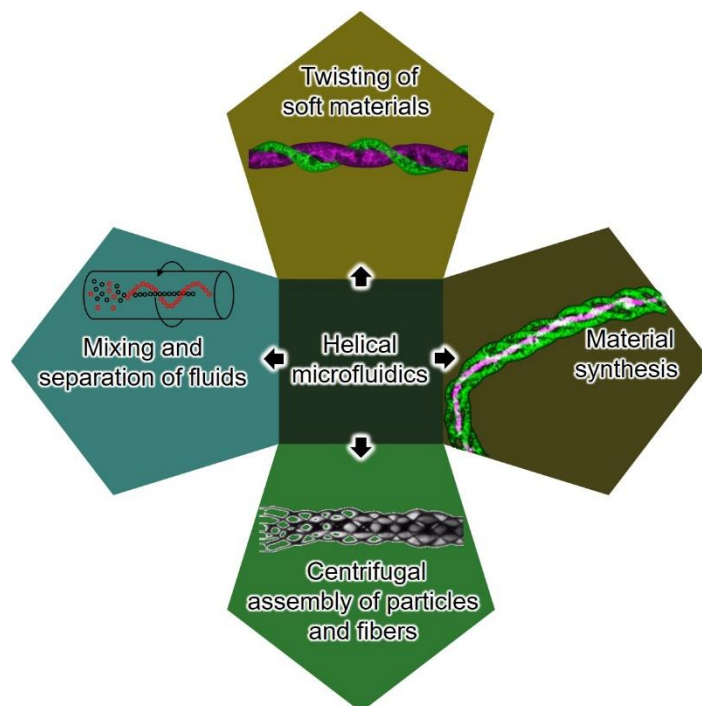
Note. (i) Twisting of soft materials (ii) Centrifugal assembly of particles and fibers (iii) Material synthesis (iv) Mixing and separation of colloidal fluids.

References

[1]   S. Sagadevan, "Recent trends on nanostructures based solar energy applications: A review," *Reviews on Advanced Materials Science*. 2013.

[2]   S. Martha, P. Chandra Sahoo, and K. M. Parida, "An overview on visible light responsive metal oxide based photocatalysts for hydrogen energy production," *RSC Advances*. 2015, doi: 10.1039/c5ra11682a.

[3]   A. J. Ragauskas *et al.*, "The Path Forward for Biofuels and Biomaterials\r10.1126/science.1114736," *Science (80-.).*, 2006.

[4]   J. H. Clark, "Green chemistry for the second generation biorefinery - Sustainable chemical manufacturing based on biomass," *J. Chem. Technol. Biotechnol.*, 2007, doi: 10.1002/jctb.1710.

[5]   D. S. Sholl and R. P. Lively, "Seven chemical separations to change the world," *Nature*. 2016, doi: 10.1038/532435a.

[6]   P. Kumar, D. M. Barrett, M. J. Delwiche, and P. Stroeve, "Methods for pretreatment of lignocellulosic biomass for efficient hydrolysis and biofuel production," *Industrial and Engineering Chemistry Research*. 2009, doi: 10.1021/ie801542g.

[7]   K. Stratford, R. Adhikari, I. Pagonabarraga, J. C. Desplat, and M. E. Cates, "Chemistry: Colloidal jamming at interfaces: A route to fluid-bicontinuous gels," *Science (80-.).*, 2005, doi: 10.1126/science.1116589.

[8]   E. M. Herzig, K. A. White, A. B. Schofield, W. C. K. Poon, and P. S. Clegg, "Bicontinuous emulsions stabilized solely by colloidal particles," *Nature Materials*. 2007, doi: 10.1038/nmat2055.

[9]   M. F. Haase, K. J. Stebe, and D. Lee, "Continuous Fabrication of Hierarchical and Asymmetric Bijel Microparticles, Fibers, and Membranes by Solvent Transfer-Induced Phase Separation (STRIPS)," *Adv. Mater.*, 2015, doi: 10.1002/adma.201503509.

[10]   T. J. Thorson, E. L. Botvinick, and A. Mohraz, "Composite Bijel-Templated Hydrogels for Cell Delivery," *ACS Biomater. Sci. Eng.*, 2018, doi: 10.1021/acsbiomaterials.7b00809.

[11]   C. A. L. Colard, R. A. Cave, N. Grossiord, J. A. Covington, and S. A. F. Bon, "Conducting nanocomposite polymer foams from lce-crystal-templated assembly of mixtures of colloids," *Adv. Mater.*, 2009, doi: 10.1002/adma.200803007.

[12]   M. Pera-Titus, L. Leclercq, J. M. Clacens, F. De Campo, and V. Nardello-Rataj, "Pickering interfacial catalysis for biphasic systems: From emulsion design to green reactions," *Angew. Chemie - Int. Ed.*, 2015, doi: 10.1002/anie.201402069.

[13]   G. Di Vitantonio, T. Wang, M. F. Haase, K. J. Stebe, and D. Lee, "Robust Bijels for Reactive Separation via Silica-Reinforced Nanoparticle Layers," *ACS Nano*, 2019, doi: 10.1021/acsnano.8b05718.

[14]   S. Cha, H. G. Lim, M. F. Haase, K. J. Stebe, G. Y. Jung, and D. Lee, "Bicontinuous Interfacially Jammed Emulsion Gels (bijels) as Media for Enabling Enzymatic Reactive Separation of a Highly Water Insoluble Substrate," *Sci. Rep.*, 2019, doi: 10.1038/s41598-019-42769-8.

[15]   J. A. Witt, D. R. Mumm, and A. Mohraz, "Microstructural tunability of co-continuous bijel-derived electrodes to provide high energy and power densities," *J. Mater. Chem. A*, 2016, doi: 10.1039/c5ta06260h.

[16]   D. Cai, F. H. Richter, J. H. J. Thijssen, P. G. Bruce, and P. S. Clegg, "Direct transformation of bijels into bicontinuous composite electrolytes using a pre-mix containing lithium salt," *Mater. Horizons*, 2018, doi: 10.1039/c7mh01038a.

[17]   M. F. Haase, H. Jeon, N. Hough, J. H. Kim, K. J. Stebe, and D. Lee, "Multifunctional nanocomposite hollow fiber membranes by solvent transfer induced phase separation," *Nat. Commun.*, 2017, doi: 10.1038/s41467-017-01409-3.

[18]   H. Firoozmand and D. Rousseau, "Food-grade bijels based on gelatin-maltodextrin-microbial cell composites," *Food Hydrocoll.*, 2015, doi: 10.1016/j.foodhyd.2015.02.034.

[19]   M. F. Haase, S. Boakye-Ansah, G. Di Vitantonio, K. J. Stebe, and D. Lee, "CHAPTER 6: Bijels Formed by Solvent Transfer-induced Phase Separation," *RSC Soft Matter*, 2020, doi: 10.1039/9781839160974-00137.

[20]   K. S. Elvira, X. C. I Solvas, R. C. R. Wootton, and A. J. Demello, "The past, present and potential for microfluidic reactor technology in chemical synthesis," *Nature Chemistry*. 2013, doi: 10.1038/nchem.1753.

[21]   C. N. Baroud and H. Willaime, "Multiphase flows in microfluidics," *Comptes Rendus Physique*. 2004, doi: 10.1016/j.crhy.2004.04.006.

[22]   A. Günther and K. F. Jensen, "Multiphase microfluidics: From flow characteristics to chemical and materials synthesis," *Lab on a Chip*. 2006, doi: 10.1039/b609851g.

[23]   A. S. Utada, A. Fernandez-Nieves, H. A. Stone, and D. A. Weitz, "Dripping to jetting transitions in coflowing liquid streams," *Phys. Rev. Lett.*, 2007, doi: 10.1103/PhysRevLett.99.094502.

[24]   Khanal, Anjana, "Dewetting induced lipid bilayer multicomponent scaffold for synthetic cell vesicle and their stability" (2021). *Theses and Dissertations*. 2872. https://rdw.rowan.edu/etd/2872

[25]   M. F. Haase and J. Brujic, "Tailoring of high-order multiple emulsions by the liquid-liquid phase separation of ternary mixtures," *Angew. Chemie - Int. Ed.*, 2014, doi: 10.1002/anie.201406040.

[26]   G. L. Wick and P. F. Tooby, "Centrifugal buoyancy forces," *Am. J. Phys.*, 1977, doi: 10.1119/1.10725.

[27]   R. Hellie, "Kholopstvo I Krepostnichestvo (Konets XV-XVI V.) . By E. I. Kolycheva. Moscow: 'Nauka,' 1971. 255 pp. 99 kopeks. - Zakreposhchenie Krest' Ian I Klassovaia Bor'ba V Rossii Vo Vtoroi Polo Vine XVI V. By V. I. Koretsky. Moscow: 'Nauka,' 1970. 366 pp. 1.40 ru," *Slavic Rev.*, 1972, doi: 10.2307/2493629.

[28]   T. N. Hunter, R. J. Pugh, G. V. Franks, and G. J. Jameson, "The role of particles in stabilising foams and emulsions," *Advances in Colloid and Interface Science*. 2008, doi: 10.1016/j.cis.2007.07.007.

[29]   Z. Wang and Y. Wang, "Tuning Amphiphilicity of Particles for Controllable Pickering Emulsion," *Materials*. 2016, doi: 10.3390/ma9110903.

[30]   M. N. Lee and A. Mohraz, "Bicontinuous macroporous materials from bijel templates," *Adv. Mater.*, 2010, doi: 10.1002/adma.201001696.

[31]   M. N. Lee and A. Mohraz, "Hierarchically porous silver monoliths from colloidal bicontinuous interfacially jammed emulsion gels," *J. Am. Chem. Soc.*, 2011, doi: 10.1021/ja201650z.

[32]   D. Cai, P. S. Clegg, T. Li, K. A. Rumble, and J. W. Tavacoli, "Bijels formed by direct mixing," *Soft Matter*, 2017, doi: 10.1039/c7sm00897j.

[33]   T. Wang, G. Di Vitantonio, K. J. Stebe, and D. Lee, "Scalable Manufacturing of Hierarchical Biphasic Bicontinuous Structures via Vaporization-Induced Phase Separation (VIPS)," *ACS Mater. Lett.*, 2020, doi: 10.1021/acsmaterialslett.0c00080.

[34]   K. A. White, A. B. Schofield, B. P. Binks, and P. S. Clegg, "Influence of particle composition and thermal cycling on bijel formation," *J. Phys. Condens. Matter*, 2008, doi: 10.1088/0953-8984/20/49/494223.

[35]   N. Hijnen, D. Cai, and P. S. Clegg, "Bijels stabilized using rod-like particles," *Soft Matter*, 2015, doi: 10.1039/c5sm00265f.

[36]   J. W. Tavacoli, J. H. J. Thijssen, A. B. Schofield, and P. S. Clegg, "Novel, robust, and versatile bijels of nitromethane, ethanediol, and colloidal silica: Capsules, sub-ten-

micrometer domains, and mechanical properties," *Adv. Funct. Mater.*, 2011, doi: 10.1002/adfm.201002562.

[37]   M. N. Lee, J. H. J. Thijssen, J. A. Witt, P. S. Clegg, and A. Mohraz, "Making a robust interfacial scaffold: Bijel rheology and its link to processability," *Adv. Funct. Mater.*, 2013, doi: 10.1002/adfm.201201090.

[38]   M. N. Lee, M. A. Santiago-Cordoba, C. E. Hamilton, N. K. Subbaiyan, J. G. Duque, and K. A. D. Obrey, "Developing monolithic nanoporous gold with hierarchical bicontinuity using colloidal bijels," *J. Phys. Chem. Lett.*, 2014, doi: 10.1021/jz5001962.

[39]   M. F. Haase, N. Sharifi-Mood, D. Lee, and K. J. Stebe, "In Situ Mechanical Testing of Nanostructured Bijel Fibers," *ACS Nano*, 2016, doi: 10.1021/acsnano.6b02660.

[40]   S. Boakye-Ansah, M. S. Schwenger, and M. F. Haase, "Designing bijels formed by solvent transfer induced phase separation with functional nanoparticles," *Soft Matter*, 2019, doi: 10.1039/c9sm00289h.

[41]   S. Boakye-Ansah, M. A. Khan, and M. F. Haase, "Controlling Surfactant Adsorption on Highly Charged Nanoparticles to Stabilize Bijels," *J. Phys. Chem. C*, 2020, doi: 10.1021/acs.jpcc.0c01440.

[42]   M. A. Meyers, P. Y. Chen, A. Y. M. Lin, and Y. Seki, "Biological materials: Structure and mechanical properties," *Progress in Materials Science*. 2008, doi: 10.1016/j.pmatsci.2007.05.002.

[43]   E. Yashima, N. Ousaka, D. Taura, K. Shimomura, T. Ikai, and K. Maeda, "Supramolecular Helical Systems: Helical Assemblies of Small Molecules, Foldamers, and Polymers with Chiral Amplification and Their Functions," *Chemical Reviews*. 2016, doi: 10.1021/acs.chemrev.6b00354.

[44]   D. R. Smyth, "Helical growth in plant organs: Mechanisms and significance," *Development (Cambridge)*. 2016, doi: 10.1242/dev.134064.

[45]   J. G. Gibbs, A. G. Mark, T. C. Lee, S. Eslami, D. Schamel, and P. Fischer, "Nanohelices by shadow growth," *Nanoscale*, 2014, doi: 10.1039/c4nr00403e.

[46]   Y. Snir and R. D. Kamien, "Entropically driven helix formation," *Science (80-.).*, 2005, doi: 10.1126/science.1106243.

[47]   Y. Han, L. Zhao, and J. Y. Ying, "Entropy-driven helical mesostructure formation with achiral cationic surfactant templates," *Adv. Mater.*, 2007, doi: 10.1002/adma.200602703.

[48]   A. Kuzyk *et al.*, "DNA-based self-assembly of chiral plasmonic nanostructures with tailored optical response," *Nature*, 2012, doi: 10.1038/nature10889.

[49]   G. M. Grason and R. F. Bruinsma, "Chirality and equilibrium biopolymer bundles," *Phys. Rev. Lett.*, 2007, doi: 10.1103/PhysRevLett.99.098101.

[50]   M. S. Turner, R. W. Briehl, F. A. Ferrone, and R. Josephs, "Twisted Protein Aggregates and Disease: The Stability of Sickle Hemoglobin Fibers," *Phys. Rev. Lett.*, 2003, doi: 10.1103/PhysRevLett.90.128103.

[51]   J. W. Weisel, C. Nagaswami, and L. Makowski, "Twisting of fibrin fibers limits their radial growth.," *Proc. Natl. Acad. Sci. U. S. A.*, 1987, doi: 10.1073/pnas.84.24.8991.

[52]   J. Zheng *et al.*, "Electrospun Aligned Fibrous Arrays and Twisted Ropes: Fabrication, Mechanical and Electrical Properties, and Application in Strain Sensors," *Nanoscale Res. Lett.*, 2015, doi: 10.1186/s11671-015-1184-9.

[53]   L. Q. Liu, M. Eder, I. Burgert, D. Tasis, M. Prato, and H. D. Wagner, "One-step electrospun nanofiber-based composite ropes," *Appl. Phys. Lett.*, 2007, doi: 10.1063/1.2644379.

[54]   J. Forth *et al.*, "Reconfigurable Printed Liquids," *Adv. Mater.*, 2018, doi: 10.1002/adma.201707603.

[55]   M. A. Daniele *et al.*, "Rapid and continuous hydrodynamically controlled fabrication of biohybrid microfibers," *Adv. Funct. Mater.*, 2013, doi: 10.1002/adfm.201202258.

[56]   E. Koos, "Capillary suspensions: Particle networks formed through the capillary force," *Current Opinion in Colloid and Interface Science*. 2014, doi: 10.1016/j.cocis.2014.10.004.

[57]   R. V. Bell, C. C. Parkins, R. A. Young, C. M. Preuss, M. M. Stevens, and S. A. F. Bon, "Assembly of emulsion droplets into fibers by microfluidic wet spinning," *J. Mater. Chem. A*, 2016, doi: 10.1039/c5ta08917d.

[58]   P. Juelg *et al.*, "Automated serial dilutions for high-dynamic-range assays enabled by fill-level-coupled valving in centrifugal microfluidics," *Lab Chip*, 2019, doi: 10.1039/c9lc00092e.

[59]   M. Madou, J. Zoval, G. Jia, H. Kido, J. Kim, and N. Kim, "Lab on a CD," *Annual Review of Biomedical Engineering*. 2006, doi: 10.1146/annurev.bioeng.8.061505.095758.

[60]   W. Al-Faqheri *et al.*, "Development of a passive liquid valve (PLV) utilizing a pressure equilibrium phenomenon on the centrifugal microfluidic platform," *Sensors (Switzerland)*, 2015, doi: 10.3390/s150304658.

[61]   N. Honda, U. Lindberg, P. Andersson, S. Hoffmann, and H. Takei, "Simultaneous multiple immunoassays in a compact disc-shaped microfluidic device based on centrifugal force," 2005, doi: 10.1373/clinchem.2005.053348.

[62]   Y. Ouyang, S. Wang, J. Li, P. S. Riehl, M. Begley, and J. P. Landers, "Rapid patterning of 'tunable' hydrophobic valves on disposable microchips by laser printer lithography," *Lab Chip*, 2013, doi: 10.1039/c3lc41275j.

[63]   J. Ducrée, S. Haeberle, S. Lutz, S. Pausch, F. Von Stetten, and R. Zengerle, "The centrifugal microfluidic Bio-Disk platform," *J. Micromechanics Microengineering*, 2007, doi: 10.1088/0960-1317/17/7/S07.

[64]   M. C. R. Kong and E. D. Salin, "Micromixing by pneumatic agitation on continually rotating centrifugal microfluidic platforms," *Microfluid. Nanofluidics*, 2012, doi: 10.1007/s10404-012-0983-x.

[65]   J. N. Kuo and L. R. Jiang, "Design optimization of micromixer with square-wave microchannel on compact disk microfluidic platform," *Microsyst. Technol.*, 2014, doi: 10.1007/s00542-013-1769-0.

[66]   S. Yasuda, M. Hayakawa, H. Onoe, and M. Takinoue, "Twisting microfluidics in a planetary centrifuge," *Soft Matter*, 2017, doi: 10.1039/c6sm02695h.

[67]   S. P. Kharal, R. P. Hesketh, and M. F. Haase, "High-Tensile Strength, Composite Bijels through Microfluidic Twisting," *Adv. Funct. Mater.*, 2020, doi: 10.1002/adfm.202003555.

[68]   N. M. Ribe, M. Habibi, and D. Bonn, "Liquid Rope Coiling," *Annu. Rev. Fluid Mech.*, 2012, doi: 10.1146/annurev-fluid-120710-101244.

[69]   T. Luelf, C. Bremer, and M. Wessling, "Rope coiling spinning of curled and meandering hollow-fiber membranes," *J. Memb. Sci.*, 2016, doi: 10.1016/j.memsci.2016.01.037.

[70]   H. A. McKenna, J. W. S. Hearle, and N. O'Hear, *Handbook of fibre rope technology*. 2004.

[71]   C. Zhang, C. Gao, M. W. Chang, Z. Ahmad, and J. S. Li, "Continuous micron-scaled rope engineering using a rotating multi-nozzle electrospinning emitter," *Appl. Phys. Lett.*, 2016, doi: 10.1063/1.4964645.

[72]   E. Koos, "Current Opinion in Colloid & Interface Science Capillary suspensions : Particle networks formed through the capillary force," *Curr. Opin. Colloid Interface Sci.*, 2014, doi: 10.1016/j.cocis.2014.10.004.

[73]   R. V. Bell, C. C. Parkins, R. A. Young, C. M. Preuss, M. M. Stevens, and S. A. F. Bon, "Assembly of emulsion droplets into fibers by microfluidic wet spinning," *J. Mater. Chem. A*, 2016, doi: 10.1039/c5ta08917d.

[74]   G. Velve-Casquillas, M. Le Berre, M. Piel, and P. T. Tran, "Microfluidic tools for cell biological research," *Nano Today*. 2010, doi: 10.1016/j.nantod.2009.12.001.

[75]   H. Zhang *et al.*, "Photothermal-responsive nanosized hybrid polymersome as versatile therapeutics codelivery nanovehicle for effective tumor suppression," *Proc. Natl. Acad. Sci. U. S. A.*, 2019, doi: 10.1073/pnas.1817251116.

[76]   R. Gorkin *et al.*, "Centrifugal microfluidics for biomedical applications," *Lab on a Chip*. 2010, doi: 10.1039/b924109d.

[77]   D. Psaltis, S. R. Quake, and C. Yang, "Developing optofluidic technology through the fusion of microfluidics and optics," *Nature*. 2006, doi: 10.1038/nature05060.

[78]   J. G. Werner, B. T. Deveney, S. Nawar, and D. A. Weitz, "Dynamic Microcapsules with Rapid and Reversible Permeability Switching," *Adv. Funct. Mater.*, 2018, doi: 10.1002/adfm.201803385.

[79]   T. Salafi, K. K. Zeming, and Y. Zhang, "Advancements in microfluidics for nanoparticle separation," *Lab Chip*, 2017, doi: 10.1039/C6LC01045H.

[80]   T. J. Ober, D. Foresti, and J. A. Lewis, "Active mixing of complex fluids at the microscale," *Proc. Natl. Acad. Sci. U. S. A.*, 2015, doi: 10.1073/pnas.1509224112.

[81]   D. Di Carlo, D. Irimia, R. G. Tompkins, and M. Toner, "Continuous inertial focusing, ordering, and separation of particles in microchannels," *Proc. Natl. Acad. Sci. U. S. A.*, 2007, doi: 10.1073/pnas.0704958104.

[82]   W. Lee, H. Amini, H. A. Stone, and D. Di Carlo, "Dynamic self-assembly and control of microfluidic particle crystals," *Proc. Natl. Acad. Sci. U. S. A.*, 2010, doi: 10.1073/pnas.1010297107.

[83]   A. D. Stroock, S. K. W. Dertinger, A. Ajdari, I. Mezić, H. A. Stone, and G. M. Whitesides, "Chaotic mixer for microchannels," *Science (80-.).*, 2002, doi: 10.1126/science.1066238.

[84]   B. Grigoryan *et al.*, "Multivascular networks and functional intravascular topologies within biocompatible hydrogels," *Science (80-.).*, 2019, doi: 10.1126/science.aav9750.

[85]   F. Sharifi, Z. Bai, R. Montazami, and N. Hashemi, "Mechanical and physical properties of poly(vinyl alcohol) microfibers fabricated by a microfluidic approach," *RSC Adv.*, 2016, doi: 10.1039/c6ra09519d.

[86] Y. Yu, F. Fu, L. Shang, Y. Cheng, Z. Gu, and Y. Zhao, "Bioinspired Helical Microfibers from Microfluidics," *Adv. Mater.*, 2017, doi: 10.1002/adma.201605765.

[87] X. Y. Du, Q. Li, G. Wu, and S. Chen, "Multifunctional Micro/Nanoscale Fibers Based on Microfluidic Spinning Technology," *Advanced Materials*. 2019, doi: 10.1002/adma.201903733.

[88] S. Rammensee, U. Slotta, T. Scheibel, and A. R. Bausch, "Assembly mechanism of recombinant spider silk proteins," *Proc. Natl. Acad. Sci. U. S. A.*, 2008, doi: 10.1073/pnas.0709246105.

[89] G. Di Vitantonio, T. Wang, K. J. Stebe, and D. Lee, "Fabrication and application of bicontinuous interfacially jammed emulsions gels," *Applied Physics Reviews*. 2021, doi: 10.1063/5.0048797.

[90] Z. J. Derlacki, A. J. Easteal, A. V. J. Edge, L. A. Woolf, and Z. Roksandic, "Diffusion coefficients of methanol and water and the mutual diffusion coefficient in methanol-water solutions at 278 and 298 K," *J. Phys. Chem.*, 1985, doi: 10.1021/j100270a039.

[91] P. Wang *et al.*, "The Evolution of Flexible Electronics: From Nature, Beyond Nature, and To Nature," *Advanced Science*. 2020, doi: 10.1002/advs.202001116.

[92] J. Xiong, J. Chen, and P. S. Lee, "Functional Fibers and Fabrics for Soft Robotics, Wearables, and Human–Robot Interface," *Advanced Materials*. 2021, doi: 10.1002/adma.202002640.

[93] M. Kanik *et al.*, "Strain-programmable fiber-based artificial muscle," *Science (80-.).*, 2019, doi: 10.1126/science.aaw2502.

[94] B. B. Mandal, A. Grinberg, E. S. Gil, B. Panilaitis, and D. L. Kaplan, "High-strength silk protein scaffolds for bone repair," *Proc. Natl. Acad. Sci. U. S. A.*, 2012, doi: 10.1073/pnas.1119474109.

[95] Y. Cheng *et al.*, "Bioinspired multicompartmental microfibers from microfluidics," *Adv. Mater.*, 2014, doi: 10.1002/adma.201400798.

[96] P. Xu, R. Xie, Y. Liu, G. Luo, M. Ding, and Q. Liang, "Bioinspired Microfibers with Embedded Perfusable Helical Channels," *Adv. Mater.*, 2017, doi: 10.1002/adma.201701664.

[97] C. M. Leech, "The modelling and analysis of the mechanics of ropes," *Solid Mech. its Appl.*, 2014, doi: 10.1007/978-94-007-7841-2_1.

[98] O. Wichterle and D. Lím, "Hydrophilic Gels for Biological Use," *Nature*, 1960, doi: 10.1038/185117a0.

[99]   L. Klouda and A. G. Mikos, "Thermoresponsive hydrogels in biomedical applications - a review," *Eur J Pharm Biopharm*, 2011.

[100]   Y. Wang, A. Dong, Z. Yuan, and D. Chen, "Fabrication and characterization of temperature-, pH- and magnetic-field-sensitive organic/inorganic hybrid poly (ethylene glycol)-based hydrogels," *Colloids Surfaces A Physicochem. Eng. Asp.*, 2012, doi: 10.1016/j.colsurfa.2012.10.009.

[101]   H. P. Lee, G. Lokhande, K. A. Singh, M. K. Jaiswal, S. Rajput, and A. K. Gaharwar, "Light-Triggered In Situ Gelation of Hydrogels using 2D Molybdenum Disulfide (MoS2) Nanoassemblies as Crosslink Epicenter," *Adv. Mater.*, 2021, doi: 10.1002/adma.202101238.

[102]   J. E. Elliott, M. MacDonald, J. Nie, and C. N. Bowman, "Structure and swelling of poly(acrylic acid) hydrogels: Effect of pH, ionic strength, and dilution on the crosslinked polymer structure," *Polymer (Guildf).*, 2004, doi: 10.1016/j.polymer.2003.12.040.

[103]   F. Tu and D. Lee, "Shape-changing and amphiphilicity-reversing Janus particles with pH-responsive surfactant properties," *J. Am. Chem. Soc.*, 2014, doi: 10.1021/ja503189r.

Appendix A

Velocity and Shear Stress Profile along Rotation Direction

The equation of motion in cylindrical direction along rotation (θ) direction is

$$\frac{d}{dr}\left[\frac{1}{r}\left(\frac{d(rv_\theta r)}{dr}\right)\right].$$

Equation 10

Integrating twice the Equation 10 we get,

$$v_\theta(r) = C_1 r + \frac{C_2}{r}.$$

Equation 11

Boundary conditions:

$$(i) \; v_\theta(r) = \omega_1 R_1 \; at \; r = R_1$$

$$(ii) \; v_\theta(r) = \omega_2 R_2 \; at \; r = R_2$$

Using the boundary conditions in the Equation 11, we get

$$C_1 = \frac{\omega_1(R_2^2 - R_1^2) - (\omega_1 - \omega_2)R_2^2}{R_2^2 - R_1^2}.$$

Equation 12

And,

$$C_2 = \frac{R_2^2 R_1^2(\omega_1 - \omega_2)}{R_2^2 - R_1^2}.$$

Equation 13

Substituting the values of C_1 and C_2 in the Equation 11, we get

$$v_\theta(r) = \frac{\omega_1(R_2^2 - R_1^2) - (\omega_1 - \omega_2)R_2^2}{R_2^2 - R_1^2} \; r + \frac{R_2^2 R_1^2(\omega_1 - \omega_2)}{R_2^2 - R_1^2}\frac{1}{r}.$$

Equation 14

Finally, the Equation 14, after some algebraic simplification, takes the form

$$v_\theta(r) = \frac{R_2^2}{R_2^2 - R_1^2}\left[r\left(\omega_2 - \frac{\omega_1 R_1^2}{R_2^2}\right) - \frac{R_1^2(\omega_2 - \omega_1)}{r}\right].$$

Equation 15

The Equation 15 gives the velocity profile along the θ direction as a function of radius vector r.

Also,

$$\frac{d}{dr}\left(\frac{v_\theta(r)}{r}\right) = -\frac{2R_1^2 R_2^2 (\omega_2 - \omega_1)}{R_2^2 - R_1^2}\frac{1}{r^3}.$$

Equation 16

The shear stress along θ direction in a cylindrical coordinate system is

$$\tau_{r\theta} = \tau_{\theta r} = -\mu\left[r\left(\frac{\partial\left(\frac{v_\theta(r)}{r}\right)}{\partial r}\right) + \frac{1}{r}\frac{\partial v_\theta}{\partial \theta}(r)\right] = -\mu r\frac{\partial\left(\frac{v_\theta(r)}{r}\right)}{\partial r} = -\mu r\frac{d\left(\frac{v_\theta(r)}{r}\right)}{dr}.$$

Equation 17

Substituting the value of $\frac{d}{dr}\left(\frac{v_\theta(r)}{r}\right)$ from the Equation 16 to the Equation 17, we get

$$\tau_{r\theta}|_{R_1} = \tau_{\theta r}|_{R_1} = \left(\frac{2\mu R_1^2 R_2^2 (\omega_2 - \omega_1)}{R_2^2 - R_1^2}\right)\frac{1}{r^2}.$$

Equation 18

The Equation 9 gives the twisting shear stress profile along the rotation (θ) direction.

Appendix B

Velocity and Shear Stress Profile along Translation Direction

The equation of motion in cylindrical direction along translation (Z) direction is

$$\frac{1}{\mu}\frac{dp}{dz} = \frac{1}{r}\frac{d}{dr}\left(r\frac{d(v_z(r))}{dr}\right). \qquad\qquad Equation\ 19$$

Integrating twice the Equation 19 we get,

$$v_z(r) = \frac{r^2}{4\mu}\frac{dp}{dz} + C_3 lnr + C_4. \qquad\qquad Equation\ 20$$

Boundary conditions:

$$(i)\ v_Z(r) = U\ at\ r = R_1$$

$$(ii)\ v_Z(r) = 0\ at\ r = R_2$$

Using the boundary conditions in the Equation 20, we get

$$C_3 = \left[-U - \frac{dp}{dZ}\left(\frac{R_2^2 - R_1^2}{4\mu}\right)\right]\frac{1}{\ln\left(\frac{R_2}{R_1}\right)}. \qquad\qquad Equation\ 21$$

And,

$$C_4 = -\frac{dp}{dZ}\frac{R_2^2}{4\mu} - C_3 lnR_2. \qquad\qquad Equation\ 22$$

Now, substituting the values of C_3 and C_4 from the Equations 21 and 22 in the Equation 20, we get

$$V_Z(r) = -\frac{dp}{dZ}\frac{R_2^2 - R_1^2}{4\mu} + \left[U + \frac{dp}{dZ}\frac{(R_2^2 - R_1^2)}{4\mu}\right]\left(\frac{\ln\left(\frac{R_2}{r}\right)}{\ln\left(\frac{R_2}{R_1}\right)}\right). \qquad\qquad Equation\ 23$$

The Equation 23 gives the velocity profile along the translation (Z) direction.

134

Using the velocity profile, the flow rate can be expressed as (with θ the angular coordinate)

$$Q_W = \int_0^{2\pi} d\theta \int_{R_1}^{R_2} V_Z(r)\, r\, dr. \qquad\qquad \textit{Equation 24}$$

And, by direct integration, one can prove:

$$Q_W = \frac{\pi}{2\mu \ln\left(\frac{R_2}{R_1}\right)} \frac{dp}{dZ}\left[\left(\frac{R_1^4}{4} - \frac{R_2^4}{4}\right)\ln\left(\frac{R_2}{R_1}\right) + \left(\frac{R_2^2}{2} - \frac{R_1^2}{2}\right)\right]$$

$$-\frac{2\pi\mu}{\ln\left(\frac{R_2}{R_1}\right)}\left[\frac{R_1^2}{2}\ln\left(\frac{R_1}{R_2}\right) + \frac{R_2^2}{4} - \frac{R_1^2}{4}\right]. \qquad\qquad \textit{Equation 25}$$

So,

$$\frac{dp}{dZ} = \left(\frac{2\mu \ln\left(\frac{R_2}{R_1}\right)}{\pi J}\right)\left[Q_W + \frac{2\pi\mu}{\ln\left(\frac{R_2}{R_1}\right)}\left[\frac{R_1^2}{2}\ln\left(\frac{R_1}{R_2}\right) + \frac{R_2^2}{4} - \frac{R_1^2}{4}\right]\right], \qquad \textit{Equation 26}$$

where,

$$J = \left(\frac{R_1^2}{4} - \frac{R_2^2}{4}\right)\ln\left(\frac{R_2}{R_1}\right) + \left(\frac{R_2^2}{2} - \frac{R_1^2}{2}\right). \qquad\qquad \textit{Equation 27}$$

Again, differentiation the velocity profile in the Equation 23 with respect to r, we get

$$\left(\frac{dv_Z(r)}{dr}\right) = \frac{dp}{dZ}\left(\frac{2r}{4\mu}\right) - \left[U + \frac{dp}{dZ}\left(\frac{R_2^2 - R_1^2}{4\mu}\right)\right]\left(\frac{1}{R_1 \ln\left(\frac{R_2}{R_1}\right)}\right). \qquad \textit{Equation 28}$$

We focus our calculation on the shear stress on the surface of the bundle at $r = R_1$, so

$$\left(\frac{dv_z(R_1)}{dr}\right) = +\left[\frac{dp}{dZ}\frac{R_1^2}{2\mu}\ln\left(\frac{R_2}{R_1}\right) - \frac{dp}{dz}\left(\frac{R_2^2 - R_1^2}{4\mu}\right)\right]\left(\frac{1}{R_1 \ln\left(\frac{R_2}{R_1}\right)}\right). \qquad Equation\ 29$$

For $= U_o$, zero shear stress is exerted on the fiber surface, so

$$\left(\frac{dv_Z(R_1)}{dr}\right) = 0. \qquad Equation\ 30$$

Where,

$$U_o = \frac{dp}{dZ}\frac{R_1^2}{2\mu}\ln\left(\frac{R_2}{R_1}\right) - \frac{dp}{dZ}\left(\frac{R_2^2 - R_1^2}{4\mu}\right), \qquad Equation\ 31$$

and, with the zero-shear stress fiber velocity U_o, we obtain,

$$\left(\frac{dv_Z(R_1)}{dr}\right) = \left(\frac{U_o - U}{R_1}\right)\frac{1}{\ln\left(\frac{R_2}{R_1}\right)}. \qquad Equation\ 32$$

Combining this expression with Newton's law of viscosity, we calculate the shear stress on the surface of the fiber as

$$\tau_{rZ}|_{R_1} = \mu\left(\frac{dv_Z}{dr}\right)|_{R_1}, \qquad Equation\ 33$$

and,

$$\tau_{rZ}|_{R_1} = \mu\left(\frac{U_o - U}{R_1}\right)\left(\frac{1}{\ln\left(\frac{R_2}{R_1}\right)}\right). \qquad Equation\ 34$$

The Equation 34 gives the shear stress profile along the translation (Z) direction.

Mixing Table for Ternary Mixture Preparation with CTAB Concentration

Variation

Table C1

Mixing Table for Ternary Preparation with CTAB Variation

Batch name	Units	Formula	C40	C60	C80
Water fraction	mL/mL	ϕ_{water}	0.18	0.18	0.18
BA fraction	mL/mL	ϕ_{BA}	0.38	0.38	0.38
Methanol fract.	mL/mL	ϕ_{methOH}	0.44	0.44	0.44
Total volume	mL	V_{total}	1	1	1
Water fraction	**mL**	$\mathbf{V_{water}^{total}}$	**0.18**	**0.18**	**0.18**
Stock Ludox	g/g	w_{TMA}^0	0.420	0.420	0.420
Stock Ludox	g/mL	ρ_{TMA}^0	1.28	1.28	1.28
Sample Ludox	g/g	w_{TMA}^1	0.42	0.42	0.42
Sample Ludox	g/mL	$\rho_{TMA}^1 = \dfrac{\rho_{TMA}^0 - \rho_{water}}{w_{TMA}^0} * w_{TMA}^1 + \rho_{water}$	1.28	1.28	1.28
Volume of stock Ludox	mL	$V_{TMA} = V_{wa}^{total} * \dfrac{w_{TMA}^1 * \rho_{TMA}^1}{w_{TMA}^0 * \rho_{TMA}^0}$	**0.18**	**0.18**	**0.18**

Volume of water	mL	$V_{wa} = V_{wa}^{total} - V_{TMA}$	**0**	**0**	**0**
BA fraction	**mL**	$\mathbf{V_{BA}^{total} = V_{total} * \phi_{BA}}$	0.38	0.38	0.38
Volume BA	mL	$V_{BA} = V_{total} * \phi_{BA}$	**0.38**	**0.38**	**0.38**
MethOH fraction	**mL**	$\mathbf{V_{methOH}^{total} = V_{total} * \phi_{methOH}}$	**0.440**	**0.440**	**0.440**
Stock CTAB	mM	C_{CTAB}^0	200	200	200
Sample CTAB	mM	C_{CTAB}^1	**40**	**60**	**80**
Volume of CTAB stock	mL	$V_{CTAB} = V_{methOH}^{total} * \dfrac{C_{CTAB}^0}{C_{CTAB}^1}$	**0.088**	**0.132**	**0.176**
Stock Ludox	g/g	$w_{TMA_m}^0$	0.465	0.465	0.465
Stock Ludox	g/mL	$\rho_{TMA_m}^0$	1.21	1.21	1.21
Sample Ludox	g/g	$w_{TMA_m}^1$	0.067	0.067	0.067
Sample Ludox	g/mL	$\rho_{TMA_m}^1 = \dfrac{\rho_{TMA_m}^0 - \rho_{methOH}}{w_{TMA_m}^0} * w_{TMA_m}^1 + \rho_{methOH}$	0.853	0.853	0.853
Sample Ludox	mL	$V_{TMA_m} = V_{methOH}^{total} * \dfrac{w_{TMA_m}^1 * \rho_{TMA_m}^1}{w_{TMA_m}^0 * \rho_{TMA_m}^0}$	**0.066**	**0.066**	**0.066**
Vol. of methOH	mL	$V_{methOH} = V_{methOH}^{total} - V_{CTAB} - V_{TMA_m}$	**0.286**	**0.242**	**0.198**

Appendix D

Mixing Table for Ternary Mixture Preparation with Nanoparticle Concentration Variation

Table D1

Mixing Table for Ternary Preparation with Nanoparticle Concentration Variation

Batch name	Units	Formula	NP$_1$	NP$_2$	NP$_3$	NP$_4$	NP$_5$
Water fraction	mL/mL	ϕ_{water}	0.18	0.18	0.18	0.18	0.18
BA fraction	mL/mL	ϕ_{BA}	0.38	0.38	0.38	0.38	0.38
Methanol fract.	mL/mL	ϕ_{methOH}	0.44	0.44	0.44	0.44	0.44
Total volume	mL	V_{total}	1	1	1	1	1
Water fraction	**mL**	$\mathbf{V_{water}^{total}}$	**0.18**	**0.18**	**0.18**	**0.18**	**0.18**
Stock Ludox	g/g	w_{TMA}^0	0.420	0.420	0.420	0.420	0.420
Stock Ludox	g/mL	ρ_{TMA}^0	1.28	1.28	1.28	1.28	1.28
Sample Ludox	g/g	w_{TMA}^1	0.42	0.42	0.42	0.42	0.42
Sample Ludox	g/mL	$\rho_{TMA}^1 = \dfrac{\rho_{TMA}^0 - \rho_{water}}{w_{TMA}^0} * w_{TMA}^1 + \rho_{wa}$	1.28	1.28	1.28	1.28	1.28

Volume of stock Ludox	mL	$V_{TMA} = V_{wa}^{total} * \dfrac{w_{TMA}^1 * \rho_{TMA}^1}{w_{TMA}^0 * \rho_{TMA}^0}$	**0.18**	**0.18**	**0.18**	**0.18**	**0.18**
Volume of water	mL	$V_{wa} = V_{wa}^{total} - V_{TMA}$	**0**	**0**	**0**	**0**	**0**
BA fraction	**mL**	$V_{BA}^{total} = V_{total} * \phi_{BA}$	0.38	0.38	0.38	0.38	0.38
Volume BA	mL	$V_{BA} = V_{total} * \phi_{BA}$	**0.38**	**0.38**	**0.38**	**0.38**	**0.38**
MethOH fraction	**mL**	$V_{methOH}^{total} = V_{total} * \phi_{methOH}$	**0.440**	**0.440**	**0.440**	**0.440**	**0.440**
Stock CTAB	mM	C_{CTAB}^0	200	200	200	200	200
Sample CTAB	mM	C_{CTAB}^1	60	60	60	60	60
Volume of CTAB stock	mL	$V_{CTAB} = V_{methOH}^{total} * \dfrac{C_{CTAB}^0}{C_{CTAB}^1}$	**0.132**	**0.132**	**0.132**	**0.132**	**0.132**
Stock Ludox	g/g	$w_{TMA_m}^0$	0.465	0.465	0.465	0.465	0.465
Stock Ludox	g/mL	$\rho_{TMA_m}^0$	1.21	1.21	1.21	1.21	1.21
Sample Ludox	g/g	$w_{TMA_m}^1$	**0**	**0.034**	**0.067**	**0.102**	**0.136**

Sample Ludox	g/mL	$\rho^1_{TMA_m} = \dfrac{\rho^0_{TMA_m} - \rho_{meth.}}{w^0_{TMA_m}}$ $* w^1_{TMA_m} + \rho_{meth.}$	0.792	0.823	0.853	0.884	0.915
Sample Ludox	mL	$V_{TMA} = V^{total}_{methOH}$ $* \dfrac{w^1_{TMA_m} * \rho^1_{TMA_m}}{w^0_{TMA_m} * \rho^0_{TMA_m}}$	**0**	**0.032**	**0.066**	**0.104**	**0.143**
Vol. of methOH	mL	$V_{methOH} = V^{total}_{methOH} - V_{CTAB}$ $- V_{TMA_m}$	**0.308**	**0.276**	**0.242**	**0.204**	**0.165**

Appendix E

Ternary Mixtures with Various Initial Densities

Table E1

Final Composition Of Five Different Ternary Mixture (TM) Solution With Their Experimentally Measured Initial Densities And Silica Fractions (Calculated)

Composition	NP_1	NP_2	NP_3	NP_4	NP_5
(1) BA, mL	0.38	0.38	0.38	0.38	0.38
(2) Methanol, mL	0.308	0.276	0.242	0.204	0.165
(3) Ludox TMA in water, mL	0.18	0.18	0.18	0.18	0.18
(4) Ludox TMA in Methanol, mL	0	0.032	0.066	0.104	0.143
(5) C_{16}TAB, mL	0.132	0.132	0.132	0.132	0.132
Total volume (1)+(2)+(3)+(4)+(5), mL	1	1	1	1	1
Density of ternary mixture, g/cm^3 (meausred)	0.911	0.923	0.936	0.952	0.966
Silica particle wt. fraction (g/g) (calculated)	0.096	0.115	0.136	0.162	0.184
Silica particle volume fraction, (v/v) (calculated)	0.043	0.051	0.06	0.736	0.0854